Spin Chain Systems for Quantum Computing and Quantum Information Applications

MARTA P. ESTARELLAS

PHD

UNIVERSITY OF YORK

Physics

April, 2018

University of York

Abstract

York Center for Quantum Technologies
Department of Physics

Doctor of Philosophy

Spin Chain Systems for Quantum Computing and Quantum Information Applications

by Marta P. ESTARELLAS

One of the most essential processes in classical computation is that related to the information manipulation; each component or register of a computer needs to communicate to others by exchanging information encoded in bits and transforming it through logical operations. Hence the theoretical study of methods for information transfer and processing in classical information theory is of fundamental importance for telecommunications and computer science, along with study of errors and robustness of such proposals. When adding the quantum ingredient, there arises a whole new set of paradigms and devices, based on manipulations of *qubits*, the quantum analogues of conventional data bits. Such systems can show enormous advantage against their classical analogues, but at the same time present a whole new set of technical and conceptual challenges to overcome. The full and detailed understanding of quantum processes and studies of theoretical models and devices therefore provide the first logical steps to the future technological exploitation of these new machines. In this line, this thesis focuses on spin chains as such theoretical models, formed by series of coupled qubits that can be applied to a wide range of physical systems, and its several potential applications as quantum devices. In this work spin chains are presented as reliable devices for quantum communication with high transfer fidelities, entanglement generation and distribution over distant parties and protected storage of quantum information. Methods to design these tools to have some robustness against errors and noise are provided, giving optimism for future quantum technologies.

Contents

List of Figures

List of Tables

Acknowledgements

Let $|\Psi_M\rangle$ be my years as a PhD candidate. As $|\Psi_M(t)\rangle$ has evolved with time t, other wavefunctions have interfered with it, either constructively or destructively, shaping it to its new form. I would like to genuinely thank to all sorts of quantum interference that suitably arranged their phases to let $|\Psi_M\rangle$ arrive where it is today, but specially to the following constructive terms:

The main contribution on the wave amplitudes has undoubtedly been the constant support, patience, care and attention from my two PhD supervisors, Tim and Irene. I could not have been luckier to work with two better scientists. You not only introduced me to the wonderful world of Physics, but taught me something far more difficult: that I could be part of it. Thank you.

As with other quantum systems, $|\Psi_M\rangle$ is entangled to many other degrees of freedom, so many that there is no room enough to write the full mathematical form of such state in this page, but let me mention a few. Carlos, an excellent example of long-distance entanglement, thank you so much for existing in my life, helping me keep our coherence robust against any perturbation, your love and your mexican food. Andrés, another of the main components of this multipartite entangled system, thank you for always being there to cheer me up, providing me with endless pictures of pugs and cats and to be by my side over these years no matter what. I want to thank to all my university PhD battle comrades, Jan, Ryan, Iskandar, Jacob, Neville, Andrea, Luke, Manuel...and many more, for the beers, the laughs, the Japanese lessons, the quizz nights and your companionship in this journey (do not give up, quantum tunneling through the thesis and other academic barriers will eventually occur). And also thanks to Ibrahim, for being the best flatmate one could ask, a great friend and accompanying me in my relaxation times at home.

Last but not least, I want to thank the state $|\Psi_M\rangle$ always collapses to: my family. Entre tots m'ensenyàreu a caminar i, des de llavors, m'heu donat la força que m'impulsa a no haver d'aturar mai. Glòria, Pau i Marc, no calen paraules, vos estim.

Declaration of Authorship

I, Marta P. ESTARELLAS, declare that this thesis titled, "Spin Chain Systems for Quantum Computing and Quantum Information Applications" and the work presented in it are my own. I confirm that:

- This work was done wholly while in candidature for a research degree at this University.
- Where I have consulted the published work of others, this is always clearly attributed.
- Where I have quoted from the work of others, the source is always given. With the exception of such quotations, this thesis is entirely my own work.
- Part of the work from this thesis has been published. I was first author of [1, 2] and contributor author of [3, 4].

"Oh, benvinguts, passeu, passeu,
de les tristors en farem fum,
que casa meva és casa vostra,
si és que hi ha cases d'algú."

A tu, pradí

Chapter 1

Introduction

> "*It always bothers me that, according to the laws as we understand them today, it takes a computing machine an infinite number of logical operations to figure out what goes on in no matter how tiny a region of space, and no matter how tiny a region of time. How can all that be going on in that tiny space? Why should it take an infinite amount of logic to figure out what one tiny piece of space/time is going to do? So I have often made the hypotheses that ultimately physics will not require a mathematical statement, that in the end the machinery will be revealed, and the laws will turn out to be simple, like the chequer board with all its apparent complexities.*"
>
> Richard Feynman

Quantum mechanics has had a huge impact into many areas of science by providing a whole new mathematical framework that helped – and keeps helping – us to enhance our knowledge of Nature in a very accurate way. This theory is so powerful that its applications reached the information science arena, giving rise to what could be – if not yet – a new technological revolution.

The idea of a mathematical computational model based on quantum mechanics came first from the need of finding a more general representation than the one offered by the classical Turing machine [5]. The Church-Turing thesis asserted that any algorithmic process could be efficiently simulated using a Turing machine which, in turn, could be simulated by a universal Turing machine. However, the original universal Turing machine was soon insufficient to simulate *any* algorithmic process. Some problems cannot be efficiently solved by classical computers, even after randomised algorithms were introduced [6] and the Church-Turing thesis was strengthened with the *ad hoc* hypothesis of a probabilistic Turing machine.

At the same time, the simulation of Nature's processes has been one of the main applications in the history of computation. Yet, the fact that Nature is also quantum sets a practical limitation on its complete simulation. The number of variables needed to tackle problems related to quantum phenomena grows exponentially with the size of the system in a classical computer. There are ways to partially overcome this limitation, both from the software perspective such as excellent approximation

models (e.g. perturbation or density functional theories) or the hardware architecture with the use of distributed computing approaches. However, no classical computational paradigm has yet been postulated for an efficient and accurate complete description of such problems.

Another important aspect is that there is a limitation in the evolution flow on the manufacturing of electronic devices. In 1965, Moore predicted that the number of transistors per integrated circuit was doubling and would double once every year [7]. Ten years later he adjusted such prediction to allow the number of transistors to double once every two years only [8] for the following decade. The direct consequence of this is that computers – and other electronic devices – would double in power by allocating more transistors that are smaller in size. We all have been able to observe the validity of such prediction, embedded in the information revolution we have witnessed these last two decades. However, this exponential trend based on the capabilities of the current technological approach to semiconductors is about to bow as quantum effects start interfering and become more prominent in such small scales.

It was soon demonstrated that a quantum computer could efficiently solve some of these aforementioned limitations. Deutsch [9] proposed that a new version of the universal Turing machine could be quantum. Problems that have no classical efficient solution such as finding the prime factors of an integer [10] or searching in an unstructured space [11] could potentially be solved in a quantum computer, as shown by Shor and Grover. Also, in the same way classical computers efficiently simulate many classical problems, quantum computers would also be expected to excel in the simulation of quantum phenomena. The variables needed for such simulations grow linearly with the size of the problem, in contrast with the exponential growth of the classical counterpart. The recognition of quantum effects as a tool for computation would also help to keep up with Moore's law as we can envisage transistors as small as one single atom [12].

Quantum computing is not the only application promised from the exploitation of quantum phenomena. Under the same framework, new technologies and devices are already being realised, e.g. to allow for secure communication (quantum cryptography [13] and quantum communication [14]) or to enhance the precision of physical measurements (quantum metrology [15]). Even though the present work will focus on computing, it is important to remark that the quantum and mathematical formalism behind it provides a total new way of dealing with information. The extension of this theory is so vast that it may well end up contributing to science and technology with forms that we have yet not been able to even imagine.

All of the previous are just a few examples of the potential advances this technology can offer. It may happen that difficult constraints are encountered in its development process -some of which, have in fact already been found- but there is a strong argument for researchers to pursue this field as far as we can. This thesis aims to contribute a humble tiny piece of this huge quantum puzzle and to illustrate in

detail the applications of spin-chains for quantum computing.

1.1 Quantum Information and Quantum Computation

In this section the fundamentals of the theory behind Quantum Information and Computation (QIC) technologies are provided as a set of general definitions [16]. A broad picture of the state of the field from the experimental point of view is reviewed and a list of desirable qualities, when it comes to the physical implementation of a quantum computer device, is examined.

1.1.1 General definitions

Qubit

In classical computing, bits are the basic units of information. A bit can be represented by any two states device as a 0/1, +/- sign, true/false, the presence or absence of a hole in a punched card, etc. Yet it will always be in one of these two values. On the contrary, one of the remarkable features of quantum mechanics is that it allows a two level quantum system to be in a linear combination of its two possible states or *superposition*. This gives rise to the analogous concept of the bit in quantum computing: the qubit.

By convention, we take 0 and 1 as the two possible states of a bit and, similarly, $|0\rangle$ and $|1\rangle$ as the states of a qubit. These two states are referred to as the computational basis, orthonormal vectors by which any arbitrary qubit can be represented such as,

$$|\Psi\rangle = \alpha|0\rangle + \beta|1\rangle, \tag{1.1}$$

where α and β are complex numbers. $|\alpha|^2$ and $|\beta|^2$ are the probabilities of measuring the qubit to be in the state $|0\rangle$ and $|1\rangle$, respectively. Given that such probabilities must sum to one, a qubit state will always fulfill the normalisation relation $|\alpha|^2 + |\beta|^2 = 1$.

State space

Any quantum physical system has an associated Hilbert space $\mathscr{H}$, which in the context of quantum information is a finite vector space with inner product also called *state space*. The system, in turn, can be described by one state vector, which will be a unit vector $|\Psi\rangle$ of its Hilbert space. Such unit vector can be represented as a linear combination of the vectors that form a *complete set* on that space.

We have seen that one possible set of two vectors spanning the Hilbert space of a single qubit is $|0\rangle$ and $|1\rangle$, which by convention correspond to the vectors $\binom{1}{0}$ and $\binom{0}{1}$, respectively. This implies that the Hilbert space for one qubit has dimension two, $\mathbb{C}^2$. Such vectors are linearly independent and orthonormal, so any state of the qubit can be described as a linear combination (or superposition) of these two (Eq. 1.1). When encountering a system with more than one qubit, the dimension of the Hilbert space

is not 2 anymore and 2^N vectors are required to fully describe the system, N being the number of qubits, $\mathscr{H} = \bigotimes_N \mathbb{C}^2$.

Basis

The same Hilbert space $\mathscr{H}$ can have more than one complete set of vectors. If the vectors of a set are linearly independent, such set will form a basis for $\mathscr{H}$. For instance, a single qubit can have $|0\rangle$ and $|1\rangle$ as a basis but also $|\varphi_\alpha\rangle \equiv \frac{1}{\sqrt{2}}\binom{1}{1}$ and $|\varphi_\beta\rangle \equiv \frac{1}{\sqrt{2}}\binom{1}{-1}$. The vectors of both sets are orthogonal to each other, linearly independent and can be transformed to another by a unitary transformation, so any state of the qubit can be represented with any of both basis.

Having said that, in quantum information, and due to their resemblance with strings of bits, it is common to take as a complete basis the 2^N possibilities of distributing the "zeros" and "ones" in a system of N qubits. This way, the v basis vectors of a system can be written as $|\Phi_v\rangle = |\phi_1\rangle \otimes |\phi_i\rangle \otimes ...|\phi_N\rangle$ with i being the qubit index and $|\phi_i\rangle \in (0, 1)$. This notation is often simplified, as shown below, with all the values being written in order inside a single ket. As an example, for a three qubits system, the $2^3 = 8$ vectors describing the basis will be the following:

$$
\begin{aligned}
|\Phi_1\rangle &= |000\rangle \\
|\Phi_2\rangle &= |100\rangle \\
|\Phi_3\rangle &= |010\rangle \\
|\Phi_4\rangle &= |001\rangle \\
|\Phi_5\rangle &= |110\rangle \\
|\Phi_6\rangle &= |101\rangle \\
|\Phi_7\rangle &= |011\rangle \\
|\Phi_8\rangle &= |111\rangle.
\end{aligned}
$$

We will refer to this basis as the *site basis* and it will be the one used in this work. The vectors will be labeled in the same consistent way, in increasing order of "ones" and by moving one "one" forward at a time.

Quantum states

We have seen that any state vector $|\Psi\rangle$ of the Hilbert space can be represented as a linear combination of the vectors that form a complete basis set. Therefore any arbitrary quantum state of a system can be described as a superposition of the basis vectors, $|\Phi_v\rangle$,

$$
|\Psi\rangle = \sum_v c_v |\Phi_v\rangle, \tag{1.2}
$$

with the normalisation condition $\sum_v |c_v|^2 = 1$. Again, the superposed nature of quantum states is in sharp contrast to what the states in classical computation look like. Yet, as it will follow, there is much more behind these superpositions and some states, such as entangled states, point to a rich variety of potential advantages for quantum information applications.

In order to understand the particularities and differences of quantum states, the state vector $|\Psi\rangle$ representation, even though very intuitive, is not always the most convenient. We here introduce a mathematical tool named the density operator or matrix, ρ, under which any quantum state can be represented in an equivalent manner to the state vector representation. Under this general description, any quantum system can be described by,

$$\rho = \sum_i p_i |\psi_i\rangle\langle\psi_i|, \tag{1.3}$$

being p_i the probability of finding the system in the pure state $|\psi_i\rangle$ and with the fulfillment of the normalisation condition $\sum_i p_i = 1$. The density operator is always positive and has trace equal one. It evolves by a unitary transformation such that $\rho(t_2) = U\rho(t_1)U^\dagger$, being U the unitary operator that relates the state of the system at time t_2 with the system at time t_1 [16].

- **Pure state**

If the state of the quantum system is fully known the system is in a pure state. A superposition of pure states is also a pure state. In terms of the density matrix we have a pure state if and only if $tr(\rho^2) = 1$ (or $\rho \equiv \rho^2$). This implies the existence of just one state with probability $p = 1$ and therefore the density matrix can be reduced to $\rho = |\psi\rangle\langle\psi|$. It can be then easily shown that $tr(\rho) = tr(\rho^2) = 1$ as $\rho^2 = |\psi\rangle\langle\psi|\psi\rangle\langle\psi| = |\psi\rangle\langle\psi|$ because $\langle\psi|\psi\rangle = 1$.

We therefore know that pure states can still be easily represented as a state vector $|\Psi\rangle$, and given that over this work we will be mostly dealing with pure states, we will stick to this representation.

- **Mixed state**

In some circumstances, the state of a quantum system is found to be as an ensemble or mixture of pure states. This is that the system is formed by a set of pure states $|\psi_i\rangle$ with probability p_i. In such cases it is then useful to use the representation from Eq. 1.3. Again, the trace of the squared density matrix, ρ, offers a criterion to determine whether the state is in a mixture: $tr(\rho^2) < 1$.

Quantum measurement

The measurement of the state of a qubit is one of the most fundamental challenges in QIC technologies and a direct consequence of quantum mechanics. When performing a computation, one will surely need to know the outcome state sooner or later

in order to make a use of it. However, the complete knowledge of a quantum state is, unfortunately, something not easily attainable. Any superposition representing the state of a single- or a multiple-qubit state will project upon measurement into a different state, called the *post-measurement state*.

The nature of such post-measurement state, $|\Psi'\rangle$, depends on the measurement operator, M_w, acting on the state space of the system being measured, where w is the index of the possible outcomes of the measurement, what forms a complete set of measurement operators. If we measure a state $|\Psi\rangle$, the probability of measuring w is $\mathcal{P}(w) = \langle\Psi|M_w^\dagger M_w|\Psi\rangle$, and the sum of all the outcome probabilities is normalised to unity as the measurement operators satisfy the completeness equation $\sum_w M_w^\dagger M_w = I$. This measurement leaves the system in the state:

$$|\Psi'\rangle = \frac{M_w|\Psi\rangle}{\sqrt{\langle\Psi|M_w^\dagger M_w|\Psi\rangle}} \tag{1.4}$$

This means that even though we can operate and perform computation on the different amplitudes in quantum superposition and therefore take advantage of them, we will need to use clever methods to gain as much information as possible from the final state. This becomes more problematic when dealing with mixed states, as uncertainty upon measurement does not only come from the collapse of the quantum superposition into the post-measurement state but also from the classical uncertainty due to the state being a probabilistic ensemble of pure states. The probability of measuring the state ρ is $\mathcal{P}(w) = tr(M_w^\dagger M_w \rho)$ leaving the post-measurement state $\rho' = \frac{M_w \rho M_w^\dagger}{tr(M_w^\dagger M_w \rho)}$.

Entanglement

Entanglement is one of the most characteristic features of quantum mechanics and implies a strong correlation between qubits or subsections of a quantum system. This correlation can be mathematically recognised in the way the quantum state looks like: an entangled state can not be described as a product state of each of the N sections forming the system, this is $|\Psi\rangle \neq |\psi_1\rangle \otimes |\psi_i\rangle ... |\psi_N\rangle$. A state describing two qubits A and B, $|\Psi_{AB}\rangle = \frac{1}{\sqrt{2}}(|10\rangle + |11\rangle)$ can be factorised as a product state between the subspaces $\mathscr{H}_A$ and $\mathscr{H}_B$, such that $|\Psi_{AB}\rangle = |1_A\rangle \otimes \frac{1}{\sqrt{2}}(|0_B\rangle + |1_B\rangle)$. If the state is instead entangled, such as the Bell state $|\Psi_{AB}\rangle = \frac{1}{\sqrt{2}}(|10\rangle + |01\rangle)$, there is no way to separate the subspace components from A and B.

Entanglement has profound implications when it comes to fitting quantum mechanics into our intuitive description of the world. Let us suppose we have two entangled qubits. When either of the two qubits are measured, the state of the other qubit is influenced by the measurement outcome, no matter how far apart they are. This contradicts the *locality* hypothesis, which states that any physical process of a system occurring at one location should not have any effect on the properties of another system in a different location if information cannot travel faster than the speed

of light. On the other hand, entanglement also disagrees with the *realism* hypothesis, which affirms that physical properties have well-defined values independently of whether they have or have not been measured. This lack of local realism led Einstein, Rosen and Podolsky (EPR) to question the completeness of Quantum Mechanics [17]. However, the EPR classical interpretation was soon called into question in 1963 when John S. Bell showed through his 'no-go theorem' that systems strictly subject to local realism cannot reproduce all the predictions of quantum mechanics. This was theoretically proved through the violation of Bell's inequality [16], results that were confirmed experimentally by John F Clauser and Stuart J Freedman in 1972 [18], and have more recently been backed with demonstrations [19] that are loophole-free [20]. Certainly, we must abandon the idea of local realism when navigating the seas of quantum mechanics.

There are mathematical quantities that allow us to prove whether a state is entangled and in what extent: Von Neumann entropy and Entanglement of Formation. The Von Neumann entropy, $S(\rho)$, determines whether a state ρ is pure or mixed and it is defined by:

$$S(\rho) \equiv -tr(\rho \log \rho). \tag{1.5}$$

If $S(\rho) = 0$, the state is pure, otherwise it is in a mixture. This mixed state happens to be completely mixed if the entropy is equal to $\log d$ with d being the dimension of the Hilbert space [16]. The presence of bipartite entanglement between subsystems A and B using this measure can be identified by tracing out B from the density matrix, ρ, such that $\rho_A = tr_B \rho$. If $S(\rho_A) = 0$ there is no entanglement between A and B [21], while if nonzero, the presence of entanglement is guaranteed provided that the overall state of A and B is pure.

Even though the entropy is a good measure of the level of mixture in the system and allows to identify the presence of entanglement, when dealing with mixed states it does not provide a good indication on how much entangled the state is. In order to quantify this, we need a monotonic measure called Entanglement of Formation (EOF) [22]. This is a bipartite measure of entanglement for mixed states and it is going to be formally defined in Chapter 2. However let us now mention that, when dealing with pure states, the amount of entanglement can also be expressed by the simple formula of the pure concurrence [22], $\mathcal{C}$, of an arbitrary two qubits state $|\Psi\rangle = c_{00}|00\rangle + c_{01}|01\rangle + c_{10}|10\rangle + c_{11}|11\rangle$:

$$\mathcal{C} = 2|c_{00}c_{11} - c_{01}c_{10}|. \tag{1.6}$$

EOF and $\mathcal{C} \in \{0, 1\}$, and the state is said to be maximally entangled when $EOF = 1$ (or $\mathcal{C} = 1$). Bell states (also refered as EPR pairs) are a set of four maximally bipartite entangled states widely used in QIC. There are also states that exhibit multipartite entanglement, some examples include GHZ, W or Cluster states and different ways of calculating their concurrence exist [23, 24].

Entanglement represents an essential resource for quantum computation and it is used in many quantum information protocols [25]. Teleportation of one qubit is a process in which the state of a quantum bit can be transmitted with the use of one classical communication channel and a pre-shared maximally entangled Bell state [26]. Similarly, a pre-shared pair of entangled qubits is needed for superdense coding [27], protocol which allows to transmit two bits of information per qubit, or for some quantum key distribution (QKD) protocols [28], enabling two parties to share a cryptographic key securely.

Decoherence

Quantum noise or decoherence is a fundamental obstacle in the processing of quantum information placing one of the biggest challenges for the practical realisation of a quantum computer [16]. Because all quantum systems will ultimately be open (this is, coupled to external degrees of freedom, usually called 'environment'), the system will eventually get entangled with external degrees of freedom and the coherence of any quantum superposition will be lost. Amplitude or phase evolution will be affected by decoherence, hampering the conservation of the quantum state.

The coherence times are the average times for which the superposition of a quantum state is conserved and they are strongly dependent on the qubit implementation. T_1 is the timescale for the amplitude damping, process in which there is an energy loss for the system until the thermal equilibrium is reached due to its coupling with the environment. For example, this is the time taken at low temperatures for an "excited" state $|1\rangle$ to decay into its "ground" state $|0\rangle$. T_2 is the timescale of the phase damping, i.e. time needed for a state $\frac{|0\rangle+|1\rangle}{\sqrt{2}}$ to acquire a random relative phase. In general, T_2 is much smaller than T_1, meaning that T_2 is more important for quantum computation. In addition, even though decoherence is generally referred to time-dependent quantum noise, static disorder due to slowly varying energy fluctuations or fabrication defects are another types of error that will probably be present in realistic systems.

Even though implementations (see later in this introduction) allowing a high degree of isolation of the qubit such as ion traps or NV-centres [29] are being realised along with developing fault-tolerant quantum computation proposals based on topological phenomena [30], the complete suppression of decoherence is unlikely. Nonetheless, instead of trying to avoid errors, one could think of correcting them. Error correcting codes can make the number of errors due to quantum noise almost negligible, providing that the system has been optimised up to a certain threshold of allowed disorder [31], but at the expense of an important experimental overhead as more qubits are required.

Quantum gates

In order to perform a quantum computation, as in classical computing, we need a quantum circuit formed by gates. Such gates are used to manipulate and change the information. In classical computers, gates are physical electronic devices able to perform a logical (Boolean) operation to one single string of bits (NOT) or between two different strings (AND, OR, NAND, XOR, NOR, XNOR). Quantum computers need analogous components able to perform different unitary operations to single qubits (i.e. state rotations or Hadamard gates) and multiple qubits (i.e. controlled gates such as CNOT).

Single qubit gates can be described as unitary matrices, $U^\dagger U = I$, of size two. To illustrate some of the most common examples, the X (or NOT), Z and Hadamard gates act on an arbitrary qubit $\alpha|0\rangle + \beta|1\rangle$ of a circuit as,

$$\begin{aligned}
\alpha|0\rangle + \beta|1\rangle \;—\boxed{X}— \;& \alpha|1\rangle + \beta|0\rangle \\
\alpha|0\rangle + \beta|1\rangle \;—\boxed{Z}— \;& \alpha|0\rangle - \beta|1\rangle \\
\alpha|0\rangle + \beta|1\rangle \;—\boxed{H}— \;& \alpha\tfrac{|0\rangle+|1\rangle}{\sqrt{2}} + \beta\tfrac{|0\rangle-|1\rangle}{\sqrt{2}}
\end{aligned}$$

These can be represented in the computational basis with the following matrices,

$$X = \begin{pmatrix} 0 & 1 \\ 1 & 0 \end{pmatrix} \quad Z = \begin{pmatrix} 1 & 0 \\ 0 & -1 \end{pmatrix} \quad H = \frac{1}{\sqrt{2}} \begin{pmatrix} 1 & 1 \\ 1 & -1 \end{pmatrix} \tag{1.7}$$

On the other side, multiple qubit gates have multiple qubits as input/output and the output of the operation depends on the relation between their states. One of the most used ones is the CNOT gate, which uses a control, $|C\rangle$, and a target, $|T\rangle$, qubit. This gate will perform an X operation to the target qubit ($X|T\rangle$) as long as the control qubit is in a state $|1\rangle$. In circuit language, this gate is described as follows,

$$\begin{aligned}
|C\rangle \;—\bullet— \;& |C\rangle \\
|T\rangle \;—\oplus— \;& |C \oplus T\rangle
\end{aligned}$$

being the operation $|C \oplus T\rangle$ the addition modulo two (also simulated by a XOR gate) and represented by the following 4x4 matrix,

$$CNOT = \begin{pmatrix} 1 & 0 & 0 & 0 \\ 0 & 1 & 0 & 0 \\ 0 & 0 & 0 & 1 \\ 0 & 0 & 1 & 0 \end{pmatrix} \tag{1.8}$$

A set of gates is said to be universal if any computation can be described using a sequence of gates from that set. For example, a set of AND, OR, NOT gates is enough to grant universality in classical computing. In the early 90's universality was shown to be attained even from only NAND (or NOR) gates [32]. In the quantum counterpart, any arbitrary operation can be described in a circuit built with a toolkit formed by single qubit gates, to perform any arbitrary single qubit rotation, and any two qubit gate capable of producing entanglement, such as a CNOT gate, to allow for arbitrary operations on multiple qubits [16, 33].

1.1.2 State of the art

The number of scientific and technological achievements with applicability to QIC technologies has been growing exponentially every year since the first ideas on the potential applications of quantum computers were born [9, 34, 35].

Hardware implementations for the realisation of qubits have been proposed, using systems as diverse as photons, semiconductors, superconductors or molecules, some of which will be explored in Section 1.2.3. Each of these presents strengths and weaknesses as many factors come into play: coherence times, scalability, initialisation, read-out, gate operations, etc. For example, NV-centers and ion traps present excellent long coherence times (T_2 of the order of seconds) but show control issues when scaling to larger systems. If one could extract and combine the benefits of each implementation we would be closer to the building of a large-scale quantum computer. This is the idea behind the pursue of hybrid quantum computer architectures [36], schemes that would make the most of each implementation's potential. It is, in fact, from such perspective that we think the class of devices proposed in this thesis could be included in the prospective design of a scalable quantum computer.

Even though new cryogenic methods and refinement on the materials engineering enhance coherence times and increase quantum computing speed, e.g. for superconducting qubits the coherence times increased from $\sim 1\,\mathrm{ns}$ to $\sim 100\,\mu\mathrm{s}$ [37], decoherence is still a problem. For now, error correcting codes are one of the best solutions to this issue and these techniques are already being applied with practical error rates [38]. Another way to potentially avoid decoherence is to use topological quantum computer architectures which perform computation through the braiding of quasiparticles called non-abelian anyons [30, 39, 40], but this is still a theoretical model as, even though predicted, non-abelian anyons have not yet been definitively detected.

With respect to quantum communication, photon-based qubits are the preferred platform due to their relative resistance against decoherence (as they interact very little with the environment) and abilities to be guided through long distances in optical fibers [41]. Quantum communication protocols realising quantum key distribution (QKD), superdense coding and teleportation have been implemented [42–44] and some QKD devices are already being commercialised [45]. Quantum communication is quickly developing up to a level where ambitious applications are envisaged

such as the design and implementation of a quantum internet [46] or the realisation of satellite-based communication. The latter is already a reality and the distribution of an entangled pair of photons has been attained over distances as large as $1200\,\mathrm{km}$, something crucial for many applications [47].

From the simulation point of view, since the very first quantum algorithms by Grover, Deutsch and Shor were formulated, hundreds of new algorithms have been proposed [48]. Experimental demonstrations of algorithms running in different quantum computer platforms of modest size have been realised [49, 50]. Large computer companies such as IBM, Google, Microsoft or Intel are stepping forward in the race for the commercialisation of the first quantum computer, making the scalability of their computer prototypes and the design of quantum software and algorithms their main priority. In 2016, Google and Martinis' group presented a quantum computer build out of an array of 9 superconducting qubits which were able to detect and correct bit-flip errors among themselves [38]. A year after, this computer was able to calculate the potential energy surface of the hydrogen molecule [51], reporting for the first time the use of a quantum computer to solve a real quantum chemistry problem. At the same time, IBM released their 5-qubits quantum computer (which they would soon upgrade to 17-qubits), also using superconducting qubits, and made it available to public through their cloud system called 'Quantum Experience' (QX). Both Google and IBM released their own quantum software, OpenFermion [52] and QISkit [53], respectively, providing the user with an accessible interface to program and run their own quantum algorithms. New ambitious goals have been already set for 2019, with IBM announcing the release of a 50-qubits computer and Google promising a 72-qubits quantum chip, systems that are believed that would outperform the computer capabilities of their classical counterparts.

1.1.3 Device design and DiVincenzo criteria

Even though still in its infancy, this field is growing fast. A ceaseless search for efficient quantum software (logic, algorithms, cryptography, etc) and reliable hardware (buses, memories, gates, routers, etc) contributes to a better understanding of what this technology will look like in a not too far future. However, the nature of the implementations that will be needed in a quantum computer is still not known, as no definite architectural proposal has really outperformed the others yet. In the meantime, devices and protocols based on different implementations able to manipulate and operate with quantum information are being designed and even fabricated. Back in 2000, DiVincenzo published his popular criteria for the physical implementation of quantum computation and communication [54] where he established a set of conditions any quantum device would be required to satisfy. This thesis presents a model along with its design capable to implement different quantum operations that we believe can be of technological interest. Because of this, let us first briefly go through DiVincenzo criteria, which will later help us to evaluate the performance and suitability of our proposal as a quantum device.

1. The system needs to be scalable and its qubits have to be well characterised.

The qubit is the building block of QIC and therefore it is essential to have it very well defined. This entails that the physical realisation of the qubit has to be a two levels system with a complete knowledge of the parameters that differentiate each of the levels (e.g. their energies). However, one isolated qubit has not much use other than its sole study and parametrisation. At the moment, and still under debate [55], the estimated number of qubits needed to outperform a classical computer is about 50 [56]. Therefore there is an obvious need for any proposed system to be able to handle several qubits. This will add more parameters that need to be taken into account, such as physical interactions between qubits, state correlations and external field fluctuations. There are several proposals for the realisation of a qubit and we will briefly see some of them in the following section.

2. There must be a way to initialise the system to a specified state.

In computing any variable needs to have an initial value assigned. It does not matter if it is defined in the context of a high level language program or as a register of the processor. In example, the arithmetic logic unit (ALU) of a computer processor performs basic operations (add, subtract, multiply and divide) between a small set of registers that temporarily allocate the data needed for a specific operation. If the computation needs to calculate the sum (add) of two variables, the control unit (CU) needs to first allocate the value of those variables into the registers rA and rB. If this initialisation is not done, the sum operation will not be correct.

Even though this requirement may sound a bit too obvious, when applying this to QIC, initialisation becomes a real technical issue. One possible method for doing this would be to cool down the system to its ground state, as long as such state is well specified (i.e. through natural thermalisation at very low temperature so the state is approximately pure). Alternatively, one could perform a set of projective measurements to prepare the system to a useful known state. It is however important to pay special attention to the time needed for this, which even though is strongly related to the physical implementation, will always need to be shorter than the operation times.

3. The relevant decoherence time needs to be much longer than the operation time.

As already introduced, decoherence can be problematic for the processing of quantum information. Such disturbance affects the state of the system converting it to a mixed state or by altering the state amplitudes. The integrity of the computation is consequently compromised. It is therefore required that the computation runs in a much smaller time scale than decoherence does.

A possible way around relies on error correcting codes, which make use of ancillary qubits to identify and correct the errors caused by decoherence. However such methods are not exempt of limitations, as they require many additional ancillary qubits and the level of decoherence still needs to be below a threshold to guarantee fault-tolerance [16].

> **4.** There must exist a universal set of quantum gates.

We have seen that one-qubit gates along with a single two qubit gate capable of generatin entanglement form a universal set [16], which allows any computation to be represented under those gates. However, alternatives to these gates performing a specific operation are also available. We will here explore one such alternative when presenting our proposed entangling gate in Chapter 5.

The unitary operations performed by a quantum gate are generated by the specific Hamiltonian of the device. This means that the dynamics of the device needs to have some level of controllability, this is to turn on/off the evolution at the required time (i.e. switch-off qubit-qubit interactions). In addition, such switch needs to be quick enough to optimize the operation time of the gate. Quantum gates will also suffer from fabrication random errors and therefore the maximum tolerable decoherence time should always be smaller than the operation time.

> **5.** A specific qubit has to be accessible for measurement.

In the same way it is basic for the computation to require input of an initial state, it is also essential to be able to retrieve the output. This is done by reading out the state of certain specified qubits without changing the state of the rest of qubits. Once again, in order to be efficient, the measurement has to be done on a short time scale in order to avoid decoherence errors. However even when the efficiency of the measurement is low, one can improve it by running the same computation several times and take the averaged value of the sample.

> **6.** There must be a way to encode the state of a stationary qubit into a flying qubit.

The hardware of a quantum computer will be mainly built out of static qubits, as well as short-ranged quantum communication devices, an example of which will be explored in Chapter 3. However, the quantum communication needed to cover longer distances will require the use of flying qubits, which will generally be photons. This makes it necessary to find a way to encode the state of the static qubit into a photon state. This is a hard requirement to fulfill and up to date only few modest size implementations have achieved it [57–59].

7. There must be a way to transmit flying qubits between two points.

In all quantum communications, the coherence of the photonic qubit needs to be preserved until the full state has been transmitted. There are many cryptographic techniques and protocols that are focused on allowing the communication to fulfill this requirement [14, 41].

1.2 Spin Chains

In the early 1920s, the Stern-Gerlach experiment [60] demonstrated the existence of a quantized property of the electron: the *spin*. This was later regarded as an intrinsic angular momentum of elementary particles that can take discrete non-negative values depending on the nature of the particle (fermions or bosons). Because it is a natural two level quantum system, the spin-$\frac{1}{2}$ can be described under the qubit model of Eq. 1.1. It is in this context that spin chains are approached in QIC, as any qubit can be mathematically regarded as a spin. Hence, in the quantum information language, spin chains are a theoretical model composed of an ensemble of two-level quantum systems coupled to each other [61]. The spin chain formalism can be applicable to a range of physical systems representing a chain of permanently coupled qubits. Thus, our focus will be on the mathematical aspect of this device putting special attention to the structure and natural dynamics of these chains.

The angular momentum associated to the spin-$\frac{1}{2}$ is an observable that can be described with the Pauli operators. These are defined by the following 2x2 Hermitian matrices σ_x, σ_y and σ_z:

$$\sigma_x = \begin{pmatrix} 0 & 1 \\ 1 & 0 \end{pmatrix} \quad \sigma_y = \begin{pmatrix} 0 & -i \\ i & 0 \end{pmatrix} \quad \sigma_z = \begin{pmatrix} 1 & 0 \\ 0 & -1 \end{pmatrix} \tag{1.9}$$

The two states of the spin-$\frac{1}{2}$ are thus the eigenstates of the Pauli operator σ_z acting at site i of an N-site chain, with eigenvalues +1 and -1 respectively and represent the spin up $|\uparrow\rangle$ and spin down $|\downarrow\rangle$ states. Such states are mapped into the computational basis or the qubit $|1\rangle$ and $|0\rangle$ states, respectively. Because the components of the spin are well-defined using the Pauli matrices, such operators are very useful for the general treatment of two level systems. Importantly, the Pauli matrices and the Identity matrix (see below) form a complete set of 2x2 Hermitian matrices by which any single qubit gate (see Section 1.1.1) can be described.

$$\mathbb{I} = \begin{pmatrix} 1 & 0 \\ 0 & 1 \end{pmatrix} \tag{1.10}$$

1.2.1 Models

An N-sites spin-$\frac{1}{2}$ chain with nearest-neighbour interactions and open boundary conditions can be described by the following general Heisenberg Hamiltonian [62]:

$$\mathcal{H} = \frac{1}{2}\sum_{i=1}^{N-1} J_{i,i+1}[(1+\lambda)\sigma_x^i\sigma_x^{i+1} + (1-\lambda)\sigma_y^i\sigma_y^{i+1} + \Gamma\sigma_z^i\sigma_z^{i+1}] + \sum_{i=1}^{N}\epsilon_i\sigma_z^i \tag{1.11}$$

The on-site energies, ϵ_i, are called homogeneous if they are not site dependent. The strength of the interaction between sites is defined by the coupling energies, $J_{i,i+1}$. Several spin models arise depending on the symmetry of the interaction between spins, also named anisotropy. The Heisenberg model or XXX model is obtained when $\lambda = 0$ and $\Gamma = 1$. If $\lambda = 0$ and $\Gamma \neq 1$, the spin chain is described by a XXZ model with the special case of $\Gamma = 0$ regarded as the XX (also called XY) model. This is the one considered in this thesis and will be described in detail in Section 2.1.1. For completeness, if $\lambda \neq 0$ and $\Gamma \neq \{0, 1\}$ the model is called XYZ, and when $\lambda = \pm 1$ and $\Gamma = 0$, it is called the Ising model.

1.2.2 Applications

In recent years spin chains have acquired growing importance within the field of quantum information processing, mainly as means of efficiently transferring information [61–64]. Such chains can represent the "perfect wire" for quantum data transmission through microscopic distances. Therefore, a spin chain able to ensure faithful and efficient state transfer between two sites can be applied to the building of quantum buses interconnecting various computer components, such as registers within quantum processors or memories. This would allow the communication and scalability of the components of a quantum computer without the need of converting the quantum state into different types of information in all-solid state quantum computer implementations. Schemes allowing quantum state transfer in spin chains include the engineering of interactions [65–68], and alternative encoding schemes such as wavepacket [65, 69] or dual rail encoding [70].

Spin chain systems are also used for the creation and distribution of entangled qubits within a solid state-based quantum processor or computer [2, 62, 71–76]. Both entanglement creation and distribution can be seen as an alternative for quantum communication between two registers which can be attained through teleportation protocols [26, 77], which rely on pre-shared pairs of maximally entangled qubits. Examples include proposals on the generation of entanglement through the natural dynamics of the system [2, 4, 71, 73, 78], statically by initialising an antiferromagnetic chain to an appropriate eigenstate [79–82] or by performing a sudden change of the Hamiltonian or "quench" of Kondo spin chains [62, 83, 84].

In addition, complex structures of spin networks with different geometries can be defined under the same formalism of a spin chain [62]. Such devices can allow for the

transfer [66, 85], routing [86], switching [87] or splitting of the quantum information through active or passive operations that are being applied to parts of the network.

1.2.3 Physical implementations

We now review a few examples of solid-state experimental platforms that could realise a spin chain. This is by no means an exhaustive exploration of all the possible physical implementations given that, as already mentioned, any proposal of a qubit that can in turn be effectively coupled to more of them can be mapped onto a spin chain or network. We thus have focused on some of the most pursued implementations which satisfy, to a greater or lesser extent, the DiVincenzo criteria.

Quantum dots

Quantum dots (QD) are small structures that have electrons or excitons confined by a localised potential with discrete electronic states. Because of that, they are also called "artificial atoms" and can be realised in different ways, i.e. as electrostatically defined quantum dots or as self-assembled quantum dots. The use of this type of semiconductor nanostructures was proposed as a platform for quantum computation [88, 89]. There are different types of quantum dots depending on how the information is encoded: electron quantum dots [65, 89] or exciton quantum dots [90–92].

Quantum dot excitons encode the qubit state with existence or nonexistence of a ground state exciton in the QD as the logical one or zero, respectively [93, 94]. When no external fields are applied, the system is in its ground state and when electromagnetic radiation is applied, the system can be initialised to the desired state. On the other hand, the use of single spins in electron quantum dots can also encode a qubit given that, as already shown, spin-$\frac{1}{2}$ is a perfect example of a two level system. Magnetic and electric fields allow the control of individual spins while for the read-out there must be a spin-to-charge conversion before a charge measurement is applied [95]. Nonetheless, alternative methods for initialisation, control and measurement of single spin quantum dots have been proposed using ultrafast optical pulses [96].

Superconducting qubits

Superconducting quantum circuits are currently one of the preferred platforms to build a quantum computer. These are based on the electrical (LC or resonant circuit) circuit forming a loop which can be described as an harmonic oscillator. Such circuit is generally build with Aluminum which at low temperatures allows the frictionless flow of electricity [97]. A Josephson Junction imposes a non-linear inductance and anharmonicity to the superconducting circuit and simulates a two level artificial atom [98]. This system allows the design and measure of macroscopic quantum effects by tuning the classical electrical elements of the circuit.

Depending on the degree of freedom being used for the encoding, we can distinguish three types of superconducting qubits: charge, flux and phase qubits [99]. In flux qubits, the two quantum states of the qubit are a magnetic flux pointing up and down and are represented by a double-well potential. A charge qubit encodes the qubit as an integer number of Cooper pairs in a superconducting island. Phase qubits use the change on the oscillation amplitudes of phase of the conductance wavefunction (which is a superconducting order parameter) across a Josephson Junction. The Transmon qubit (or Xmon) forms part of this last group and is currently the dominant qubit implementation of this type [99].

Regulated microwave pulses allow to perform single qubit rotations as well as state initialisation. Two qubit gates are implemented by coupling different qubits either by using a quantum bus or by joining neareast-neihgbour qubits to an electrical circuit. The read-out process depends on the type of qubit, e.g. for flux qubits the state is measured using a magnetometer.

Two of the main drawbacks of superconducting qubits [100] are related to the errors in the manufacturing process of the device, and the low temperatures required (around $50\,\mathrm{mK}$) to operate, which hampers the scaling of this architecture.

Trapped ions

An alternative solid-state hardware approach uses ion traps, where a small number of atoms or ions are confined in an isolated space using electromagnetic fields [101]. Each ion encodes the qubit state in the two internal levels defined within an hyperfine manifold or a forbidden optical transition, states which can be efficiently controlled attaining long coherence times [102]. Initialisation is done by cooling down the system to its ground state using optical pumping and the state is measured using state-dependent fluorescence techniques with very high fidelities [101, 103, 104]. Single qubit gates are realised by the application of appropriate pulses of electromagnetic radiation, providing a quantum logic of excellent fidelity [103]. Interactions between neighbouring ions are due to Coulomb interactions mediated with laser pulses, which allow for multiple qubit quantum gates [41]. In fact, the first ever logical CNOT gate was realised with trapped ions according to Cirac and Zoller's proposal [105, 106].

While ion traps provide excellent coherence times of the order of minutes for hyperfine qubits and seconds for optical traps [103], the scaling of these systems to a large number of qubits, even though progress in micro-fabrication techniques is being made, is still not possible, making the scalability issue the main disadvantage of this platform [100, 104].

NMR-based processors

Another proposed platform takes advantage of Nuclear Magnetic Resonance (NMR) techniques and store the quantum information in the nuclear spins of the atoms of an

ensemble of molecules [62, 102]. One qubit gates are realised using radio-frequency pulses that allow to manipulate the nuclei. The spin magnetization defining the state of the qubit is measured as an induced current of a coil surrounding the sample.

Such experiments can use liquid or solid samples. In liquid NMR (LNMR), the sample is dissolved in a solvent and can be seen as an ensamble of independent quantum computers (one molecule as one computer) running in parallel. The couplings between spins depend on the type of molecules but are generally weak due to the molecular motion [62]. Solid-state NMR (SNMR) allow for faster gates due to stronger dipolar interactions as the molecules are now fixed. They present relaxation times T_1 of the order of seconds, and even minutes for solid-state samples along with a phase damping time scale T_2 of the order of hundreds of milliseconds.

One disadvantage is initialisation as it is difficult to prepare the system in an initial pure state even though techniques such as pseudo-pure state initialisation or algorithmic cooling have been proposed [107]. Nevertheless, in 1999 Samuel L. Braunstein showed that no entanglement is found in NMR experiments [108], so the practicality of such devices for quantum computation is limited [25]. The type of measurements allowed is quite restricted as it is not possible to address individually a single nucleus, and the measurement output is an average over all the molecule's signals [16].

The main advantages of this type of physical realisations rely on the advanced and mature state of the NMR techniques, something that has allowed to demonstrate many QIC experiments and has helped in the development of other quantum computer technologies. Up to date, functional NMR quantum computers able to run algorithms and quantum error correction protocols have been implemented up to a size of 12 qubits [109].

Others

Many other technologies with QIC capabilities have been proposed. Coupled waveguides and photonic lattices present a particularly useful tool as they allow for the systematic engineering of networks of different geometries and coupling configurations [62, 110, 111]. In such structures, the qubit is represented by a distinct lattice site, or the individual waveguide, and the encoding is realised by the presence or absence of a photon at a given site, corresponding to the $|1\rangle$ and $|0\rangle$ states, respectively [112]. Molecular and atomic spins in solids are also good qubit candidates due to their long coherence times, examples include fullerenes [113], ^{31}P donors in silicon [114] or diamond NV-centres [115]. The latter has emerged as one of the preferred candidates for room temperature QIC due to its robust spin quantum states [116]. Among its advantages, it is possible to prepare the electronic and nuclear spins of a NV-centre with high fidelity and detect their quantum states in a single measurement [116].

1.3 Thesis outline

In addition to this Introduction, this thesis is divided in five more chapters. Chapter 2 describes the mathematical methods used to obtain the results that will be presented. Three chapters will be the main core of the thesis and will focus on the detailed investigation of the three different spin chain applications we here foresee: quantum data buses, quantum state memories and quantum entangling gates. Chapter 3, part of which is based on [3], discusses the use of spin chains for quantum state transfer with a focus on the presence of Anderson localisation when randomised on-site energies are present. The next application of spin chains is described in Chapter 4 where the quantum state localisation and protection due to the presence of topologically protected eigenstates is considered. Some of the results are based on the work published in [1]. The last application we contemplate is the use of spin chain systems as quantum entangling gates and we present detailed analysis of this in Chapter 5, study that is also published in [2, 4]. Finally, Chapter 6 covers a general discussion on the feasibility for our proposed models and protocols to be used as a reliable quantum device: we revisit the set of requirements stated by DiVincenzo criteria and assess the performance of the suggested applications in physical systems. In addition, an outlook on the future of this research topic is also given as a part of the concluding remarks.

Chapter 2

Methods

In this chapter we describe in detail the procedures followed to perform the numerical calculations used to generate the results of this thesis. We have made use of our own numerical methods (mainly coded in Fortran90 and Python) to perform the computations needed. When required, the numerical results have been compared with the analytical counterparts to ensure the correctness of our approach.

The theoretical nature of this work makes the computer our laboratory and the numerical simulations of the quantum systems here explored, our methods. The first thing our computations need is input of the initial conditions of the system which the Hamiltonian represents. The diagonalisation of the Hamiltonian matrix allows us to obtain the eigenstates and eigenvalues of the system, providing the necessary ingredients to solve the Schrödinger equation. In order to assess the quality of the different proposed devices we calculate various quantities that measure the performance of a given operation, i.e. fidelity, entanglement or occupation probability. Such performance is tested against the presence of different types of fabrication errors or operation time delays in order to evaluate the robustness of the various protocols and devices proposed in this thesis. The mathematical theory behind the methods used and described here is accompanied with an outline of a simplified version of the algorithm used to compute them written in pseudocode.

2.1 Building the spin chain

2.1.1 Hamiltonian and Schrödinger equation

One of the postulates of quantum mechanics states that the time evolution of any system is governed by the Schrödinger equation [117, 118],

$$i\hbar\frac{\partial}{\partial t}|\Psi(t)\rangle = \mathcal{H}(t)|\Psi(t)\rangle. \tag{2.1}$$

By solving it for a given initial state $|\Psi(0)\rangle$, the state of the system at any time t, $|\Psi(t)\rangle$, can be determined. In conservative systems the total energy of the system is conserved as its Hamiltonian does not depend on time. We here consider our system

to be well isolated and therefore uncoupled to an external environment, hence its total energy will be constant. In such cases, given the eigenvalues and eigenstates of the Hamiltonian, the time-dependent Schrödinger equation can be solved.

In order to obtain those we need to solve the eigenvalue equation of $\mathcal{H}$:

$$\mathcal{H}|\varphi_k\rangle = E_k|\varphi_k\rangle, \tag{2.2}$$

being $\{|\varphi_k\rangle\}$ the set of eigenstates with their corresponding eigenenergies, $\{E_k\}$. Once these quantities are obtained, we can write our state at any time in terms of the eigenstates of $\mathcal{H}$, as they form a complete basis set:

$$|\Psi(t)\rangle = \sum_k a_k(t)|\varphi_k\rangle, \tag{2.3}$$

with,

$$a_k(t) = \langle\varphi_k|\Psi(t)\rangle. \tag{2.4}$$

Given that the eigenstates of the system do not depend on t, the time dependence of $|\Psi(t)\rangle$ is contained in the coefficients $a(t)_k$. If we now project Eq. 2.1 onto the eigenstates of $\mathcal{H}$,

$$i\hbar\frac{\partial}{\partial t}\langle\varphi_k|\Psi(t)\rangle = \langle\varphi_k|\mathcal{H}|\Psi(t)\rangle, \tag{2.5}$$

and knowing from Eq. 2.2 that $\langle\varphi_k|\mathcal{H} = E_k\langle\varphi_k|$, we can write Eq. 2.5 as,

$$i\hbar\frac{\partial}{\partial t}a_k(t) = E_k a_k(t). \tag{2.6}$$

By direct integration the time dependence of the coefficients is $a_k(t) = a_k(0)e^{-iE_k t/\hbar}$ and therefore the state of the system evolves as,

$$|\Psi(t)\rangle = \sum_k a_k(0)e^{-iE_k t/\hbar}|\varphi_k\rangle, \tag{2.7}$$

with $a_k(0) = \langle\varphi_k|\Psi(0)\rangle$. In our calculations, we have set $\hbar = 1$.

It is then clear that our top priority will be to obtain the eigenvectors and eigenvalues from the diagonalisation of our Hamiltonian in Eq. 2.2, from which we can find an exact solution of Eq. 2.1 when the Hamiltonian does not depend on time. In order to do so we first need to build the Hamiltonian matrix, which will require a set of basis states. The site basis is usually taken for convenience, however we could have chosen any different complete basis set. The form of the Hamiltonian matrix will differ depending on the basis vectors of choice but its evolution will be the same. The algorithm followed to build and diagonalise the Hamiltonian is outlined in Alg. 1.

As already introduced, there are several Hamiltonian models to represent spin chains. In this thesis we wish to account for one-dimensional spin chain systems

with nearest-neighbour interactions. We will consider the XY Hamiltonian (also referred to as XX Hamiltonian):

$$\mathcal{H}_{XY} = \frac{1}{2}\sum_{i=1}^{N-1} J_{i,i+1}\left(\sigma_x^i\sigma_x^{i+1} + \sigma_y^i\sigma_y^{i+1}\right) + \sum_{i=1}^{N}\frac{\epsilon_i}{2}(\sigma_z^i + \mathbb{I}), \tag{2.8}$$

where $J_{i,i+1}$ are the positive couplings between nearest-neighbour sites i and $i+1$, which will acquire different values depending on the type of chain under study, and N is the total number of sites in the chain. The X, Y and Z components of the spin are represented by the Pauli matrices already introduced in Section 1.2.

The first term of Eq. 2.8 imposes an isotropic coupling between the X and Y components of the spin-spin interactions between sites i and $i+1$. By doing this we ensure that the total Z component of the system commutes with the Hamiltonian. As will be discussed in Section 2.1.2, the immediate consequence of this is that the system conserves the total number of excitations (in our notation this is the number of 'ones' in the total qubit state), something desirable for quantum information applications.

The second term represents the on-site energies of the chain corresponding to the energy cost of exciting one site $|0\rangle \rightarrow |1\rangle$ (see Fig. 2.1). When no perturbations are considered, this term will be omitted as we choose all the on-site energies, ϵ_i, to be equal and, for convenience, rescaled to zero.

Even though it is quite common to see spin Hamiltonians represented by Pauli matrices as in Eq. 2.8, sometimes it can be clearer to write them in qubit notation. This is attained by using the following notation

$$\sigma_x = |1\rangle\langle 0| + |0\rangle\langle 1| \tag{2.9}$$

$$\sigma_y = i\left(|1\rangle\langle 0| - |0\rangle\langle 1|\right) \tag{2.10}$$

$$\sigma_z = |1\rangle\langle 1| - |0\rangle\langle 0|, \tag{2.11}$$

and rewriting the Hamiltonian in terms of raising and lowering operators. In this thesis we use this notation and convert the Hamiltonian from Eq. 2.8 to the following form:

$$\mathcal{H}_{XY} = \sum_{i=1}^{N-1} J_{i,i+1}[|1\rangle\langle 0|_i \otimes |0\rangle\langle 1|_{i+1} + |0\rangle\langle 1|_i \otimes |1\rangle\langle 0|_{i+1}] + \sum_{i=1}^{N}\epsilon_i|1\rangle\langle 1|_i. \tag{2.12}$$

Under this notation it is then easy to understand the first term as the hopping of an excitation, $|1\rangle$, over the chain sites as shown in Fig. 2.1. In addition, the above Hamiltonian can be mapped to a model of noninteracting spinless fermions with nearest-neighbour interaction through the Jordan-Wigner transformation [119], making this Hamiltonian a general representation for many real fermionic systems:

$$\mathcal{H}_{XY} = \sum_{i=1}^{N-1} J_{i,i+1}(a_i^\dagger a_{i+1} + a_{i+1}^\dagger a_i) + \sum_{i=1}^{N} \epsilon_i (a_i^\dagger a_i). \tag{2.13}$$

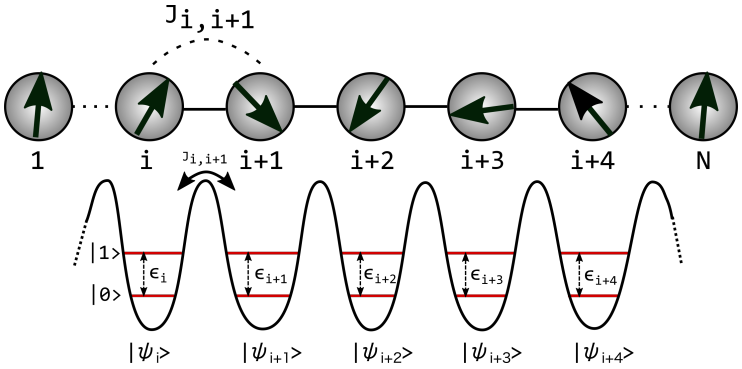

FIGURE 2.1: Schematic labeled representation of a one-dimensional linear spin chain with the particle hopping term $J_{i,i+1}$ and the on-site energies ϵ_i.

Data:
k: number of basis vectors
N: number of sites
$J[N-1]$: array with pre-defined couplings
Result: k eigenstate vectors $\varphi_k[k]$ and k eigenvalues E_k
$H = 0$ (initialise Hamiltonian matrix);
$Basis_k[N] = 0$ (initialise k basis vectors to have all 0's);
for *all the excitation subsectors* $\mathcal{E}$ **do**
  $Basis_k[N]$=all k permutations of $\mathcal{E}$ 1's in vectors of size N;
end
for *every pair of basis vectors* $\{basis_i, basis_j\}$ **do**
  if *same number of 1's* **then**
    sum the two vectors $w[N] = basis_i[N] + basis_j[N]$;
    for *every term* n *in* $w[N]$ **do**
      if *two consecutive 1's* **then**
        fill Hamiltonian term $H[i,j]$ with $J[n-1]$;
      end
    end
  end
end
Diagonalise H with LAPACK subroutine $\Rightarrow \{\varphi_k[k]\}$ and $\{E_k\}$;

Algorithm 1: Building and diagonalising the XY Hamiltonian of a linear chain.

2.1.2 Encoding and initial injection

As already discussed in Section 1.2, the sites (or spins) of a spin chain are qubits, as any two level quantum system can be mapped into a spin-$\frac{1}{2}$. The encoding of quantum information over a spin chain is done (unless otherwise stated) by direct correspondence between a single site and a single qubit ($site \mapsto qubit$). Each qubit can either contain a spin down state ($|\downarrow\rangle$), a spin up state, ($|\uparrow\rangle$), or a superposition of both ($\alpha|\downarrow\rangle + \beta|\uparrow\rangle$). Given the spin/qubit correspondence we can translate such states into a more common qubit notation such that,

$$|\downarrow\rangle \mapsto |0\rangle \tag{2.14}$$

$$|\uparrow\rangle \mapsto |1\rangle \tag{2.15}$$

$$\alpha|\downarrow\rangle + \beta|\uparrow\rangle \mapsto \alpha|0\rangle + \beta|1\rangle \tag{2.16}$$

Any pure non-entangled state of the full N-sites chain can be formally written as a tensor product state of the individual qubits such that $|\Psi\rangle = |\psi_1\rangle \otimes ...|\psi_i\rangle \otimes |\psi_{i+1}\rangle...|\psi_N\rangle$, being $1, ..., i, i+1, ...N$ the labels of each qubit or site (as shown in Fig. 2.1) and $|\psi_i\rangle$ any arbitrary state ($\alpha|0\rangle + \beta|1\rangle$). It is although common to simplify such expression notation and omit the tensor products, e.g. a state with a spin up at site $i = 1$ and the rest down would read $|\Psi\rangle = |100..0\rangle$. From now on, we will use the term *excitation* to refer to a spin up or a qubit in the $|1\rangle$ state.

The total number of excitations in the chain is given by the operator $\mathcal{E} = \sum_i^N |1\rangle\langle 1|_i$. This number is conserved given that its operator commutates with the Hamiltonian, $[\mathcal{H}, \mathcal{E}] = 0$. This implies that our Hilbert space $\mathscr{H}$ can be decomposed into excitation subspaces $\mathscr{H}_\mathcal{E}$ each containing $\mathcal{V}_\mathcal{E} = \begin{pmatrix} N \\ \mathcal{E} \end{pmatrix} = N!/\big(\mathcal{E}!(N-\mathcal{E})!\big)$ basis vectors, corresponding to all the possibilities of distributing the number of indistinguishable excitations $\mathcal{E}$ in a chain of N sites. Each basis vector is therefore defined by $|\Phi_v\rangle = |\phi_1...\phi_i...\phi_N\rangle$ with $\phi_i \in 0, 1$ and $\sum_i^N \phi_i = \mathcal{E}$. The possibility of partitioning $\mathscr{H}$ allows us to treat each $\mathscr{H}_\mathcal{E}$ eigenspace independently.

As stated by DiVincenzo [54] (and already addressed in Section 1.1.3), one of the fundamental requirements for a device to realise quantum computation relies on its initialisation. One must be able to initialise the qubits comprising a quantum computing device to a known state, e.g. $|00...0\rangle$. We are interested in having our spin chain initially with all the spins down, $|\downarrow\downarrow ... \downarrow\rangle$, which happens to be the ground state. This state will not evolve until we *inject* an excitation by flipping one of the spins to a spin up $|\uparrow\rangle$ or to a superposition $\alpha|0\rangle + \beta|1\rangle$. We will use the term *initial injection* to refer to this process.

In our numerics, we prepare the system for such initial injection by mapping our initial state into the Hamiltonian eigenstates, given that they also form a complete basis themselves. Suppose that we inject into a system that has all spins down,

$|vac\rangle = |00..0\rangle$, an arbitrary qubit state of $\alpha|0\rangle + \beta|1\rangle$ into the site s. This initial state can be mapped to the N one-excitation sector eigenstates such that,

$$|\Psi(0)\rangle = (\alpha|vac\rangle + \beta \sum_{k=1}^{N} \langle\varphi_k|00..1_s..00\rangle|\varphi_k\rangle). \tag{2.17}$$

As in Eq. 2.7, the subsequent time dependence of such a state is,

$$|\Psi(t)\rangle = \alpha|vac\rangle + \beta \sum_{k=1}^{N} \langle\varphi_k|00..1_s..00\rangle e^{-iE_k t/\hbar}|\varphi_k\rangle, \tag{2.18}$$

and the algorithm used to compute it is presented in Alg. 2.

Injecting and retrieving information will depend on the specific hardware used for embedding the mathematical concept of spin chain and some specific methods will be discussed in Section 6.1.

Data:
T: total time
V: injected vector index
Result: evolved state $\Psi(t)$
for *all eigenstates k* **do**
  $a_k(0)$ = CONJG$[\varphi_k[V]]$;
end
$t = 0$;
for $t < T$ **do**
  for *all eigenstates* k **do**
    $a_k(t)$ = $a_k(0)$EXP$[-itE_k]$;
  end
end
$\Psi(t)$ =SUM$[a_k(t)\varphi_k]$

Algorithm 2: Encoding of the initial state and time evolution.

2.2 Measures of device performance

2.2.1 Fidelity

The fidelity is one of the most common measures to test the performance of a chain as a quantum device. This is a time-dependent quantity that indicates how close the evolving state ($e^{-i\mathcal{H}t/\hbar}|\Psi(0)\rangle$) of a system is to any arbitrary desired state ($|\Psi_{des}\rangle$). In order to obtain this we calculate the modulus square of the overlap between these two states as,

$$\mathcal{F}(t) = |\langle\Psi_{des}|e^{-i\mathcal{H}t/\hbar}|\Psi(0)\rangle|^2, \tag{2.19}$$

with $0 \leq \mathcal{F}(t) \leq 1$ (see Alg. 3). This allows us to study the quality of state transfer for a spin chain acting as quantum wire (as will be seen in Chapter 3). For instance, we can check when and how well a spin up state $|1\rangle$ injected at site $i = 1$ arrives to the other end of the chain (site $i = N$) by calculating the overlap between the evolution of the initial state, $|1_1 0...0\rangle$, and the desired state, $|00...1_N\rangle$. A fidelity close to 1 indicates a good quality of the quantum state transfer, in this specific case, between sites $i = 1$ and $i = N$. It is also important to note that the transfer of the quantum state is considered to be useful as long as its transfer fidelity is above a threshold of $\frac{2}{3}$ [62, 120]. This measure does not only allow us to asses transport features but also to identify formation of new states, e.g. as a result of a quantum operation "hidden" in the natural dynamics of the chain (as will be seen in Chapter 3).

Data:
$\Psi(t) = SUM[a_k(t)\varphi_k]$: evolved state
V: desired vector state index
T: total time
Result: fidelity F(t)
$t = 0$;
for $t < T$ **do**
  for *all eigenstates* k **do**
    $F(t) = F(t) + CONJG[a_k(t)\varphi_k[V]] * [a_k(t)\varphi_k[V]]$
  end
end

Algorithm 3: Calculation of fidelity

2.2.2 Site occupation probability

The study of the structure of the full state, $|\Psi(t)\rangle$, allows us to obtain the probability, $\mathcal{P}_i$, of every site, i, to be occupied by an excitation ($|1\rangle_i$). When studying localisation and transfer suppression phenomena (as in Chapter 3) it is useful to look at these probabilities. If we map our k eigenstates into our $\mathcal{V}$ site basis vectors, $|\Phi_v\rangle$, such that,

$$|\varphi_k\rangle = \sum_{v}^{\mathcal{V}} c_{k,v}|\Phi_v\rangle, \tag{2.20}$$

we know that we can describe our state as,

$$|\Psi(t)\rangle = \sum_{k} a_k(t) \sum_{v} c_{k,v}|\Phi_v\rangle. \tag{2.21}$$

We can then combine the coefficients into a single expression such that $d_{k,v}(t) = a_k(t)c_{k,v}$. From here, the site occupation probabilities are easy to extract for the one-excitation subsector as there is a direct mapping between the vectors, $|\Phi_v\rangle$, and the

sites, i, as $\mathcal{V} = N$, and we can show that $\mathcal{P}_i = \sum_k^N |d_{k,i}(t)|^2$. This however gets more complicated when increasing the number of excitations ($\mathcal{V} \neq N$), where we need to find the occupation probability of a site i by summing all the coefficients of the vectors with nonzero probabilities at that site, $\mathcal{P}_i = \sum_k |d_{k,v}(t)|^2$ with $|\Phi_v\rangle = |00..1_i..0\rangle$.

In this thesis we will also look at the site occupation probability of the eigenstates in order to analyse localisation signatures (explored in Chapter 3 and 4). In such cases, we will only consider the first excitation subsector so the probabilities can be obtained from projecting the eigenstates into the site basis vectors, $\mathcal{P}_i = \sum_k^N |\langle\varphi_k|\Phi_i\rangle|^2$

2.2.3 Entanglement of formation

In order to quantify entanglement we use the entanglement of formation, EOF, a bipartite measure of entanglement for mixed states [121]. We will apply this measure to find the degree of entanglement between an arbitrary pair of qubits $\mathcal{A}$ and $\mathcal{B}$ when considering the general case of mixed states. We choose this quantity and not the pure concurrence (see Section 1.1.1) because although our initial states will be pure, due to entanglement with the rest of the chain at later times, the state of just sites $\mathcal{A}$ and $\mathcal{B}$ could be mixed. This entanglement measure is defined by,

$$EOF_{AB} = \xi(C_{AB}), \tag{2.22}$$

being $\xi(C_{AB}) = h(\frac{1+\sqrt{1-\tau}}{2})$ and $h = -x\log_2 x - (1-x)\log_2(1-x)$ [22]. This can be computed by obtaining the square roots of the four eigenvalues, $\lambda_i = \sqrt{\varepsilon_i}$, of the matrix $\rho_{AB}\widetilde{\rho_{AB}}$ (see Alg. 4). The reduced density matrix of sites $\mathcal{A}$ and $\mathcal{B}$, ρ_{AB}, is calculated by tracing out the rest of sites of a chain in a state ρ, i.e. $\rho_{AB} = tr_{rest}(\rho)$, and $\widetilde{\rho_{AB}} = (\sigma_y^A \otimes \sigma_y^B)\rho_{AB}^*(\sigma_y^A \otimes \sigma_y^B)$. By arranging these λ_i in decreasing order, τ is obtained as

$$\tau = [max(\lambda_1 - \lambda_2 - \lambda_3 - \lambda_4, 0)]^2. \tag{2.23}$$

$EOF_{AB} \in [0,1]$ so that two maximally entangled qubits $\mathcal{A}$ and $\mathcal{B}$ present an $EOF_{AB} = 1$. This is attained when the state between $\mathcal{A}$ and $\mathcal{B}$ is pure, entangled and there is no entanglement with the rest of the chain.

Data:
$\rho_{AB}[4]$: reduced density matrix of qubit A and B
$\sigma[4]$: $\sigma_y^A \otimes \sigma_y^B$
T: total time
Result: entanglement $EOF(t)$
$t = 0$;
for $t < T$ **do**
  M=$\rho_{AB}\sigma$CONJG$[\rho_{AB}]\sigma$;
  Diagonalise M with LAPACK subroutine $\Rightarrow \{E_1, E_2, E_3, E_4\}$;
  for $i<4$ **do**
    λ_i =SQRT$[E_i]$;
  end
  Sort $\{\lambda_i\}$ in decreasing order.;
  τ =MAX$[(\lambda_1 - \lambda_2 - \lambda_3 - \lambda_4)^2, 0]$;
  $x = 1$+SQRT$[1 - \tau]/2$;
  $EOF(t) = x$LOG$[x] - (1 - x)$LOG$[1 - x]$;
end

Algorithm 4: Calculation of EOF

Fidelity and EOF can be useful quantities when used together. In some applications using EPR pairs as a resource, such as teleportation or superdense coding, it does not suffice the promise that the pair of qubits is maximally entangled and it is relevant to know which of the four Bell states is being shared. In such scenarios, testing for entanglement using EOF and then identifying such state using fidelity against the four Bell states may be a convenient procedure.

2.3 Perturbations

The manufacture of any quantum device, no matter how precise its fabrication is, will be subject to errors. Quantum phenomena that underpin the desired applications of such devices might get heavily disturbed by these errors, due to extreme sensitivity of the phenomena to the errors. On one hand, we wish to account for time-independent perturbations that affect the on-site energies of the spins and their interactions as fabrication defects. Such errors are included in the system through a set of R (typically $R \sim 1000$) random disorder realisations over which we will average the out-coming results, i.e. energy spectrum, fidelity or EOF. On the other hand, we also consider asynchronous state injections for the cases when the system is initialised from more than one site.

2.3.1 Diagonal disorder

One approach to model local fabrication errors is to consider energy fluctuations. We do this by adding random disorder to the diagonal terms of the Hamiltonian. Diagonal disorder encompasses both the case of local fabrication defects and local fields fluctuations, which has been shown to be some of the most damaging source of static decoherence for the single excitation sector in spin chains [64].

The second term of the Hamiltonian from Eq. 2.12 is set to have $\epsilon_i = Er_i\gamma$, where r_i is a random number from a uniform distribution between $-1/2$ and $1/2$, E is a dimensionless positive parameter that fixes the scale of the disorder and γ is one of the characteristic energies of the system (e.g. the coupling energy between sites). It is important to note that the perturbation added to the diagonal terms of the Hamiltonian involving basis vectors with more than one excitation, $\langle 0..1_i1_j..0|\mathcal{H}|0..1_i1_j..0\rangle$, will be calculated as the sum of the random disorder added to the single excitation vectors, $\epsilon_i + \epsilon_j$.

2.3.2 Off-diagonal disorder

Our second approach to model fabrication errors and local defects accounts for static coupling errors introduced in the off-diagonal terms of the Hamiltonian matrix. Such perturbation represents random disorder in the couplings of the chain, $J_{i,i+1}$. In order to do so we modify the first term of the Hamiltonian from Eq. 2.12 by setting $J^{eff}_{i,i+1} = J_{i,i+1} + Er_{i,i+1}\gamma$, where $r_{i,i+1}$, E and γ have the same meaning as in the previous section.

2.3.3 Time Delays

When dealing with the entangling protocols shown in Chapter 5, for some cases the ideal injection scenario will be the injection of excitations simultaneously at different sites a and b, e.g. the state $|1_a0...01_b\rangle$. We want to assess how damaging for those protocols it is to inject such excitations in a slightly asynchronous way. This is attained by adding a time delay $t_D = Dt_E$ being D the scale of the delay ($0 \leq D \leq 1$) and t_E the original operation time (in our case, the time needed for the protocol to complete the entangling operation).

This injection is performed in two parts. First, we initiate the time evolution of the initial state that has an excitation at site a, $|00..1_a..00\rangle$. Right before the delayed time, at t_D^-, we retrieve the overall state of the system $|\Psi(t_D^-)\rangle$. We can write $|\Psi(t_D^-)\rangle = \sum_i^N c_i|\Phi_i^{1ex}\rangle$ (with N being the total number of sites and equal to the vectors of the one excitation subsector) where $\sum_i^N |c_i|^2 = 1$ and $|\Phi_i^{1ex}\rangle = |00..1_i..00\rangle$. Then when injecting a second excitation at site b, we need to map these coefficients c_i into the two excitations vectors, $|\Phi_v^{2ex}\rangle = |00..1_i1_b..00\rangle$ with $i \neq b$, to find $|\Psi(t_D^+)\rangle = \sum_v c_i|\Phi_v^{2ex}\rangle$. It is important to note that in our calculations the time delay is not long enough to allow numerically zero probability of the first injected state at site a to be located at site b by the time the second state is injected, hence the

aforementioned treatment is an accurate approximation and no renormalisation is required.

Data:
R: number of realisations
E: scale of the disorder
$Basis_k[N]$: site basis vectors
Result: perturbed Hamiltonian H
H=0 (initialise Hamiltonian matrix);
if *diagonal disorder* **then**
  if *k<N* **then**
    r_k =RAND$(-1/2, 1/2)$;
    $H[k,k] = r_k * E * J_{max}$;
  else
    for *s in* $Basis_k[N]$ **do**
      if $Basis_k[s] = 1$ **then**
        $H[k,k] = H[k,k] + H[s,s]$;
      end
    end
  end
end
if *off-diagonal disorder* **then**
  for *i<(N-1)* **do**
    r_i =RAND$(-1/2, 1/2)$;
    $J[i] = J[i] + r_i * E * J_{max}$;
    Build Hamiltonian as in **Algorithm 1.;**
  end
end

Algorithm 5: Addition of fabrication defects

Chapter 3

Spin chains as quantum buses

In this chapter we examine the use of spin chains as quantum wires or buses. One of the approaches to engineering the system to allow for quantum state transfer (QST) is considered in detail. We consider the robustness of the wire against random local errors, and how such disorder affects the state transfer. We demonstrate that when diagonal perturbations are high enough, spin chains are good systems in which to observe Anderson localisation signatures. Part of this work has been published in: **R. Ronke, M. P. Estarellas, I. D'Amico, T.P. Spiller & T. Miyadera**, "Anderson localisation in spin chains for perfect state transfer", Eur. Phys. J.D. **70**, 189, (2016).

It is undeniable that telecommunications are nowadays key in our daily life. Sound, video, images, and any sort of data are being massively and constantly shared through several communication protocols as data packets. Physical means to transmit the information are required, both for short- and long-distance connections. Classical communications run through several platforms such as radio channels, optical fibers or copper wires that transfer the bits that form each data packet in the form of electromagnetic waves or optical pulses. Nevertheless, in the era of Internet, fiber optics has become the preferred media for long range communications due to its ability to support large bit rates (hundreds of gigabits per second) and their robustness against electromagnetic interference.

On a smaller scale, computer hardware needs a means to connect and communicate between its various components, which will tend to sit very close (the size of current Intel microprocessors is of $37.5\,\mathrm{mm}^2$ with a feature size of $22\,\mathrm{nm}$ [122]). Any processing unit contains various registers, $\{Ri\}$, that temporarily store data before and after being processed and over which the logical operations that define the overall computation are applied. In example, the data and the instructions to be implemented in a processing unit need to arrive to the register location, communicate with the ALU (or logical arithmetic unit) and go back to the main memory after the computation. In classical computer architecture this is generally attained with the use of data buses. Such components allow for the transmission of a certain width (generally 8, 16, 32 or 64 bits) of data or instructions between two locations. As the transfer is done over short distances, the bus device is generally implemented

through copper wires.

In the context of quantum technologies, quantum communication soon became a field by itself. Certainly, a quantum counterpart to transfer information is on demand and an effective way to transfer qubits is required, as stated by the last two requirements of DiVincenzo criteria [54] (see Section 1.1.3). As in its classical counterpart, long-distance quantum communication has been dominated by photonics. Even though single photons may not be the preferred qubit implementation out of which a quantum computer can be built, they do provide several advantages when used for quantum communication applications. These moving entities can be guided through optical fibers for long distances with very low loss rates. This is a clear advantage as there already exists a classical worldwide network's built out of optical fibers, reducing the cost of designing and developing a new quantum communication infrastructure.

As with classical computers and conventional data, a quantum computer processor will need buses to be able to transmit quantum data between its components or registers without losing its state coherence. Clearly the use of photonics for such short range communication presents some drawbacks. Quantum computer hardware is generally built out of static qubits (e.g. superconductors, ion traps or quantum dots) and the use of photons will require to convert the solid qubit state into states of light and vice-versa. This type of encoding/decoding may be worth it for long distances due to the advantages of the use of photons as qubits, as already commented, but it may add an extra cost on smaller scales. Likewise, the moving of solid-state qubits from one location to another needs a precise control of the system and it implies that an extra source of systematic errors will be present. In order to overcome these limitations, Bose pioneered the idea of using spin chains as quantum data buses [61, 120], an idea that attracted lot of attention and was soon investigated by many [63, 66, 123]. Bose's main motivation was the possibility of building a wire with the same type of solid-state qubit than the rest of the hardware. The theoretical model behind spin chains can indeed be applied to several solid-state implementations of permanently coupled qubits, something that makes them interesting systems to study a wide variety of quantum protocols. Another of the advantages of using the spin chains as quantum wires is that they can be set to operate through their natural dynamics, hence with the requirement of a minimal external control.

The applicability of chains of solid-state qubits as data buses requires a method to transport an arbitrary quantum state from one site to another with little external control. There are several strategies to allow for good state transfer, however we will mainly focus on one of them to enable what is called 'perfect state transfer' (PST) and explore its capabilities. As a part of such exploration we will examine the robustness of spin systems for transfer operations and investigate the presence of Anderson localisation in the strong disordered regime.

3.1 State Transfer

The transfer of a quantum state over a spin chain implies that the state that sits at one site is reliably transfered to another site of the chain. We will name these two participant sites register *rA* and register *rB* and assume they are separate by a finite distance that can be covered by a set of N interacting qubits, as shown in Fig. 3.1 for the case of a linear chain.

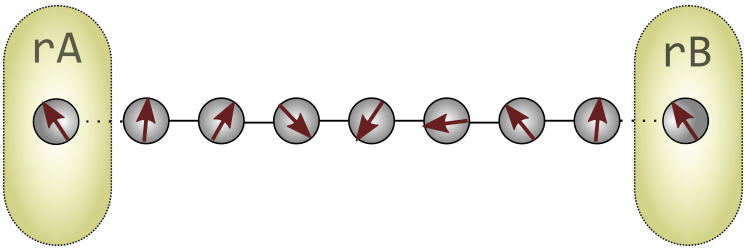

FIGURE 3.1: General linear spin chain acting as a quantum bus between registers *rA* and *rB*.

This protocol can be outlined by the following steps,

1. Placement or injection of the initial state at the register *rA*.
2. Time-evolution of the system for a finite time, $t_{\mathcal{T}}$
3. Extraction or measurement of the state at the register *rB*.

A good way to assess the performance and information transport quality of the quantum bus under this protocol is by the calculation of the fidelity $\mathcal{F}$ (see Section 2.2.1). The state transfer is considered to be ideal or perfect when the evolution of the initial state (quantum state in *rA*) is arranged to achieve $\mathcal{F}(t_{\mathcal{T}}) = 1$ against the final state (quantum state in *rB*) at a known time $t_{\mathcal{T}}$.

The initial state evolves with the natural dynamics of an N-site spin chain described by the time-independent Hamiltonian of the system, which in this thesis is the one considered in Eq. 2.12 is considered (see Section 2.1.1). Among various strategies, one of the keys to attain optimised transfer fidelities relies on the engineering of the system interactions. But before looking at this let us first consider the transfer capabilities of unmodulated systems, that is, with uniform interactions [120].

3.1.1 State transfer in linear chains

We now wish to explore the transfer abilities of linear uniform chains. We consider an N-sites chain with all their spins, i, initially down (or in state $|0\rangle = |0_1 0_i ... 0_N\rangle$) to transfer an injected state $|\Psi(0)\rangle = |1\rangle_{rA} \otimes |0\rangle_{rest}$ from register rA to rB. This means that after a given time $t_{\mathcal{T}}$, the state will be $|\Psi(t_{\mathcal{T}})\rangle = |1\rangle_{rB} \otimes |0\rangle_{rest}$.

Let us consider a very simple case: a 3-sites chain with equal couplings $J_{i,i+1} = 1$. In Fig. 3.2 we present the fidelity, $\mathcal{F}(t)$, of the overall state $|\Psi(t)\rangle$ against the initial

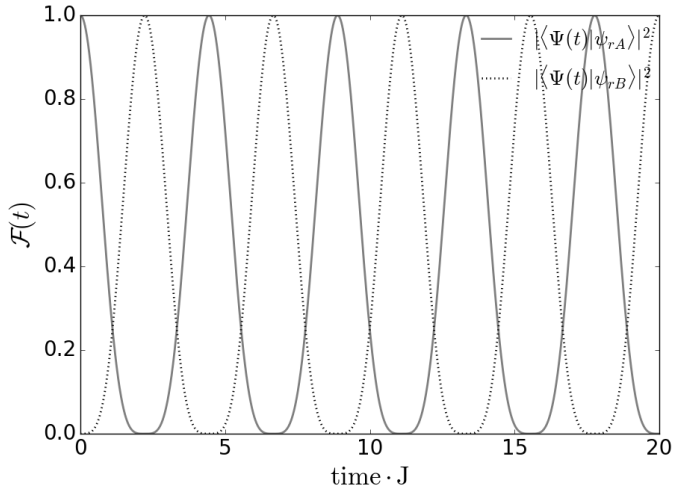

FIGURE 3.2: Dynamics of a 3-sites spin chain transferring an excitation between registers *rA* and *rB*. Solid profile is the fidelity of the state against the initial state (excitation at site rA). Dashed profile is the fidelity of the state against the desired state (excitation at site rB)

state at $|\psi_{rA}\rangle$ (solid profile) and the transfered state $|\psi_{rB}\rangle$ (dashed profile). Both profiles have a periodic behavior and we observe that as the solid profile decreases away from unity, the dashed profile does increase up to a maximum ($\mathcal{F}(t_{\mathcal{T}}) = 1$), therefore the state is perfectly transferred from site rA to rB. It is however clear that the dynamics will not stop there and the excitation will keep oscillating back and forth between sites, due to its periodic nature. Yet, if the value of $t_{\mathcal{T}}$ is known (for instance, through calibration of the device), the state can be measured or extracted at this time (or any multiple) by the user or the implicated computer component (see Section 6.1 for further discussion on this).

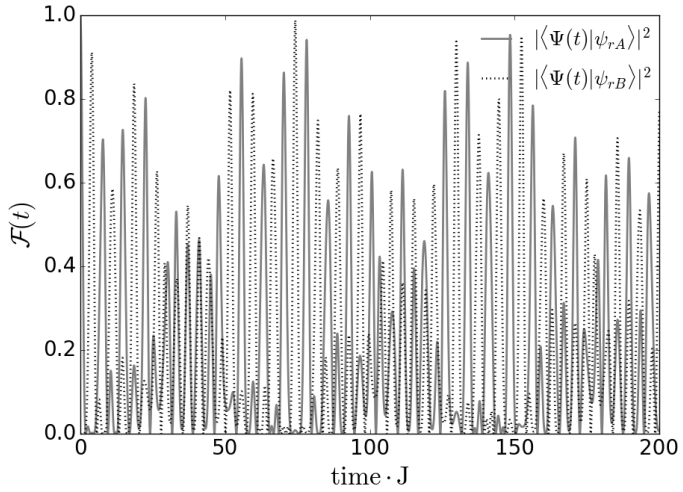

FIGURE 3.3: Dynamics of a 6-sites spin chain transferring an excitation between registers *rA* and *rB*. Solid profile is the fidelity of the state against the initial state (excitation at site rA). Dashed profile is the fidelity of the state against the desired state (excitation at site rB)

Unfortunately, this behaviour is not scalable and the time needed for the transfer, $t_{\mathcal{T}}$, grows exponentially with N [120]. Additionally, the dynamics of the system loses its periodicity and the maximum transfer fidelity attained is not unity anymore. Nonetheless, some exceptions are found for certain chain sizes ($N = p-1$, $N = 2p-1$ and $N = 2^m - 1$, p being a prime) which yield to what is called "pretty good state transfer", with fidelities approaching to unity as long as one waits enough time, an effect presumably related to number theory [124]. This can be observed from the 6-sites chain example shown in Fig. 3.3 ($N = p-1$), in which is possible to reach a good transfer quality if enough time has passed ($t_{\mathcal{T}} \sim 75$ J^{-1}). However, when increasing the chain size up to $N = 14$ (Fig. 3.4) the transfer fidelity does not approach to unity even when the time window considered is of three orders of magnitude higher than the one for the $N = 3$ sites example.

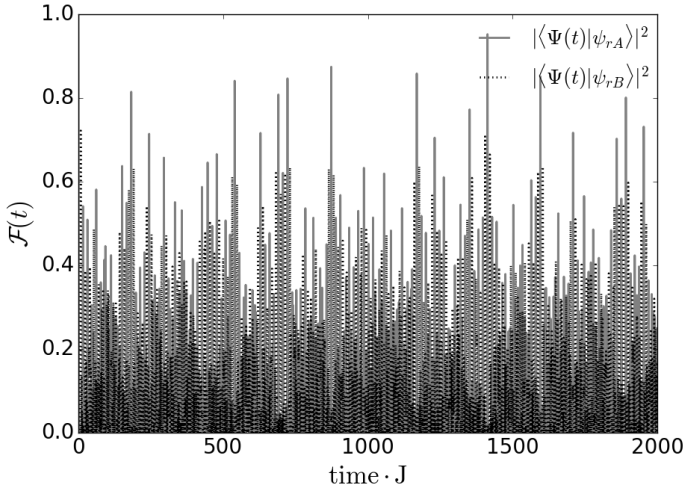

FIGURE 3.4: Dynamics of a 14-sites spin chain transferring an excitation between registers *rA* and *rB*. Solid profile is the fidelity of the state against the initial state (excitation at site rA). Dashed profile is the fidelity of the state against the desired state (excitation at site rB)

3.1.2 State transfer in other geometries

Even though the first picture of a data bus that comes to one's mind is that of a linear chord or wire (similarly to the one presented in Fig. 3.1), one could also conceive the possibility of transferring information through more complex geometries. For instance, some computation could need a transport device that distributes a state among different parties. This would imply a communication based on broadcast topology, *1 to N*, instead of a point-to-point, *1 to 1*, communication.

Multiple M-branched systems such as the one in Fig. 3.5 (also called spin star) allow, in example, an excitation initially injected at site rA, $|\psi(0)\rangle = |1\rangle_{rA} \otimes |0\rangle_{rest}$, to be routed to a certain rB_i by tuning the couplings or adding local magnetic fields [87, 125]. Interestingly, it also allows to distribute the initial state $|\psi(0)\rangle$ between all the rB_i sites. However, the probability of the transfered state at time $t_{\mathcal{T}}$ will be shared

between all the branches. This means that the overall state of the system once the transfer is complete will be in a superposition of $|\Psi(t_{\mathcal{T}})\rangle = \frac{1}{\sqrt{M}} \sum_i^M |1\rangle_{rB_i} \otimes |0_{rest}\rangle$. This is a type of multipartite entangled state called W state and it is maximally entangled between the M parties due to the presence of entangled Bell states between pairs. Such states are used as a popular entanglement resource for many quantum information applications due to its robustness against noise and qubit loss [126, 127]

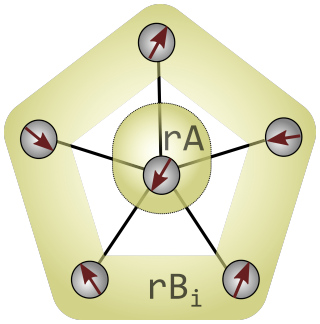

FIGURE 3.5: Example of a spin star system with one hub, rA, and five branches, rB_i.

Examples like this one form altogether a zoo of different protocol topologies with various purposes and applications. In fact, quantum information processing, similarly to what is encountered in classical networks, will need components such as routers, splitters or switches that process and help distributing the quantum information during its communication. For such purposes, higher geometric arrangements other than linear chains are good candidates and are also being explored [62, 85, 128, 129]. It is important to note that similarly to what happens with linear systems, these more complex structures will also have scalability issues in their transfer fidelities. Fortunately there are design schemes that can help to overcome these limitations for both linear and branched systems.

3.1.3 Perfect State Transfer

There is a clear potential of spin chains and spin networks to work as quantum data buses, yet the previously presented uniform coupling scheme has been shown to have a scalability issue. In order to overcome this hurdle, several spin chain designs providing good throughputs on state transport through arbitrary distances have been proposed. When these schemes allow for an ideal transfer of the state (fidelity of the transfer is unity), we say that they allow for *perfect state transfer* (PST).

Quantum state transfer with high fidelity can be enabled through many strategies. Examples include the application of local magnetic fields [130], the use of different state encodings such as dual- and multi-rail encoding [70] or wavepacket encoding [131], or the use of adiabatic techniques [132]. Last but not least, one of the most popular ways to enable the chain to allow for PST is by the engineering of spin-spin interactions.

Before going more into detail about how the couplings can be engineered, let us first go through the requirements needed for a system to present PST. In fact, many of the previously mentioned schemes have one thing in common and it is that they rely on a system that is mirror-symmetric. This symmetry is closely related to a characteristic energy spectrum and it can be engineered through the interactions or the geometry of the network. In such designs, one of the consequences of mirror symmetry is a periodic dynamics of a state, $|\psi\rangle$, that (following the example from Fig. 3.1) moves between the initial injection site rA and its mirror, rB, such that,

$$e^{-i\mathcal{H}2t_{\mathcal{T}}}|\psi_{rA}\rangle = e^{-i\mathcal{H}t_{\mathcal{T}}}e^{i\theta}|\psi_{rB}\rangle = e^{i2\theta}|\psi_{rA}\rangle, \tag{3.1}$$

being $e^{-i\mathcal{H}t}$ what defines the time evolution of the initial state with respect the Hamiltonian $\mathcal{H}$ of the system (see Section 2.1.1 for more detail), and $|\psi_{rA}\rangle$ and $|\psi_{rB}\rangle$ the states corresponding to an excitation at sites rA and rB, respectively. The system takes time $t_{\mathcal{T}}$ to transfer a state from register rA to its mirror position rB and, by symmetry, twice that time for the state to go back to its initial position [123].

When referring to these systems, we will call the time $t_{\mathcal{T}}$ needed to transfer the state from the initial position to its mirror, the *mirroring time*, t_M. The dynamics of the system is therefore periodic up to a phase 2θ (which is a global phase, hence can be corrected) and period $2t_M$. This mirroring phenomenon arises from the fact that for a particular coupling condition the spin chain can be mapped onto a macroscopic spin, with the mirroring corresponding to its precession [65, 123]. Hence, we can operationally define the mirror operator M having the following effects to each term, $a, b, y, z \in \{0, 1\}$, in any arbitrary superposition state of the chain:

$$M|a\rangle_1|b\rangle_2...|y\rangle_{N-1}|z\rangle_N = |z\rangle_1|y\rangle_2...|b\rangle_{N-1}|a\rangle_N \tag{3.2}$$

Any initial state $|\Psi(0)\rangle$ can thus be decomposed into its even and odd parts under the mirror operator M, such that

$$|\Psi(0)\rangle = \frac{1}{\sqrt{2}}(|\Psi_+(0)\rangle + |\Psi_-(0)\rangle), \tag{3.3}$$

being $|\Psi_\pm(0)\rangle \equiv \frac{1}{\sqrt{2}}(|\Psi(0)\rangle \pm M|\Psi(0)\rangle)$. Thus the Hamiltonian eigenstates (which are also eigenstates of M as $[M, H] = 0$) can be decomposed as superpositions of even and odd energy eigenstates $|\Psi_\pm(0)\rangle \equiv \sum_{\pm k} a_{\pm k}|\varphi_{\pm k}\rangle$. Then for the evolved state at time t_M to have unit fidelity against the mirrored initial state $M|\Psi(0)\rangle$, up to a global phase, it has to be of the form

$$|\Psi(t_M)\rangle = \frac{e^{i\theta}}{\sqrt{2}}(|\sum_{+k} a_{+k}|\varphi_{+k}\rangle - \sum_{-k} a_{-k}|\varphi_{-k}\rangle) \tag{3.4}$$

It is therefore clear that this mirroring phenomenon is closely related to the properties of the eigenstates. The energy spectrum plays indeed an important role in the

PST dynamics. The general state of the system after a full period from Eq. 3.1 can be rewritten in terms of the eigenstates, $|\varphi_k\rangle$, such as,

$$|\Psi(2t_M)\rangle = \sum_k a_k e^{-iE_k 2t_M}|\varphi_k\rangle = e^{i2\theta}\sum_k a_k|\varphi_k\rangle \tag{3.5}$$

From which the condition $E_k 2t_M - 2\theta = 2m_k\pi$, with m_k being integers, must be fulfilled in order to show PST. Eliminating θ between two states r and s we can rewrite this condition in the form,

$$(E_s - E_r)2t_M = 2(m_s - m_r)\pi. \tag{3.6}$$

And by calculating the ratio between two sets we can eliminate the common factors such as,

$$\frac{E_s - E_r}{E_v - E_w} = \frac{m_s - m_r}{m_v - m_w} \in \mathbb{Q}, \tag{3.7}$$

and because m's are integers, we can deduce that the spectrum needs to be such that the ratios of the differences between eigenvalues are rational numbers ($\mathbb{Q}$). In fact, it can be shown that this condition is not fulfilled for linear uniform chains with $N \geq 4$ [65] and the energy differences stop being commensurate, causing the dynamics to deviate from PST.

The couplings can be arranged in different ways to allow for perfect or nearly-perfect state transfer. Some of them require the engineering of *all* the spin-spin interactions, $J_{i,i+1}$, [63, 68, 133] and others only ask for control of the boundary interactions, $J_{1,2}$ and $J_{N-1,N}$ [134–137]. Other proposals exploit this boundary control so that the distant spins get entangled in the ground state (named long-distance entanglement) and communication can be achieved through teleportation [77, 79, 82]. We here will focus on an arrangement example proposed by Nikolopoulos and Christiandl [65, 66] where the $N-1$ interactions of an N-sites linear chain are defined as,

$$J_{i,i+1} = J_0\sqrt{i(N-i)}, \tag{3.8}$$

with i being the site number.

In any practical system there will be a maximum spin-spin coupling strength, independent of the length N and set by a characteristic value for the particular physical realisation of the spins. Therefore, to address this practical constraint, we keep the maximum coupling value $J_{max} = 1$ constant as N is varied (even though not all authors working on such models have considered this physical constraint [62, 66, 138]). J_{max} is then our unit of energy and its coupling occurs in the middle of the chain. As a result $J_0 = 2J_{max}/N$ for even ($J_0 = 2J_{max}/N\sqrt{1-1/N^2}$ for odd) length chains and all the couplings $J_{i,i+1}$ are symmetric about the center ($J_1 = J_N, J_2 = J_{N-1}, ..., J_i = J_{N-i+1}$).

The Hamiltonian of a chain with engineered couplings according to Eq. 3.8 fulfills the energy spectrum condition (Eq. 3.7) and the single excitation energy levels are equidistant, therefore their ratios are rational. This distribution is then enough to impose the mirror symmetry with a periodic dynamics and, therefore, ensure PST for any arbitrary chain length.

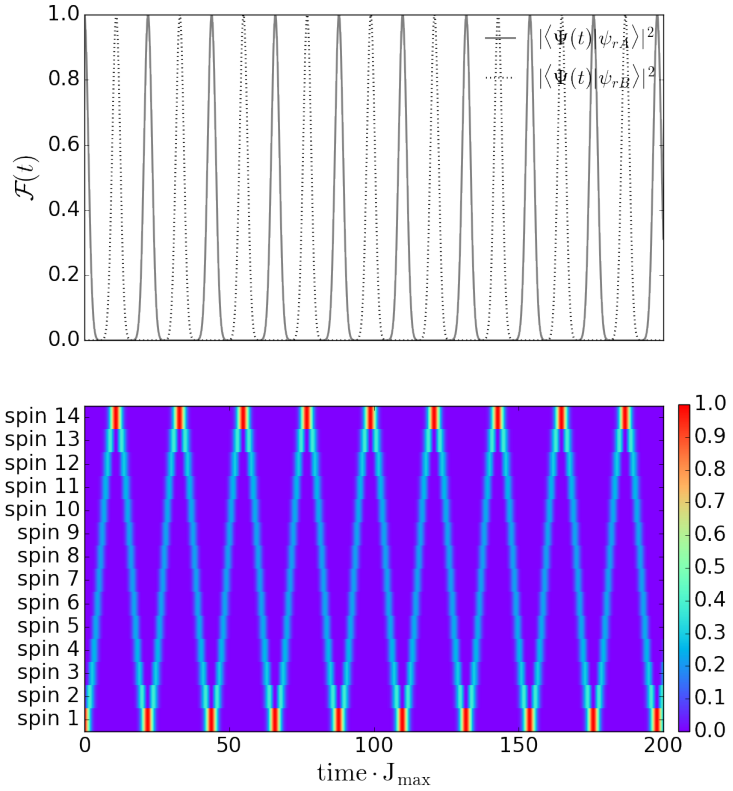

FIGURE 3.6: Dynamics of a 14-sites PST-engineered spin chain transferring an excitation between registers *rA* and *rB* (upper panel). Site occupation probabilities for all sites i against time (lower panel).

Throughout the rest of this chapter we will be considering PST systems under this scheme. Even though in our examples here we have chosen a simple initial state due to its convenience, any arbitrary state, including states with more than one excitation and entangled states, is allowed to be used in this protocol [123, 139]. The time scale for an excitation to exhibit PST from one end of a chain to the other is defined by $t_M = \pi\hbar/2J_0$. This time scales with N when J_{max} is maintained. In all cases the full periodicity of the system evolution is given by $t_F = 2t_M$.

The previously presented $N = 14$ uniform linear chain (Fig. 3.4) provides a suitable system where to test the effect of engineering the interactions between sites according to Eq. 3.8. We use this as an illustrative example and present the dynamics of the new chain in Fig. 3.6. The upper panel shows the fidelities of the initial (solid profile) and mirror (dashed profile) state. The lower panel maps the site occupation probabilities at all the times for all the sites, labeled as "spins", being the red color

areas the ones containing the maximum probability. It can be observed from the dynamics and the site probabilities that the transfer of the state is completed at all the periods. Therefore, it is indeed demonstrated that the enforcing of mirror symmetry through engineering of the couplings allows for PST.

From the lower panel of Fig. 3.6 we observe that the site-occupation probabilities only attain the maximum (red) probability at the edge sites. This implies that the excitation does not travel along the chain as a localised peak. Such behaviour is backed from the eigenstate occupation probabilities, $\mathcal{P}_{i,k}$ (see Section 2.2.2), presented in Fig. 3.7, which spread across the chain. The spreading allows the delocalisation of the initial injection and its later (t_M) relocalisation at site $N = 14$ when the phases of all the eigenstate amplitudes arrange themselves suitably. The inset of Fig. 3.7 also shows how the PST engineering scheme used here imposes the required equidistant energy spectrum. We will come back to the discussion of the eigenstate and energy spectrum later in Section 3.2.3.

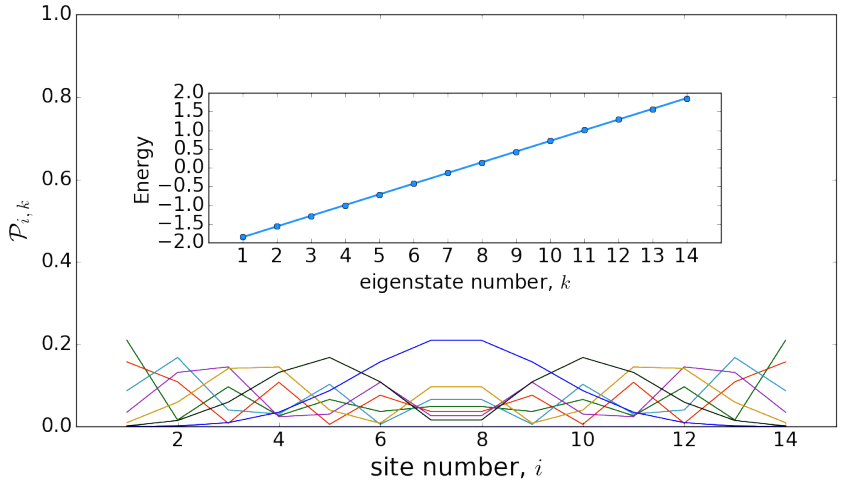

FIGURE 3.7: Eigenstate occupation probabilities of a 14-sites PST-engineered spin chain and its energy spectrum (inset) for the first excitation subspace.

When other geometries other than linear systems come into play, the engineering of the couplings can still allow for PST. Spin networks distributed as a certain category of graphs can be mapped into linear chains through engineering of the graph couplings. This would allow for *point-to-point* perfect communication between the edges or branches [65], something that can lead to some interesting behaviours such as the creation of entangled states through the dynamics of branched systems [129].

3.1.4 Effects of perturbations

We have seen that some spin chain designs allow for the perfect transfer of an arbitrary state between two sites or more under ideal conditions. However, no real

implementation will be perfectly manufactured or completely isolated from external disorder, and the dynamics of the system will subsequently be disturbed. Time-dependent factors such as random fluctuating fields or qubit coherence times are subject to the type of implementation chosen to fabricate the spin chain (see discussion in Section 1.2.3). A more general form of noise errors that is more independent of the platform but still unavoidable is the random static disorder such as the one related to the fabrication process of the chain or the presence of non-uniform local fields. The robustness of PST designs against this type of errors has been widely studied [64, 140–144] showing that such devices have a considerable level of robustness against moderate errors, e.g. transfer fidelities of around 80% are attained with on-site errors of around 10% and coupling errors of 5% the maximum coupling J_{max} [64].

Detailed studies [64, 73, 142, 145–147] conjecture that the effects of static random perturbations to the state transfer scale with the size of the chain. We will show that this is a direct consequence of the presence of localisation signatures that appear when the size of random errors is high enough and the system is considerably large. In the next part of this chapter we explore this phenomenon and relate it to Anderson localisation. We therefore investigate the question of if and how random defects would affect the relevant transmission properties of PST spin chains for different levels of disorder and spin chain sizes.

3.2 Disorder and Anderson localisation

The exponential decrease of conduction due to the presence of static random fluctuations in solids had been observed in several experiments, mainly in ones related to spin diffusion [148–150]. The classical Boltzmann scattering description was insufficient to explain the deviations found in the resistance from Ohm's law for increasing sample sizes [151]. It was not until 1958 that this phenomenon was formally explained by P. W. Anderson [152] and not until ten years later that his arguments were entirely accepted and followed by many [151, 153–155]. Since then, its reach and influence has been greatly extended in condensed matter physics, to many systems and phenomena (examples include the integer quantum Hall effect [156], classical waves [157, 158], photonics [159, 160] or Bose-Einstein condensates [161, 162]).

The presence of weak disorder leads to a decrease of spin diffusion or electrical conductivity, something related to the electrons scattering by the impurities of the random potential. For strong random disorder, the transport is halted and the wavefunction of an electron in a periodic lattice is localised and characterized by an exponential decay, $|\psi(x)\rangle \sim e^{|x-x_o|/\xi}$, that falls with distance, x, from the site of maximum amplitude, x_0. ξ is the localisation length, related to the degree of localisation, being a state with $\xi \to 0$ strongly localised and a state with $\xi \to \infty$ completely extended. This localisation behaviour could not be predicted by classical theory, which assumes that electrons move through classical trajectories between collisions. Such

approximation is valid as long as the mean-free path, l, is bigger than the Fermi wavelength, λ_F, (corresponding to the electron responsible of the charge current, with energy E_F) however when disorder is high enough then $\lambda_F \sim l$ and quantum effects become prominent. Indeed, Anderson introduced that the fundamental reason for which this localisation and transfer suppression arise is associated to quantum interference of wavefunction components that are scattered by the random potential.

When weak disorder is present in a conductor, the resistance increases as the result of weak localisation [153]. This type of localisation is due to a destructive quantum interference of the electron wavefunction with itself. If no interference is present, the total probability of the electron to go from x_o to x is $\sum_k A_k^2$, being the k's all the possible wave paths and A their amplitudes. When $x_o = x$, there will be two time-reversed paths, k_1 and k_2, starting at, x_o, and returning to the same point which contribute $4A_{k_1=k_2}^2$ to the total probability. This increase of the probability to go back to its initial site due to interference in the weak disorder regime is enough to decrease the conductivity.

In the limit of very strong disorder, in addition to the previous effects, the eigenstates localise at positions where the random potential forms a deep well. Their overlap with other states will be reduced, as localised states will be dominant in some regions but negligible in others. Due to this small state overlap and big energy differences, the hopping amplitudes are not enough to delocalise the particles and the transport is affected. This behaviour scales with the system size, N, in all dimensions as it becomes more prominent.

The theory of Anderson localisation predicts localisation of all states of one-dimensional disordered lattices [163]. However it should be noted that in one dimensional finite systems disorder does not necessarily imply the complete vanishing of extended states, as discussed by Pendry in the case of 'necklace' states [164]. Therefore there are important theoretical motivations for considering non-uniform and finite systems, along with the fact that experimental systems are finite in extent.

In this study we will simulate a random potential including diagonal disorder to the Hamiltonian according to Section 2.3.1. In what follows we will restrict ourselves to the dynamics of a single excitation injected at the beginning of the chain. Such dynamics, in an ideal condition, is perfectly periodic and transfers the state back and forth from its initial to its mirror position. Because the appearance of Anderson localisation can be observed from the spatial localisation of the state wavefunction, from the transport of the quantum particle, or from the eigenstate and eigenenergies spectrum, we will here explore all of these points for a different range of chain sizes and disorder strengths.

3.2.1 Spatial localisation

For infinite one dimensional systems with diagonal disorder, Anderson localisation implies that any initially localised state remains so at all times. For example, in a

semi-infinite discrete chain with one excitation started at the end site $i = 1$ and an overall state of the form $|\Psi(t)\rangle = \sum_{i=1}^{\infty} c_i(t)|\Phi_i\rangle$, with $|\Phi_i\rangle$ being the site vectors for the one excitation subspace, the localisation condition can be written as

$$\sum_{i=1}^{\infty} \mathcal{P}_i i < \infty, \tag{3.9}$$

at all times t and with $\mathcal{P}_i = |c_i(t)|^2$.

One of the cases where the semi-infinite condition is satisfied is when the site occupation probabilities follow a power decay,

$$\mathcal{P}_i \sim i^{-(2+\delta)}, \tag{3.10}$$

for all times and positive δ.

Even though such consideration is done for infinite-length chains, we will stick to this form of scaling dependence for finite scenarios. In order to do so we need to normalise the occupation probabilities, $\mathcal{P}_i$. For large values of chain length N, the normalisation factor, α_N, can be approximated to $\alpha_\infty = \frac{1}{\zeta(2+\delta)}$, being ζ the Riemann Zeta Function, as $\zeta(r) = \sum_i^{\infty}(1/i^r)$. This way, the normalised probability takes the form,

$$\mathcal{P}_i = \alpha_N \; i^{-(2+\delta)} \tag{3.11}$$

For $(\delta = 0)$, we find the critical normalisation $\alpha_{\infty Cr} = \frac{1}{\zeta(2)}$. Similarly, for the whole range of N (100 to 1000) in our study, α_{NCr} can be approximated to $\alpha_{\infty Cr} \sim 0.6$, so we can plot one critical probability distribution for comparison with all the numerical simulations at different N values, from 100 to 1000.

We wish to explore how the effect of random disorder scales with the chain size. In Fig. 3.8 we present the effective steady state site occupation probabilities $\overline{\mathcal{P}_i}^{ss}$ (see definition below) as a function of the site number, i, for a range of chain lengths $N = [100, 1000]$, with a strength of disorder $E = 1.0$ (see Section 2.3.1 for more detail).

In order to approximate a steady state condition, the dynamics of each of the systems is evolved to $t = 5t_M$ when the excitation is initially injected at site $i = 1$. Results of the site occupation probabilities, $\mathcal{P}_i$, are then averaged over 100 time steps that go from $t = 5t_M$ to $t = 7t_M$:

$$\overline{\mathcal{P}_i}^{ss} = \frac{\sum_{t=5t_M}^{7t_M} \mathcal{P}(t)_i}{100}. \tag{3.12}$$

A plot of $\alpha_{\infty Cr} \; i^{-2}$ is included. This line gives the accepted cut-off for Anderson localisation in the limit $N \to \infty$. Identifying everything below the cut-off as localised, and everything above as not, we can conclude that chains with N about ~ 500 and above exhibit Anderson localisation under this criterion (according to Eq. 3.9) for an excitation initially at the chain end.

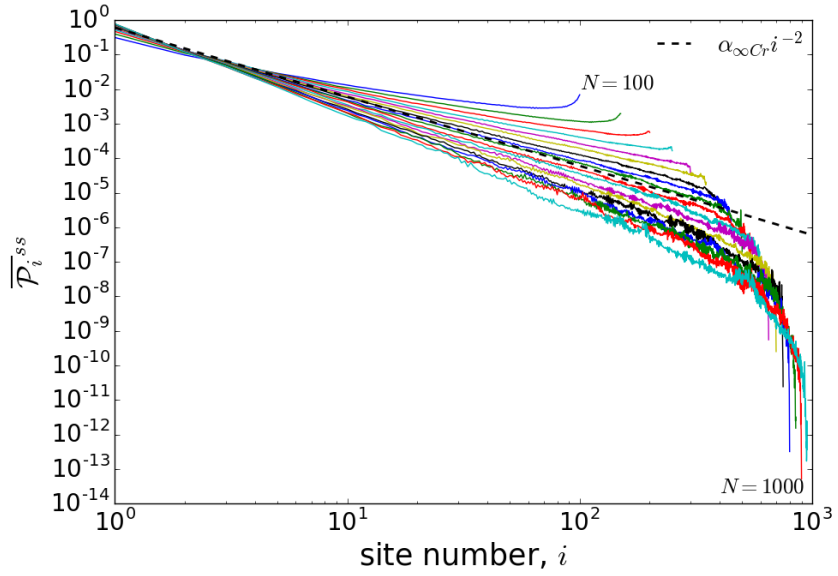

FIGURE 3.8: Effective steady state site occupation probabilities versus chain site, i, for a range of chain lengths $N = [100, 1000]$ and disorder of strength $E = 1.0$, when the excitation is injected at site 1. For comparison, the critical line given by i^{-2} is added (with a normalisation factor $\alpha_{\infty Cr} = 0.6$).

Given the approximate straight line behaviour of the data plots, in terms of an analytic approximation to the probabilities given by $\mathcal{P}_i = \alpha_N i^{-(2+\delta)}$, we can comment that δ exhibits slow variation with N. For small N, δ is negative and increasing, crossing the threshold for localisation ($\delta = 0$) at about $N \sim 500$.

One way to consider the localisation length is by looking for the fraction of the chain over which most of the state probability is contained. In Fig. 3.9 we show the fraction of the whole chain, n/N, over which the steady state probability needs to be summed in order to achieve a total probability of $\mathcal{P}_i^{ss} = 0.95$, as a function of both disorder strength E and the chain length N. Here n is defined as the smallest integer such that

$$\frac{1}{N_d}\sum_d \frac{1}{N_t}\sum_{t_j}\sum_i^n |c_i^{(d)}(t_j)|^2 \geq 0.95, \tag{3.13}$$

with d ranging over $N_d = 100$ disorder realizations, t_j over the $N_t = 100$ discretized time steps from $t = 5t_M$ to $t = 7t_M$.

This calculation shows the Anderson localisation regime, $E > 0.6$ and $N \gtrsim 500$, for the excitation release at $i = 1$, where the chain fraction is close to zero. This means that in this regime most of the state probability is localised close to the initial site. Fig. 3.10 shows how for a fixed strength of disorder, $E = 1$, as the chain gets bigger the 95% of the averaged steady state probability (calculated according to Eq. 3.13) is compressed closer to the initial site, $i = 1$. Such results indicate that, for high amounts of disorder and large chains, the excitation gets localised close to its initial position (i.e. around the first four sites for the case $N = 1000$).

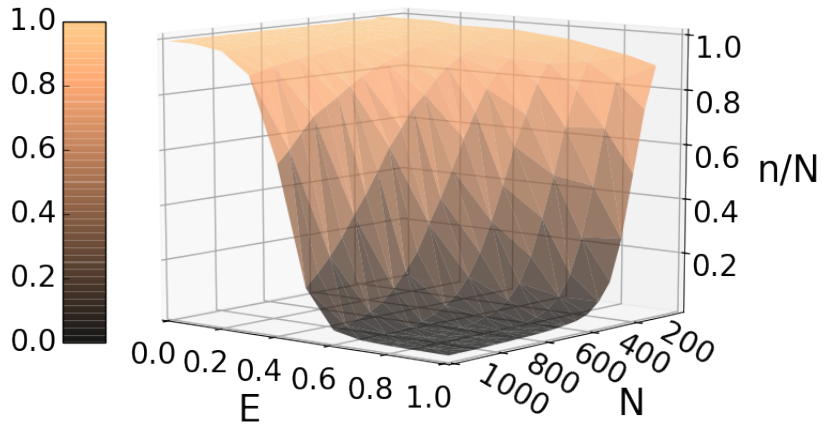

FIGURE 3.9: Ratio n/N against chain length N and perturbation strength E for achieving a total site occupation probability of 0.95, when the excitation is injected at site $i = 1$.

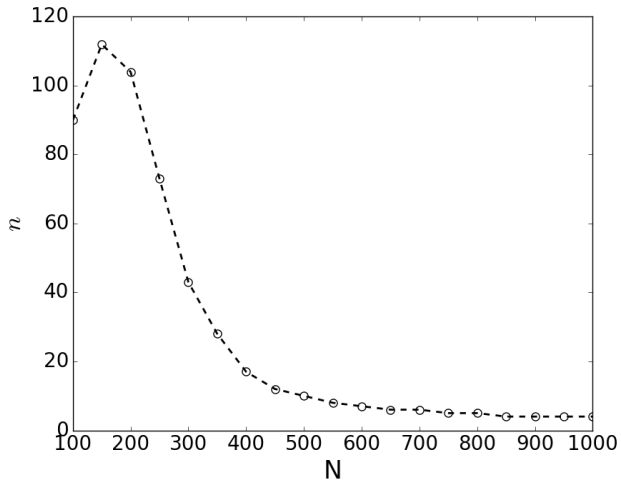

FIGURE 3.10: Number of sites n needed to localise a 95% of the total averaged steady state probability against chain length N for a system initialised at site $i = 1$ and with a disorder strength $E = 1$.

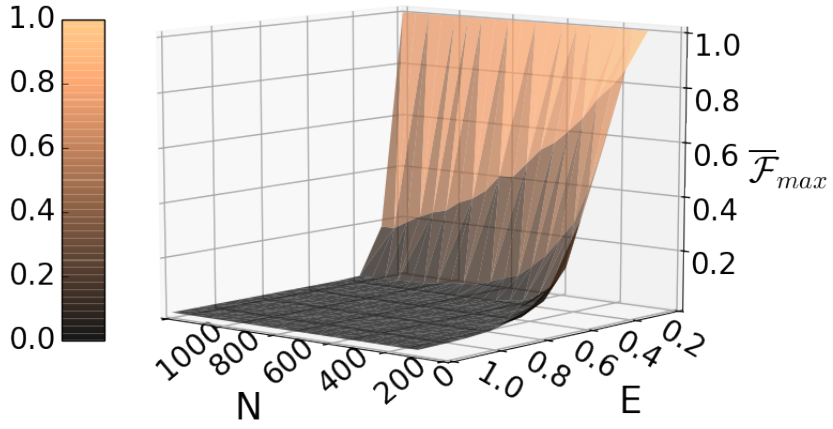

FIGURE 3.11: Maximum fidelity of the transferred state in a window of $4.5t_M$ versus chain length N and perturbation strength E, for excitation released at the chain end site $i = 1$. Results are averaged over 100 disorder realizations.

It is also important to note, that if we change the initial injection site we may obtain different results, even the absence of Anderson localisaton. This is somewhat counterintuitive, as Anderson localisation is normally expected to be independent of initial conditions. However this expectation is correct only when uniform systems are considered, where uniform disorder implies the same local effect on the eigenvalues. When, as in this case, the unperturbed system is non-uniform, uniform disorder may affect *locally* the properties of the system.

3.2.2 Effects on the dynamics

The appearance of Anderson localisation was originally introduced as a way to explain the lack of spin diffusion or electron conductivity in randomly disturbed lattices. Therefore an interesting alternative and complementary perspective from which to consider Anderson localisation effects is to examine transport. The spin system here considered, without any disorder, is by design a "perfect wire" as the chain is enabled to transport an excitation (in analogy of a charge or a spin carrier) from one end to the other with perfect fidelity in a time t_M. Furthermore, modest length N chains with low levels of disorder exhibit potentially useful robustness and the state can still be successfully transferred [64, 73], which is why PST spin chains are considered to be useful elements for short range quantum communication. Nevertheless, for larger N values there is seen to be exponential damping of the transfer fidelity with N, as already sensed from the previous analysis, along with Gaussian dependence on the relevant noise amplitude [64, 73, 143].

Previous work on this topic has looked at the transfer fidelity at some chosen time, which for example would be $t = t_M$ if the objective is perfect quantum communication along a chain. However to link such transport studies to the onset of localisation effects, it is important to examine the fidelity over a range of times to ensure that the maximum transfer fidelity is precisely determined. In fact one contribution to fidelity loss could simply be a shift in the time of an excitation arriving at its destination, rather than a suppression of the arrival happening at all. To demonstrate true localisation and therefore total suppression of PST, we have therefore taken the maximum value of the state transfer fidelity over a significant range of time spanning a number of t_M.

The maximum state transfer fidelity, $\overline{\mathcal{F}}_{max}$, is calculated as an average over 100 disorder realisations of the maximum fidelity of the mirror state (this is a state with an excitation at site $i = N$) in a time window of $4.5t_M$. In Fig. 3.11 we show this $\overline{\mathcal{F}}_{max}$ as a function of both chain length N and disorder strength E, for an excitation released at the chain end site $i = 1$. The PST behaviour is visible for all N at zero disorder $E = 0$, with fidelities close to unity, along with the region of high fidelity for modest N and small E. The presence of such stable range demonstrates the practical application regime of PST spin chains for short range communication. However, for larger amounts of disorder, the figure shows a clear decay and the maximum fidelity approaches zero. Given that the plot is of maximum fidelity over a significant time window, this is therefore evidence for the presence of Anderson localisation, complementary to the results on the spatial distribution of the steady state given in the previous section.

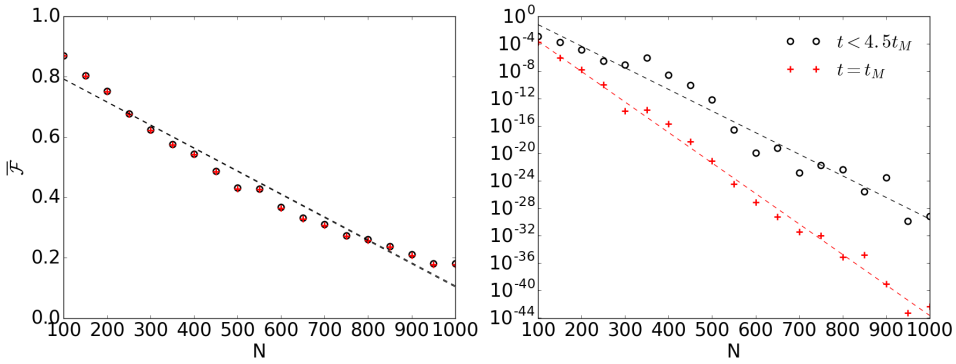

FIGURE 3.12: Averaged fidelity of the transferred state in a time window of $4.5t_M$ versus chain length N, at exactly t_M (red) and maximum value over $4.5t_M$ (black), $E = 0.1$ (left panel) and $E = 1.0$ (right panel). Black and red dashed lines are a fit for all values of N.

More detail on the decay of the fidelity of the state transport is presented in the two panels of Fig. 3.12. The figure presents the averaged transfer fidelity at exact t_M and the maximum transfer fidelity over a time window ($4.5t_M$) for small ($E = 0.1$) and large ($E = 1.0$) levels of disorder. When the disorder is weak (left panel), the maximum transfer fidelity occurs at the expected time of $t = t_M$ and falls off exponentially but slowly with N (left panel), again demonstrating practical and usable

high fidelities for modest $N \sim 100$. For stronger disorder levels (right panel), there is rapid exponential decay of the fidelity, both for the maximum fidelity and for the fidelity at t_M, approaching zero even for moderate length chains. Additionally, for such level of disorder, the maximum fidelity deviates from occurring at t_M. The analysis of the fidelity then demonstrates the strong suppression of PST for a strong levels of disorder and large systems, and supports the appearance of Anderson localisation along with the spatial arguments.

3.2.3 Effects on the eigenstates and energy spectrum

Strong random disorder affects the Hamiltonian spectrum by localising its eigenstates in such a way that localised and extended states will not coexist at the same energy region of the spectrum. Therefore, signatures of Anderson localisation have to be also apparent from the study of the eigenstates and spectrum of spin chains [142]. In order to study how the diagonal random disorder affects the eigenstates, $|\varphi_k\rangle$, of the system we obtain the occupation probabilities as function of the site number i, $\mathcal{P}_{i,k} = |\langle \Phi_i | \varphi_k \rangle|^2$, being Φ_i the basis vectors representing the single excitation subspace (see Section 2.2.2 for further detail). We here restrict ourselves to a strength disorder of $E = 1.0$, for which we already know the state transfer is suppressed and therefore constitutes an optimal value where to observe strong localisation phenomena.

Fig. 3.13 shows the site occupation probabilities of the N eigenstates for a single noise realisation of a $N = 1000$ sites chain. The left (right) inset demonstrates that the eigenstates which peak at the first (last) three sites of the chain are not extended anymore as they are indeed completely localised within very few sites. This is the expected signature of Anderson localisation in one-dimensional systems in which most of the probabilities of the eigenstates of the Hamiltonian are contained over one or few sites. In fact, Anderson theory predicts that for one-dimensional periodic systems under random disorder all the eigenstates will be equally localised. We do not observe this complete localisation because, as already commented, our system is not periodic given the presence of non-uniform interactions between sites. Nevertheless, because our coupling scheme imposes a weaker spin-spin interaction at the ends, the disorder is sufficient to cause strong localisation at the ends but not in the middle. Having said that, we would expect that, eventually, stronger levels of disorder would completely localise the eigenstates peaking in the middle sites of the chain.

We further support the presence of localised eigenstates by considering $\overline{\mathcal{P}}_{i,max}$, the maximum site occupancy probability over all the eigenstates averaged over 1000 realizations. In Fig. 3.14, the maximum averaged site occupation probabilities are shown. The probability of one eigenstate being in the first (last) sites is close to 1. This behaviour is, as expected from previous findings, size dependent and the maximum values increase with the size of the chain (see inset). We contrast this with the corresponding probability distribution for the unperturbed case (pink dashed line

profile): in this case all the states are delocalised along the chain as extended states and hence the maximum probability of occupying any site in the chain is very small and roughly uniform all along the chain. This delocalisation of all eigenstates is crucial for PST (as already seen with the earlier $N = 14$ example of Fig. 3.7): the injection of an initially localised excitation, for example at the end of the chain, is thus injection of a superposition over many eigenstates, giving raise to the well known PST dynamics. When disorder localises the relevant eigenstates at the chain ends, the same initial injection is then a superposition with far fewer significant amplitudes corresponding to more localised eigenstates (eventually just one, for large disorder).

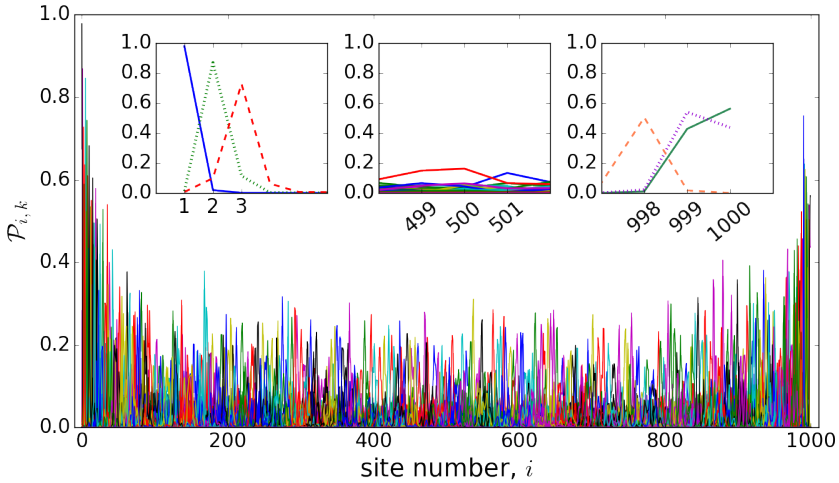

FIGURE 3.13: Site occupation probabilities versus site number i for the N eigenstates of the system for one random realization. Left and right inset show three representative eigenstates which peak on the three initial and final sites of the chain, respectively. Central inset shows the site occupation probabilities of the states peaking in the middle sites of the chain.

The suppression of transport due to Anderson localisation is then explained by combination of eigenstates localisation and splitting of the relevant eigenergies. The upper panels of Fig. 3.15 show the eigenstates localised by disorder on the right contrasted with the delocalised unperturbed states on the left, for the first few sites of the chain. The lower panels show the corresponding energy spectra. For the unperturbed case, the energy levels form a band with an equally spaced distribution of k energy values such that $E_k = (N - 2k + 1)J_0$. However, when random disorder is added such that $E \neq 0$ and we are in the Anderson localisation regime, the perturbed energy levels are no longer uniformly distributed in the band, and gaps begin to appear (see r.h.s lowest panel of Fig. 3.15). Importantly, the energies corresponding to the eigenstates localised on the few first sites are well separated, as shown by the black lines in the lowest r.h.s panel.

The localisation process can be exemplified by comparing the initial state as injected at site 1 for both the unperturbed and perturbed cases shown in the upper panels of Fig. 3.15. At time $t = 0$, the initial state will be a superposition of all the

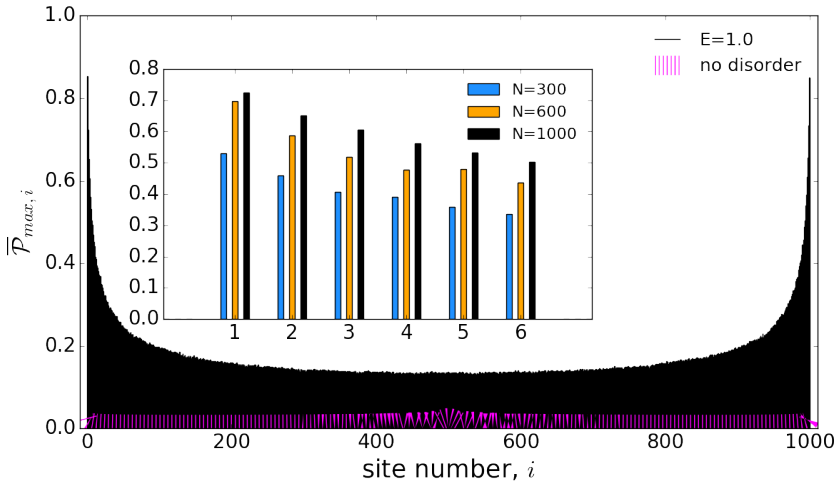

FIGURE 3.14: Averaged maximum occupation probabilities for each site averaged over 100 independent realizations versus site number. The inset shows the difference between the averaged maximum probabilities at the first six sites for N=1000, 600 and 300 (as labeled).

non-vanishing eigenstates at site 1 and its energy will be the corresponding linear combination of eigenenergies. For the unperturbed case, these eigenstates will be many, and by inspection and by considering that the energy band is very dense, we may deduce that the energy from the corresponding linear combination of eigenenergies will not be very different when moving from the first to the next sites (this is in fact corroborated by PST).

However, for the disordered chain, we can approximate the state as injected in site 1 as,

$$|\Psi_{inj}\rangle = c_{11}|\varphi_1\rangle + c_{12}|\varphi_2\rangle + c_{13}|\varphi_3\rangle, \tag{3.14}$$

which will be dominated by approximately one eigenstate, $|\varphi_1\rangle$ (see Fig. 3.15, top r.h.s. panel). Its energy will then be

$$\langle\Psi_{inj}|\mathcal{H}|\Psi_{inj}\rangle = \sum_i \langle\Psi_{inj}|c_{1i}E_i|\varphi_i\rangle,$$

and we can approximate $\langle\Psi_{inj}|\mathcal{H}|\Psi_{inj}\rangle \approx E_1$ as we know that $|a_{11}|^2 \gg |a_{12}|^2, |a_{13}|^2$ (see upper r.h.s panel of Fig. 3.15).

Bearing in mind that the dynamical evolution of our Hamiltonian will conserve the energy, and having shown that our initial state sits on the E_1 energy level, we can conclude in addition to the eigenstate localisation argument that, because the eigenstates peaking at the nearby sites have energies far apart from the initial one (see Fig. 3.15, bottom-right panel), the state transfer will be strongly diminished. Therefore localisation for this specific case is indeed supported by both eigenstate and eigenenergy arguments and the no coexistence of localised states with extended ones: spatially close overlapping eigenstates have distant eigenenergies, states with

close energy levels have spatially distant eigenstates with vanishing overlap.

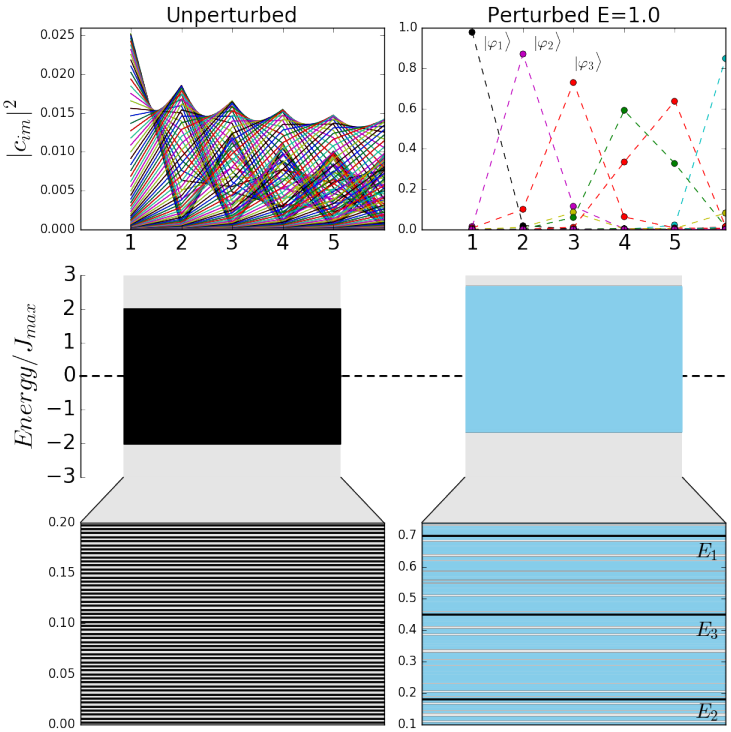

FIGURE 3.15: Site occupation probabilities of the eigenstates peaking at the first few sites of an unperturbed (l.h.s) and perturbed $N = 1000$ chain with $E = 1.0$ (r.h.s) (top panels) and their energy spectra (other panels). Both bottom panels display a zoom to clearly observe the energy splitting, equally spaced for the unperturbed chain and randomly spaced (white gaps) for the perturbed chain. The black lines in the bottom r.h.s. panel indicate the eigenergies corresponding to the eigenstates $|\varphi_1\rangle, |\varphi_2\rangle, |\varphi_3\rangle$ in the top r.h.s. panel.

3.3 Summary

In this chapter we have explored the ability of spin systems, mainly one-dimensional spin chains, to transfer quantum states. This behaviour has made this system very popular due to its potential applications to communicate quantum information over small distances, e.g. between registers of a quantum processor, as an alternative to photonics. The transport phenomenon can be triggered in several ways, but here we considered the engineering of the chain interactions. Under ideal conditions, such scheme leads to the quantum transport with perfect fidelities (PST). Previous investigations on the robustness of the transfer of quantum states over spin chains have showed that they present a level of robustness in their transport properties, which is why they are of interest for quantum information transport.

In that line, we have investigated in detail the phenomenon of localisation in one-dimensional PST spin chains in the moderate-strong disorder regime. Our investigations show that transport is affected by moderate disorder and suppressed

for levels of disorder of the order of $E \sim 1$ and for growing chain lengths N, due to the spatial localisation of a locally injected excitation. One excitation injected at the chain end exhibits genuine Anderson localisation for this level of disorder and chains longer than $N \sim 500$. These localisation signatures are also reflected in the system eigenstates, with eigenstates localised over few sites at the beginning and end of the chain for $N \gtrsim 500$ and $E \sim 1$. These localised states have energies that sit far apart in the energy spectrum, as well as vanishing overlap with closer states, further supporting the lack of hopping between stated sites.

On one hand, we have seen how the exhibition of localisation phenomena due to random disorder can indeed damage the desired result of the operation for which a spin chain device is set. In this case, the operation desired was related to state transport, but it could be any other, and the existence of methods to protect such operations from disorder would be very useful. On the other hand, the presence of localised eigenstates could be something to take advantage of. The utilisation of such states could lead us to the possibility of using spin chains for quantum state localisation purposes and therefore memories. Let us now move to the next chapter and explore all these questions.

Chapter 4

Spin chains for protected quantum state localisation

In this chapter we consider spin chain families inspired by the Su, Schrieffer and Hegger (SSH) model. The presence, nature and robustness of topologically protected localised eigenstates is investigated in detail. The potential use of such systems for storing quantum states and serving as quantum memories is also examined. Part of this work has been published in: **M. P. Estarellas, I. D'Amico & T.P. Spiller**, "Topologically protected localised states in spin chains", Scientific Reports **7**, 42904, (2017).

In the previous chapter we have focused on systems designed to serve as quantum wires, that is, designed to allow for perfect or high fidelity state transfer and distribute a quantum state from its initial position to a desired location. However, now we want to consider a different application also crucial in the exploitation of quantum technologies. While spin chain models, as we have already explored, have been identified as promising candidates for short-range quantum communication, any implementation of a quantum computer will also need to have a means to store quantum information. Classical computers use silicon-based memories to save their digital bits temporarily (volatile memories such random-access memories or RAM) or permanently (non-volatile memories such the read-only memories or ROM). Yet a quantum counterpart of such devices, even in its most primitive form such as in gate processed circuits, will have to face an additional hurdle: decoherence, which can have a considerable impact in the quantum properties of the system as we have previously seen. For this reason, proposals to build the first quantum state memories (and other applications) pay special attention to the protection of the coherence of the stored quantum state against external disorders and possible small deformations during the fabrication process of the device. This context of finding a way to create a dissipation-free zone for the manipulation of qubits, is where the idea of topological quantum computers appeared [39, 165, 166].

Topology has acquired an increasing importance in condensed matter physics since the observation of the Quantum Hall effect [167] and the first experimental realization of a topological insulator [168]. One of the most sought applications of the

topological state confinement is its use to design coherence protected quantum transistors [169]. Such systems can embody quantum information as topologically protected states and they open new paths in the search for a robust quantum processing architecture.
In this chapter we apply the well known Su, Schrieffer and Hegger (SSH) model [170], one of the simplest models showing non-trivial topological effects for one-dimensional systems, to linear spin chains. We explicitly demonstrate the presence of such effects through the confinement of an eigenstate and the opening of a gap in the energy spectrum. We extend this idea to a set of related chain configurations with different coupling patterns and number of confined states present. These configurations display one or more localised eigenstates with most of their state probability confined in one site of the chain. The localisation is such that it opens the possibility of injecting or initialising a qubit state locally and keep the information encoded in such a state at that individual site. The robustness of the localised state is investigated by simulating static random disorder, showing that these protected states are very robust against this type of perturbations. Systems with such resilience against fabrication defects or quasi static fields are of clear interest for quantum information tasks and their ability to perform potential memory applications is discussed in this chapter.

4.1 SSH model

The Su, Schrieffer and Hegger (SSH) model was first presented in 1979, to describe a soliton formation in polyacetylene, $(CH)_x$, and allow the understanding of its conduction mechanism [170]. This polymer has a dimerised chain pattern constructed by the alternating single and double bonds as result of the sp^2 hybridization of the carbon atoms. This is a consequence of the Peierls instability [171] (also called the Jahn Teller effect), the distortion of a uniform lattice that lifts the degeneracy of the two states in the Brillouin zone opening an energy gap in the spectrum. The system's ground state is therefore a superposition between two isoenergetic configurations corresponding to the two resonant forms of the molecule, which are equivalent under interchange of single with double bonds alternatively, as shown schematically in Fig. 4.1.

These two configurations (α and β from Fig. 4.1) coexist through the dynamics of a charge carrier, also called soliton, which appears as an electronic zero-energy mode in the middle of the band gap. It is in this situation where the symmetry of the system is broken and this soliton creates a domain wall between the two configurations. Under chemical doping, more of these solitons appear and the conductivity of the polymer increases [172]. This phenomenon drove the scientific community to the further study of conducting polymers culminating in the form of a Nobel Prize in Chemistry for Heeger, MacDiarmid and Shirakawa in 2000 [173–175].

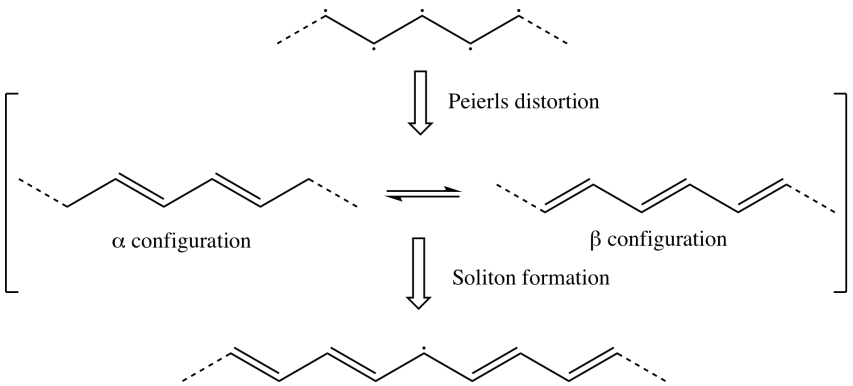

FIGURE 4.1: Schematic diagram of the process that leads to a soliton formation in polyacetylene driven by the dimerisation of the lattice caused by the Peierls instability.

The domain wall that appears between the two configurations is a protected eigenstate at zero energy also called a zero mode. Jackiw, Rebbi and Schrieffer explained the presence of this mode through field theory [176, 177], while more modern literature makes use of the topology argument [111, 178–181]. We will here focus on the latter.

4.1.1 Topological characterisation

Topology studies whether objects can be transformed into each other continuously [182]. In condensed matter physics we can ask whether the Hamiltonians of two quantum systems can be continuously transformed into each other. If that is the case, then we can say that those two systems are topologically 'equivalent'. If we consider all Hamiltonians without any constraint, every Hamiltonian could be continuously deformed into every other Hamiltonian of the same size, and all quantum systems would be topologically equivalent. This, however, changes drastically if we restrict ourselves to systems with a conserved topological invariant [183], e.g. the presence of an energy gap. If an energy gap is present, then the Hamiltonian of the system has no eigenvalues in a finite interval and there is a finite energy cost to excite the system above this gap. So our constraint or invariant would be to preserve the gap over the Hamiltonian finite transformation. In this example, then we say that two gapped quantum systems are topologically equivalent if their Hamiltonians can be continuously deformed into each other without ever closing the energy gap.

Discrete symmetries can have a rich influence on topology (time-reversal symmetry, particle-hole symmetry,...) and in the SSH model we explicitly encounter chiral (also named sublattice) symmetry. Systems with such symmetry are characterised by the possibility of dividing the degrees of freedom into different groups, something that happens when the lattice has two sublattices (A and B):

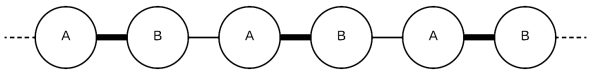

FIGURE 4.2: Diagram showing the sublattices A and B joined by weak (thin line) and strong (thick line) couplings.

As a consequence, the Hamiltonian of this system can be reduced to,

$$H = \begin{pmatrix} 0 & H_{AB} \\ H_{AB}^{\dagger} & 0 \end{pmatrix} \tag{4.1}$$

and the sublattice symmetry arises from the following operation,

$$\sigma_z H \sigma_z = -H \tag{4.2}$$

This immediately reveals that if $(\Psi_A, \Psi_B)^T$ is an eigenvector of the Hamiltonian with energy ε, then $(\Psi_A, -\Psi_B)^T$ is also an eigenvector with energy $-\varepsilon$. The consequence of this symmetry is therefore a symmetric spectrum.

Interesting topological phenomena arise when connecting two regions with topologically distinct regions [111, 184, 185]. In a dimerised system such as the SSH model, we can understand the soliton as an interface between two topologically distinct dimers configurations or domain wall, e.g. the α and β configurations shown in Fig. 4.1. Additionally, we could also think of a defect acting as a domain wall at the edge of a chain as an interface between the dimerised system and the vacuum. This means that a topological transition at the soliton or defect site must exist and that a localised state will be present. Both case scenarios will be explored here by studying two different dimerised chain configurations.

Widely used topological invariants in one dimensional systems such as the winding number [183] or the Zak phase [186, 187] are useful quantities to identify topologically distinct configurations. These can be applied to the SSH model in order to characterise each of the dimer configurations and demonstrate the topological nature of the domain wall or 'soliton' between them. See [188] for more detail on the topological properties of the SSH model.

4.1.2 Application to Spin Chains

As already pointed out, there are potential advantages of building protected quantum regions, and the possibility of constructing spin chains to be topologically analogous to the SSH model makes them a good system in which to study this type of localisation and protection phenomena. We here translate the polyacetylene picture into the spin chain formalism. Previous works have already done the same extrapolation to different experimental set-ups such as edges of graphene ribbons [189], edges of honeycomb arrays of microcavity pillars [190], optical waveguides [110] or Bose-Einstein condensates of Rb^{87} atoms in suitable optical lattice potentials [179,

187], motivating the further theoretical exploration of these models. We simulate the dimerisation caused by the Peierls instability in polyacetylene by modulating the inter-site coupling or interactions of a one-dimensional finite spin chain. Here we consider symmetric chains with an odd number of spins or sites with alternating weak (δ) and strong (Δ) couplings. Each chain is symmetric with respect to the mid point, here labeled as site $i = 0$. We consider two different chain configurations (sketched in Fig. 4.3), configuration (a) and (b), and the coupling nature of site 0 will determine the rest of the chain. As seen in the previous section, the soliton is the domain wall between the two distinct configurations of the ground state in polyacetylene. This is here mimicked as a defect weakly coupled to the rest of the system at site $i = 0$ in configuration (a). On the other hand, the inverted scenario is also examined in configuration (b), flipping the inter spin couplings, and leaving two edge defects, which still create a domain wall between two different configurations.

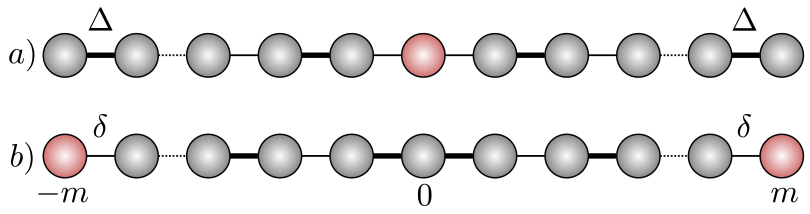

FIGURE 4.3: Spin chain configurations (a) and (b).

The time independent Hamiltonian of an N-site spin chain of this form can be written as (see Section 2.1.1 for further detail),

$$\mathcal{H} = \sum_{i=-m}^{m} \epsilon_i |1\rangle\langle 1|_i + \sum_{i=-m}^{m} J_{i,i+1}[|1\rangle\langle 0|_i \otimes |0\rangle\langle 1|_{i+1} + |0\rangle\langle 1|_i \otimes |1\rangle\langle 0|_{i+1}], \quad (4.3)$$

where $m = (N-1)/2$. $J_{i,i+1}$ are the coupling strengths between two nearest-neighbour sites and are pre-engineered to take two different values, Δ and δ. As an example. in the calculations presented here and unless stated otherwise, we choose a ratio between the couplings of $\delta/\Delta = 0.025$, with a chain length of $N = 101$. Therefore, for the first case (Fig. 4.3-a), site 0 is weakly coupled ($J_{-1,0} = J_{0,1} = \delta$) to the rest of the chain such that,

$$i \in 2\mathbb{Z} \begin{cases} J_{i,i+1} \equiv \delta, & J_{i+1,i+2} \equiv \Delta \quad (0 \leq i < m) \\ J_{i,i+1} \equiv \Delta, & J_{i+1,i+2} \equiv \delta \quad (-m \leq i < 0) \end{cases} \quad (4.4)$$

In the second case (Fig. 4.3-b), site 0 is strongly coupled to the rest of the chain, $J_{-1,0} = J_{0,1} = \Delta$,

$$i \in 2\mathbb{Z} \begin{cases} J_{i,i+1} \equiv \Delta, & J_{i+1,i+2} \equiv \delta \quad (0 \leq i < m) \\ J_{i,i+1} \equiv \delta, & J_{i+1,i+2} \equiv \Delta \quad (-m \leq i < 0) \end{cases} \quad (4.5)$$

4.2 Characterisation of the localised state(s)

In order to study and characterise the localisation features of our system, the eigenstates and their relative eigenvalues need to be obtained. This is done through diagonalization of the Hamiltonian defined in Eq. 4.3 for both chain configurations shown in Fig. 4.3 (see Chapter 2 for more detail). As expected in analogy with the results previously obtained for other SSH-like models, a localised state at the central site is found for the spin chain configuration (a) and two localised states at the edges are found for the spin chain configuration (b). We characterise the nature of such states not only from the static point of view, but also dynamically. This is attained from evolving the system when an excitation is initially injected at those localised states. In this section we demonstrate state localisation supported by the eigenstates, energy spectrum and dynamics of the system.

4.2.1 Eigenstates and energy spectrum

Let us first focus on the single-excitation eigenstates and the band structures of these two types of chain. The study of the eigenstates of the system, $|\varphi_n\rangle$ with $n \in [1, N]$, immediately shows localisation signatures for both types and such features will be discussed separately.

Spin chain configuration (a):

By looking at the eigenstates' probabilities we observe a confined state sitting in the middle of the chain. Fig. 4.4 shows the absolute squared amplitudes, hence the occupation probabilities, as a function of site number i, $\mathcal{P}_{i,n} = |\langle i|\varphi_n\rangle|^2$, for each eigenstate.

The localised state sits at site $i = 0$ as predicted and seen from the green profile of Fig. 4.4 that peaks up to ~ 1. This means that almost the entire occupation probability of that eigenstate is contained at that site, hence it is localised. The rest of the eigenstates, as observed in the figure and with some enlarged areas presented in the insets for more clarity, are spread along the chain and therefore completely delocalised.

The presence of a confined eigenstate is however not enough to ensure that the state will remain localised and protected, and the inspection of the full energy spectrum is needed. In Fig. 4.5 the spectrum of this configuration clearly shows the presence of an energy gap. In the middle of the gap and between twenty-five higher and twenty-five lower twofold degenerate states, there is one zero-energy state corresponding to the eigenstate confined at site $i = 0$. This observation is crucial as it is the presence of the gap that protects the state.

With the use of symmetry arguments and by simplifying the chain in smaller sections of dimers we can accurately explain the features of the spectrum. Due to the chiral symmetry of the chain configuration, an operator $\mathcal{M}$ reflects the system

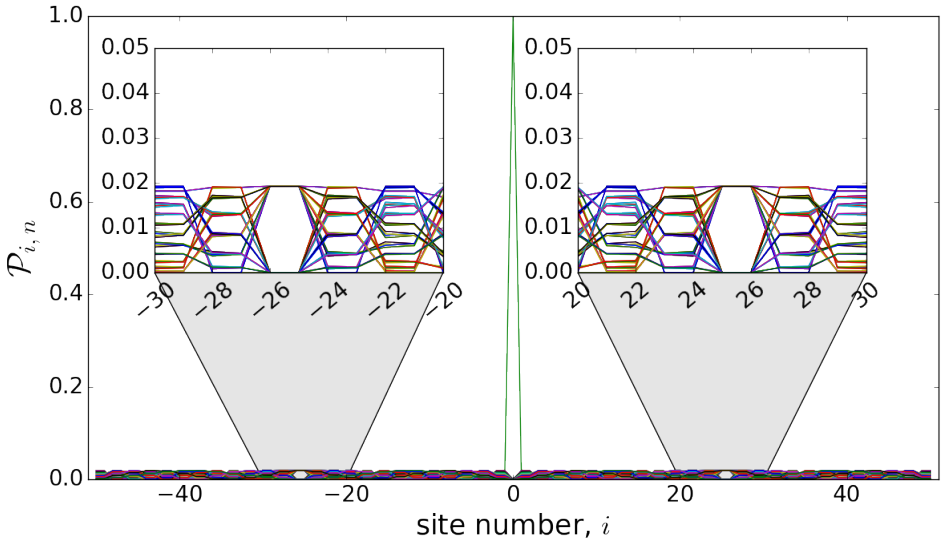

FIGURE 4.4: Eigenstate occupation probabilities, $\mathcal{P}_{i,n}$, versus site number i for a $N = 101$ sites spin chain under (a) configuration. The localised state peaks at ~ 1, sits at site $i = 0$ and it is shown in green. The rest of eigenstates are delocalised over the chain and the two insets show two different enlarged sections with such states

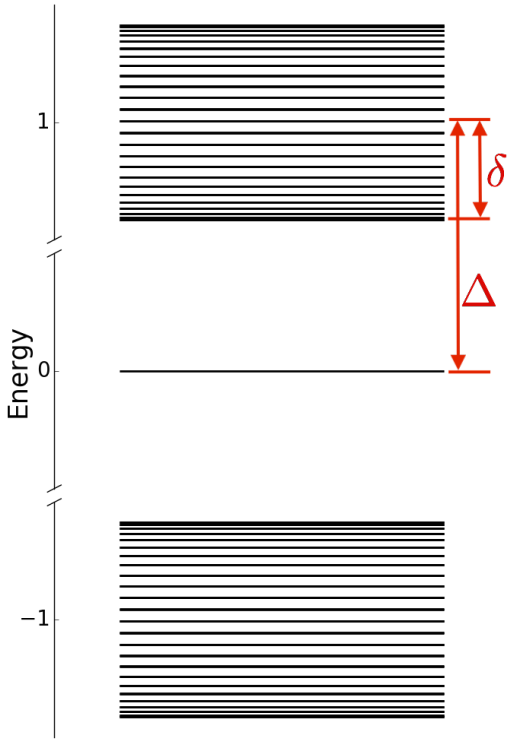

FIGURE 4.5: Energy spectrum of $N = 101$ sites spin chain with configuration (a). Each of the states in the bands are two-fold degenerate and one single localised state sits in the middle.

about its middle site ($i = 0$). Such an operator commutes with the Hamiltonian and therefore non-degenerate eigenstates of the system must each be even or odd (with eigenvalue $+1$ or -1) under $\mathcal{M}$. On the other hand, given that $\Delta \gg \delta$, each the pair

of strongly (Δ) coupled sites can be seen as a dimer. Each dimer formed by sites $|i\rangle$ and $|i+1\rangle$ has the eigenstates $\frac{1}{\sqrt{2}}(|i\rangle \pm |i+1\rangle)$ with eigenvalues $\pm\Delta$. Using these dimer states (rather than the site states) as basis states we can explain the positions of the energy bands in Fig. 4.5. The mid points of these bands are at the dimer energies $\pm\Delta$ and we have $m/2$ weakly coupled dimers either side of the central site state $|i=0\rangle$. Using these dimer states as a basis, the higher energy ($+\Delta$) dimer states for positive i ($0 < i \leq m$) can be treated as an $m/2$-site weakly coupled uniform spin chain with a constant coupling of $\delta/2$. This can be confirmed by comparing each of the bands with the analytical formula for the energy spectrum of a uniform spin chain $E_n = \delta(1-\cos(\frac{\pi}{m/2}(n-1)))$ [120], being $n = 1, 2, .., m/2$ and J the uniform coupling. From this we can assert that the eigenstates are delocalised superpositions of the dimer states with eigenvalues forming a band that spreads from $\Delta-\delta$ to $\Delta+\delta$, with a characteristic cosine distribution within the band, as observed in each bands of Fig. 4.5. The higher energy ($+\Delta$) dimer states for negative i ($-m \leq i < 0$) can be treated analogously, with eigenvalues degenerate with the positive i states. Enforcing the symmetry under reflection $\mathcal{M}$ means that the final upper band eigenstates for this configuration are even or odd superpositions of the positive and negative i band states. These odd and even states are degenerate, which explains why each band level, as shown in Fig. 4.5, is doubly degenerate. A similar analysis follows for the positive and negative i lower energy ($-\Delta$) dimer states, giving a band of doubly degenerate states ranging from $-\Delta-\delta$ to $-\Delta+\delta$, with the same characteristic cosine distribution. The full set of $2m+1$ eigenstates and eigenvalues for this type of chain is completed with the inclusion of the localised state $|i=0\rangle$ that has zero energy.

Spin chain configuration (b):

The previous picture gets more complicated when considering the eigenstate and energy spectrum of the configuration (b). In Fig. 4.6, the eigenstates occupation probabilities are again displayed and two states with probabilities ~ 1 are found confined at the edges of the chain. Additionally and in contrast with the previous case scenario, we now observe three localised eigenstates peaking at ~ 0.5 in the three middle sites of the chain ($i=-1$, $i=0$ and $i=1$). From these, two of them peak at the central site while the other one peaks at its neighbouring sites. The remaining eigenstates are still delocalised along the chain (see insets of Fig. 4.6).

The energy spectrum now displays three degenerate zero-energy eigenstates in the middle of the gap, corresponding to the ones peaking at the edges and neighbour sites of the central site of the chain (see Fig. 4.7). These states are surrounded by twenty-four higher/lower twofold degenerate states and one highest/lowest state forming two other bands against the bulk of states. The latter two states occur at energies $\pm 2\sqrt{\Delta}$ and correspond to the two additional states peaking in the chain centre in Fig. 4.6.

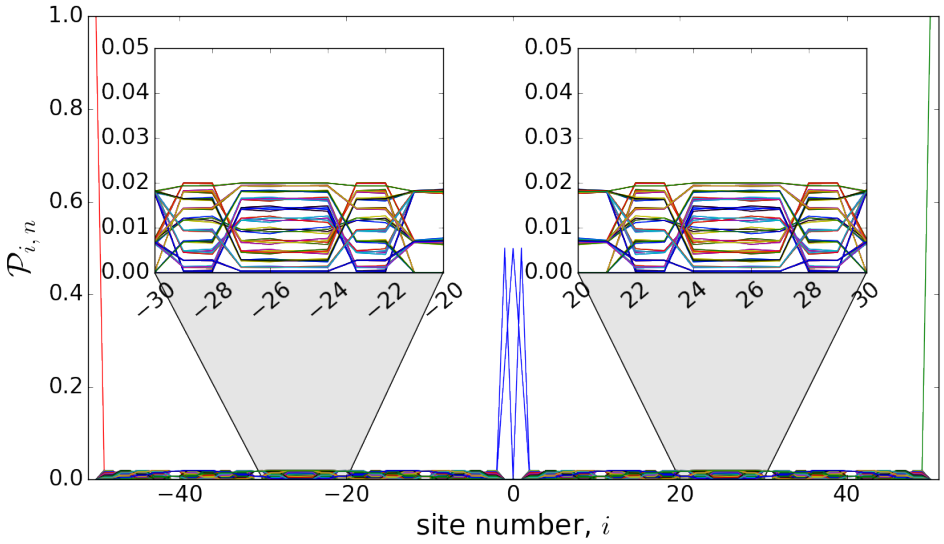

FIGURE 4.6: Eigenstate occupation probabilities, $\mathcal{P}_{i,n}$, versus site number i for a $N = 101$ sites spin chain under (b) configuration. Two localised states peak at the edges of the chain ~ 1 and are shown in red and green. Three eigenstates peak at ~ 0.5 at the three central sites of the chain and are shown in blue. The rest of eigenstates are delocalised over the chain and the two insets show two different enlarged sections with such states.

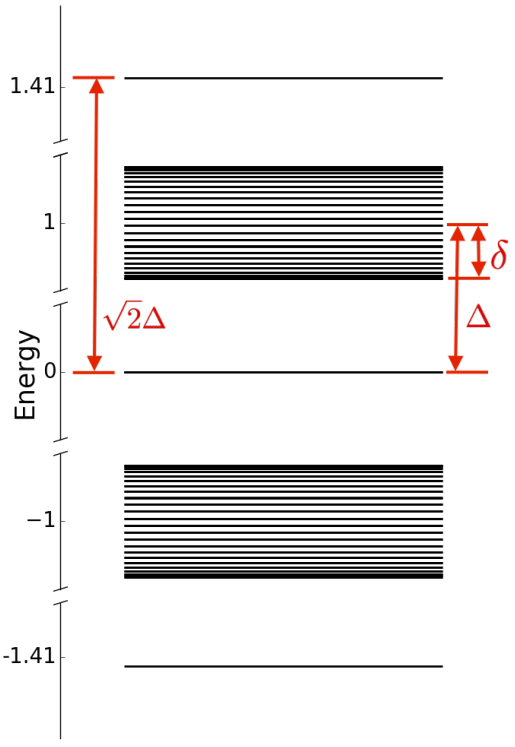

FIGURE 4.7: Energy spectrum of $N = 101$ sites spin chain with configuration (b). Each of the states in the bands are two-fold degenerate and a further state sits above/below the upper/lower band. Three degenerate states sit at zero energy.

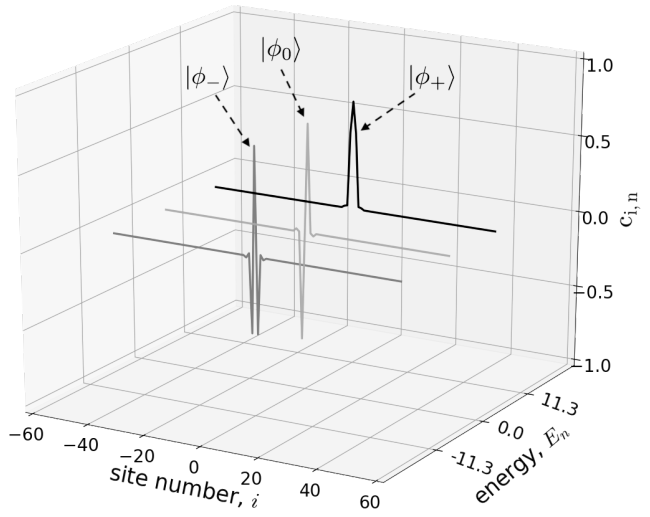

FIGURE 4.8: State amplitudes versus site number, i, and energy, E_n, for the three states corresponding to the ones whose probabilities are in the center of the chain with configuration (b) and its neighbouring sites (trimer subsystem). Their energies correspond to the ones sitting above/below the upper/lower bands of the spectrum spin chain and to one of the zero-energy states sitting in the gap. The structures of these states are equivalent to the ones in Eq. 4.6.

Again, symmetry and dimerisation arguments help us understand the spectra and eigenstates of this configuration. Let us now simplify the structure of configuration (b) by partitioning the system. In this case we have the end sites ($|-m\rangle$ and $|m\rangle$) weakly coupled (δ) to two subsystems of $(m-2)/2$ dimers. In turn, these two subsystems are weakly coupled to a trimer; this a strongly coupled (Δ) subsystem of three sites corresponding to $|-1\rangle$, $|0\rangle$ and $|+1\rangle$ sitting in the middle. We focus first on the trimer and given that $\delta \ll \Delta$ we can approximate its eigenstates to the ones obtained from an isolated trimer. The eigenstates of a trimer are then given by Eq. 4.6, with $|\phi_-\rangle$ having energy $-\sqrt{2}\Delta$, $|\phi_0\rangle$ having energy zero and $|\phi_+\rangle$ having energy $\sqrt{2}\Delta$.

$$|\phi_-\rangle = \begin{pmatrix} -1/2 \\ 1/\sqrt{2} \\ -1/2 \end{pmatrix} |\phi_0\rangle = \begin{pmatrix} -1/\sqrt{2} \\ 0 \\ 1/\sqrt{2} \end{pmatrix} |\phi_+\rangle = \begin{pmatrix} 1/2 \\ 1/\sqrt{2} \\ 1/2 \end{pmatrix} \tag{4.6}$$

We can relate the structure of such trimer states to the three semi-localised states that sit in the middle, the amplitudes of which are shown in Fig. 4.8. The trimer state $|\phi_+\rangle$ corresponds to the one sitting above the upper band of Fig. 4.7, the trimer state $|\phi_-\rangle$, to the one below the lower band, and the third trimer state $|\phi_0\rangle$ to the one in the mid-gap at zero-energy. Adding the later to the other two edge states $|-m\rangle$ and $|m\rangle$ we obtain the triply degenerate level at zero energy between the bands. The band levels themselves are again even or odd superpositions of the positive and negative

i band states (as for configuration (a)) with the same cosine distribution except that here each band contains $(m-2)$ levels (instead of m). The total level count is thus still $2m+1$.

4.2.2 State Dynamics

In addition to the static argument, we also wish to explore the behaviour of the localised states with time. To do so the evolution of the initial state $|\Psi(0)\rangle = |1\rangle_k \otimes |0\rangle_{rest-of-chain}$ with injection at the central site $k=0$ for configuration (a) and edge site $k=-m$ for configuration (b) has been studied.

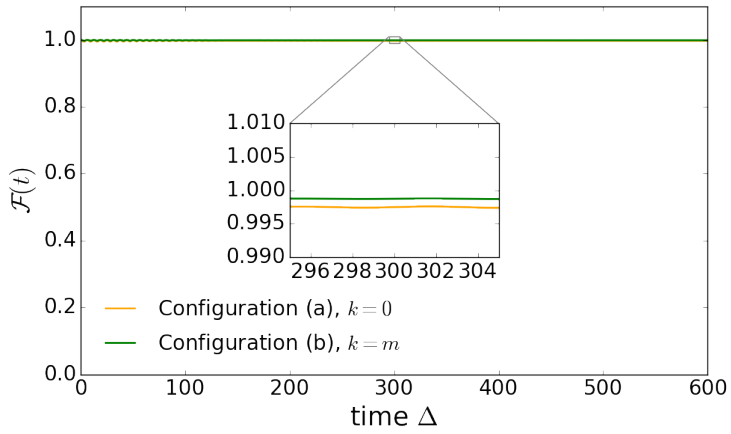

FIGURE 4.9: Fidelity of the initial state $|\Psi(0)\rangle = |1\rangle_k \otimes |0\rangle_{rest-of-chain}$ at the central site ($k=0$) for configuration (a) and edge site ($k=-m$) for configuration (b). The inset is a blow-up of a section at $time \sim 300$.

More arguments supporting localisation are obtained from the observation of Fig. 4.9. The fidelities ($\mathcal{F}(t) = |\langle\Psi(0)|\Psi(t)\rangle|^2$) of the states injected at the sites that present confined eigenstates remain almost constant and very close to unity (presented as an inset in the center of the figure). This implies that most of the probability of the initial state remains contained on the localised eigenstate and its evolution will not give significant non-zero probability components at any other site.

4.3 Ratio and length dependence

As shown in [111], the topological distinctiveness of the two α and β phases (or the vacuum) leads to the formation of an exponentially localised state with a wavefunction of the approximated form $|\psi_i\rangle = (-\Delta/\delta)^{-|i|/2}$ for even sites and $|\psi_i\rangle = 0$ for odd sites i. All the previous analysis has been done considering a pretty low coupling ratio value, $\delta/\Delta = 0.025$. This means that, given that $\Delta \gg \delta$, the dimerisation of the system is very marked. With such a coupling ratio, the exponential decay of the localised amplitudes is such that our states are indeed highly localised and non-overlapping. However, the localisation features seen along the previous section are still significant for coupling ratios an order of magnitude bigger and the exponential

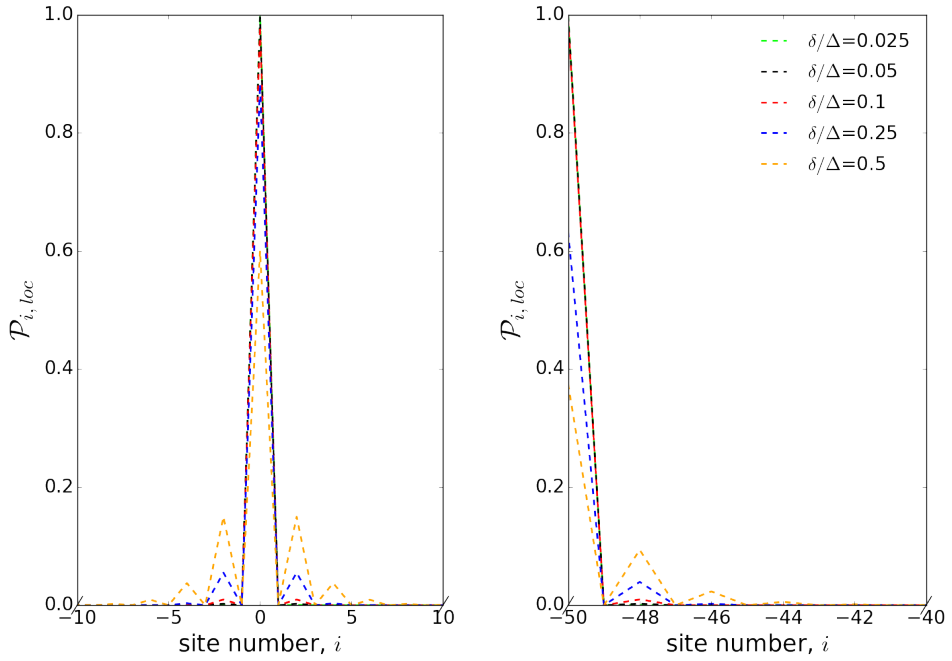

FIGURE 4.10: Change on the structure of the probability peak, $\mathcal{P}_{i,loc}$, of the localised state at site $i = 0$ for configuration (a) –left panel– and $i = -m$ for configuration (b) –right panel– with coupling ratio δ/Δ.

decay of the localised state state confined to the sites with even index is more visible. This is presented in the two panels of Fig. 4.10 where it can be observed that the occupation probability, $\mathcal{P}_{i,loc}$, on the relevant sites $i = 0$ and $i = -m$ for configurations (a) and (b), respectively, does not start decreasing from $\mathcal{P}_{i,loc} \sim 1$ until the coupling ratio is $\delta/\Delta = 0.25$. In such case, the occupation probability is of the order of 0.6 for configuration (a) and 0.88 for configuration (b). For higher ratios the probability profile of the localised state of configuration (b) has a more pronounced exponential decay for even sites of the chain, as observed for the profile $\delta/\Delta = 0.5$, and its tails end up overlapping with the localised state that sits at the other edge of the chain. Such behavior can also be understood from the influence of Δ and δ to the spectrum structure (see Fig. 4.5). If the coupling ratio increases by increasing δ, the eigenstates in the energy bands spread between higher limits as, in absolute values, they go from $\Delta + \delta$ to $\Delta - \delta$. This affects the protection of the localised states as with the increase of δ (or the decrease of Δ) the gap becomes smaller and vanishes when $\delta/\Delta \to 1$.

We can therefore assert that there is scope for flexibility in the tuning of the coupling ratio. Moderate coupling ratios still allow for significant localisation patterns as long as the energy gap is conserved. The scalability of the system, on the other hand, will depend on the type of configuration. In the case of configuration (a), the chain can be enlarged as much as desired by adding dimers at either sides of the central $i = 0$ site. The localised state will still be present with a probability dependent only on the chosen coupling ratio. If we want, on the contrary, to reduce the

length of the chain, the shortest length allowed for this chain type will be $N = 5$ in order to preserve the symmetry of the spectrum (the central weakly coupled site and two strongly coupled dimers at each side). In the case of configuration (b) there is more than one localised eigenstate present. Such states sit at the ends of the chain and therefore if the system is too short the tails of the two localised eigenstates will unavoidably overlap (similarly to what happens when the coupling ratio is high). Through investigation of a range of systems, the limit found for $\delta/\Delta = 0.025$ coupling to start happening is $N < 45$. In Fig. 4.11 the eigenstate occupation probabilities of a $N = 21$ sites chain are shown in order to illustrate this. For such a scenario, the two eigenstates that were localised at each edge site of the chain for large N are now overlapped and peaking up to ~ 0.5 in probability simultaneously at both sides, so we lose the localisation property. However, due to the superposed nature of the two eigenstates (symmetric and antisymmetric) any state initially injected at one of the edge sites of the chain transfers to its opposite (mirror) site at the other edge and we therefore foresee the application of such system for quantum state transfer purposes.

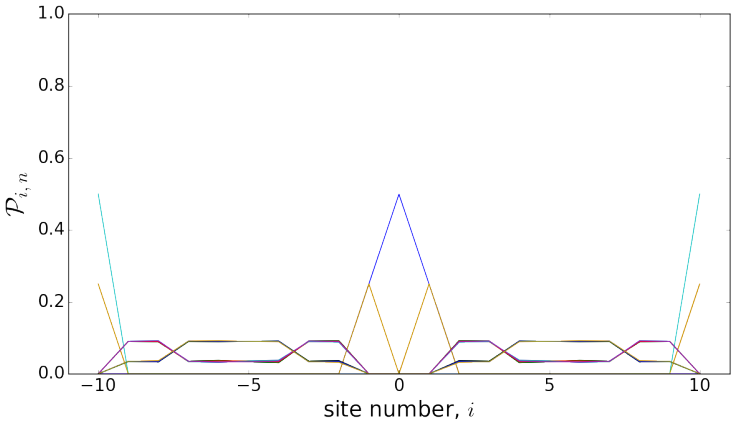

FIGURE 4.11: Eigenstate occupation probabilities, $\mathcal{P}_{i,n}$, versus site number i for a $N = 21$ sites spin chain under (b) configuration. The localised state peaks at ~ 1, sits at site $i = 0$ and it is shown in green. The rest of eigenstates are delocalised over the chain. The rest of eigenstates are delocalised over the chain and the two insets show two different enlarged sections with such states

From the above observations we can justify our decision of studying the example of N=101 and $\delta/\Delta = 0.025$, which is well into a region where the localised states are both N and δ/Δ independent. We however remark that this is not the extreme limit where to observe localisation and protection phenomena and other chain lengths and coupling ratios can indeed be considered.

4.4 Robustness and Protection

The previous discussion of the bands and eigenstates explains how the energy gap is created. The choice of a small coupling ratio (in our case we are taking $\delta/\Delta = 0.025$)

leads to gaps between the localised states and the bands of order Δ. This gap protects the structure of the state as the energy needed for a perturbation to excite the state up to the next level is, also, of the order of $\sim \Delta$. If the coupling ratio is lowered then the spread of the bands increases, relative to the separations between the localised states, reducing the effect of the energy gap protection.

This protection is crucial because any implementation of a quantum state memory, no matter how small, will need to show at least –and assuming the role of a volatile memory only, hence temporary– some level of robustness against external disorder, i.e. without losing its coherence. In this section we will investigate this in detail by imposing on the system two different types of disorder and then inspecting the impact these have on the spectrum.

4.4.1 Diagonal disorder

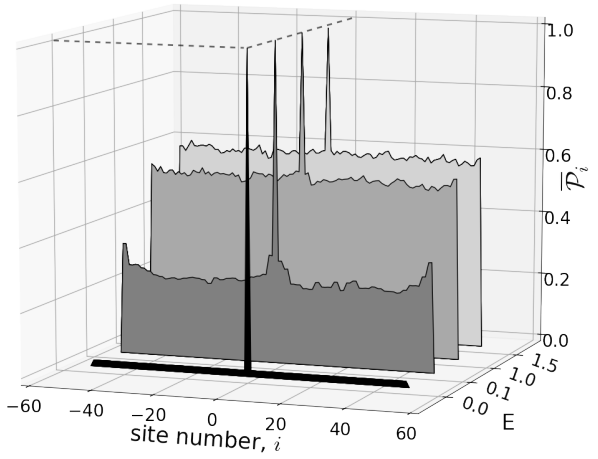

FIGURE 4.12: Maximum occupation probabilities for each site of configuration (a), averaged over 100 independent noise realisations, with $E = 0.0$ (black), $E = 0.1$ (darkgrey), $E = 1.0$ (grey) and $E = 1.5$ (light gray) levels of diagonal disorder. The y-axis representing the scale of the disorder E has some band gap regions omitted for clarity.

We have already mentioned that one approach to modelling disorder is to add random diagonal disorder to the Hamiltonian (see Chapter 2). The dimensionless parameter E that sets the scale of the disorder is weighted against Δ. Due to the stochastic nature of these calculations, we average the maximum site occupancy probability for all the N eigenstates over 100 realisations of the disorder (average denoted by a bar),

$$\bar{\mathcal{P}}_i \equiv \overline{\max_n |\langle i|\varphi_n\rangle|^2}. \tag{4.7}$$

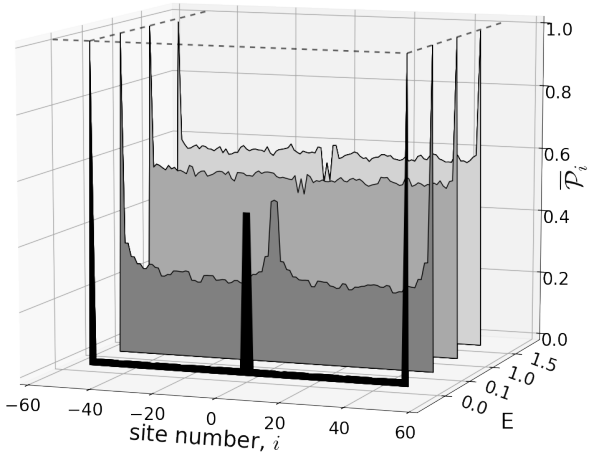

FIGURE 4.13: Maximum occupation probabilities for each site of configuration (b), averaged over 100 independent noise realisations, with $E = 0.0$ (black), $E = 0.1$ (darkgrey), $E = 1.0$ (grey) and $E = 1.5$ (light gray) levels of diagonal disorder. The y-axis representing the scale of the disorder E has some band gap regions omitted.

Fig. 4.12 and Fig. 4.13 represent the maximum occupation probabilities of the two chain configurations for cases with $E = 0.1$, $E = 1.0$, $E = 1.5$ and without added diagonal disorder, $E = 0.0$. For configuration (a) (Fig. 4.12), as the level of disorder increases, the maximum probabilities along the chain sites get higher in comparison with the unperturbed ($E = 0$) scenario (black profile). This means that the eigenstates are not uniformly spread anymore and they start to present Anderson localisation [152] (see also Section 3.2). It is seen however that the probability of the state being in the middle of the chain remains peaked at unity for levels of disorder of the order of $E \sim 1$.

Similarly, for configuration (b) (Fig. 4.13)) the states undergo localisation as the perturbation increases. The protected behaviour is also observed for the states peaking at the ends sites and at sites $i = \pm 1$ (the eigenstate that is closely approximated by $|\phi_0\rangle$ of Eq. 4.6). Remarkably, this last state is protected even when the growing Anderson localisation affecting the neighbouring sites induced by increasing disorder is greater than the topologically-induced localization as observed from the 'W' shape of the two profiles with higher disorder E. We also note that the two states with energies $\pm\sqrt{2}\Delta$, peaking at the mid point of the chain ($i = 0$) and with eigenstates that are closely approximated by the states $|\phi_-\rangle$ and $|\phi_+\rangle$ of Eq. 4.6, have some amount of protection but start to be affected for $E \sim 1$.

This behaviour can be further understood by observing the averaged energy spectrum for these same levels of disorder as shown in Fig. 4.14. With increasing disorder, the band energies spread and the band gaps shrink. Further increasing of

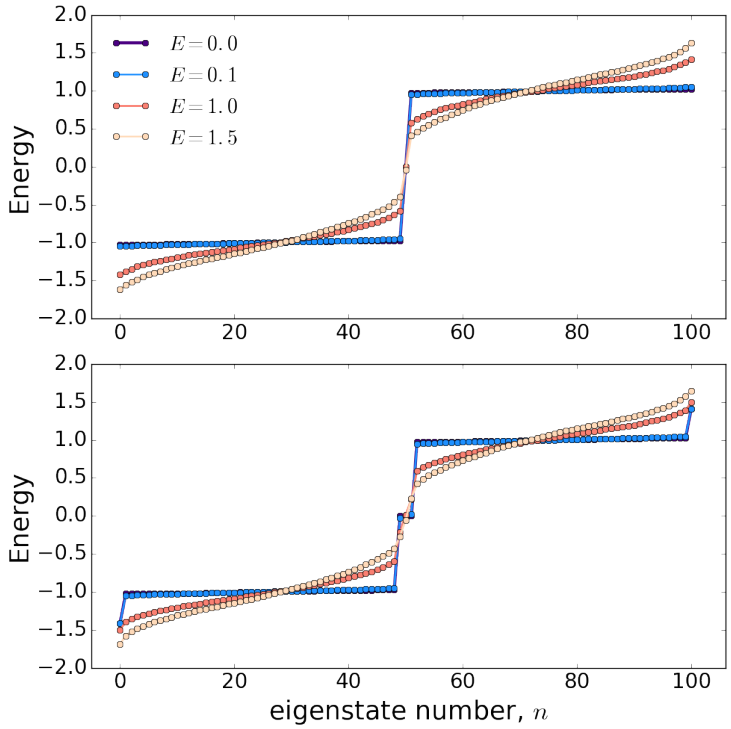

FIGURE 4.14: Energy spectrum of $N = 101$ sites spin chain with configuration (a) –upper panel– and (b) –lower panel–, averaged over 100 independent noise realisations and for different levels of diagonal disorder.

the disorder strength eventually closes the gaps and the protection suffers. However, we have observed that the localisation remains very strong: even with a disorder strength of $E = 3.0$ (three times the strong coupling value Δ) the unit peaks decrease by only 4%, so are still strongly localised with a probability $\rho_i \approx 0.96$. As already noted, the eigenstates approximated by states $|\phi_-\rangle$ and $|\phi_+\rangle$ of Eq. 4.6 that peak at site $i = 0$ are less protected against disorder than the other localised states because their energy gaps are somewhat smaller than those of the zero energy states.

4.4.2 Off-diagonal disorder

Off-diagonal disorder is another type of static disorder affecting the couplings between sites, as already introduced in Chapter 2. As the name indicates, such random errors affect the off-diagonal terms of the Hamiltonian. Similarly to the diagonal disorder we scale the perturbation added against the strong, Δ, coupling. The average of the maximum probabilities against site over 100 independent realisations for both configurations are shown in Fig. 4.15 and Fig. 4.16.

In contrast with what it was observed in the previous section, the localised states for both chain configurations are more affected by the off-diagonal disorder. This can be observed from the rapid decrease on the localised profiles from Fig. 4.15 and 4.16 as E gets larger. Even though the profile is still well-defined, its maximum probability decreases as much as ~ 0.6 when $E = 1.5$. In Fig. 4.17 the change on the peak

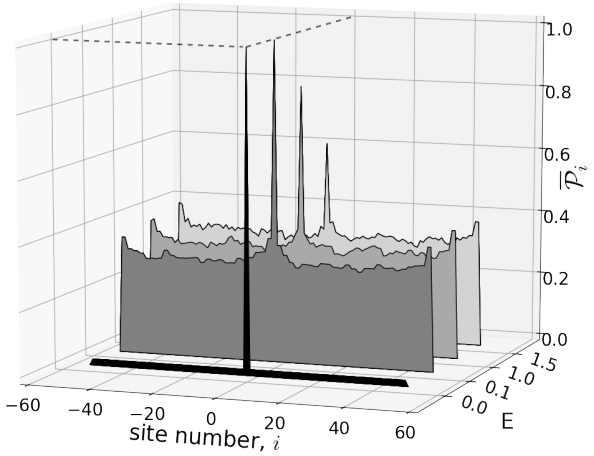

FIGURE 4.15: Maximum occupation probabilities for each site of configuration (a), averaged over 100 independent noise realisations, with $E = 0.0$ (black), $E = 0.1$ (darkgrey), $E = 1.0$ (grey) and $E = 1.5$ (light gray) levels of off-diagonal disorder. The y-axis representing the scale of the disorder E has some band gap regions omitted.

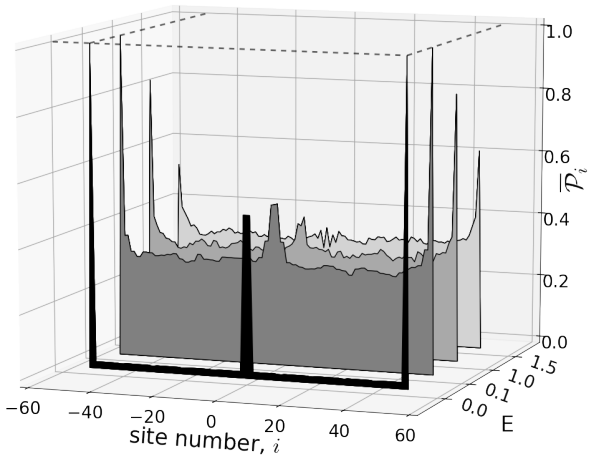

FIGURE 4.16: Maximum occupation probabilities for each site of configuration (b), averaged over 100 independent noise realisations, with $E = 0.0$ (black), $E = 0.1$ (darkgrey), $E = 1.0$ (grey) and $E = 1.5$ (light gray) levels of off-diagonal disorder. The y-axis representing the scale of the disorder E has some band gap regions omitted.

representing the localised state probability for both configurations and types of disorder is presented against the perturbation strength, E. There is a sharp difference between both disorder scenarios showing a faster decay of the localisation when the

couplings are affected. This difference is attributed to the nature of the off-diagonal perturbation: as the errors on the couplings get bigger, the more broken the dimerisation symmetry is and the system approximates to a fully uniform chain, hence the energy gap closes faster. We note that the localisation peak for configuration (a) has a more pronounced decay in the low perturbation regime because the localised site $i = 0$ is doubly disordered from errors due to the double nature of its coupling, while the localised site at $i = -m$ of configuration (b) is coupled to just one site.

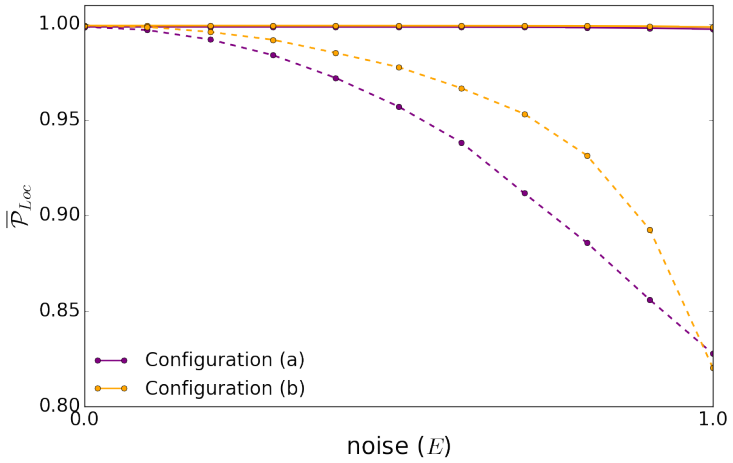

FIGURE 4.17: Maximum occupation probabilities for the localised sites $i = 0$ for configuration (a) (purple profile) and $i = -m$ for configuration (b) (yellow line) against diagonal (solid lines) and off-diagonal (dashed lines) disorder.

All these observations are clear signatures of the presence of topologically protected localised states in both types of configurations sitting in the middle of the energy gap. Even though we observe higher robustness of the system against diagonal disorder, it is important to note that we have here stressed the system up to unrealistically high levels of disorders (150% of the strong coupling Δ) and yet we get outstanding stability of the localised profiles. Indeed such states present for now the desired characteristics for the potential use of such system for storing applications.

4.5 Quantum memory applications

Over the last sections we have studied in detail the presence, nature and protection of localised states in our two chain configurations. Our findings suggest that such systems allow for any single qubit state injected into the sites where the localised state is confined to be stored in a robust manner. In this section we ought to explore if such behaviour is really attained, and therefore whether the system application as a quantum memory is something feasible.

In order to do so we inspect how disorder affects the dynamics of the system. In Section 4.2 we dealt with systems with a $|1\rangle$ state initialised (injected) at the sites

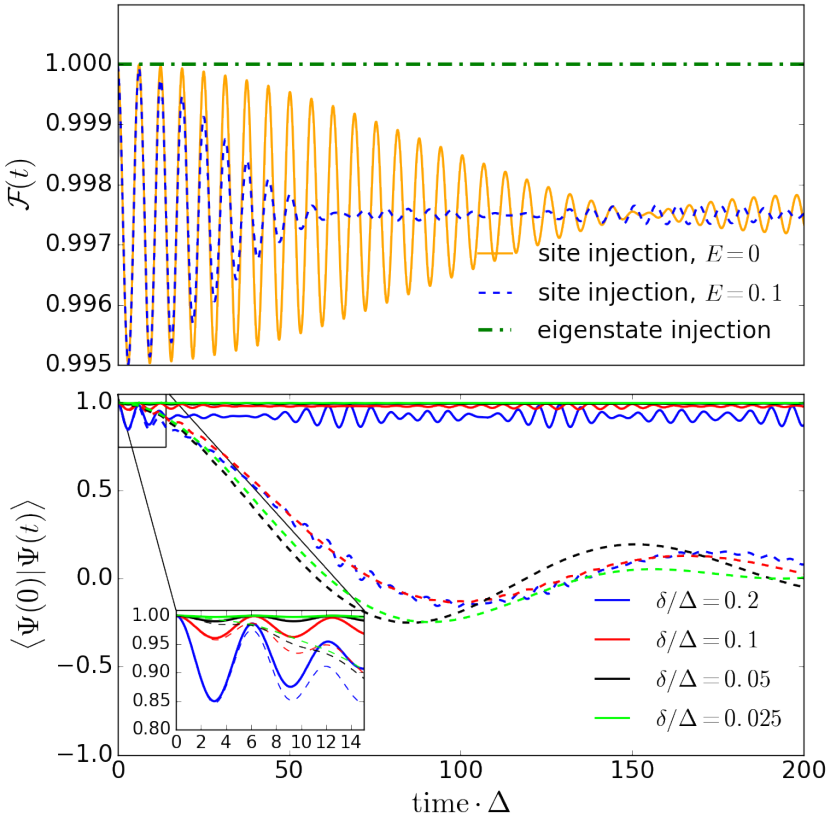

FIGURE 4.18: In the upper panel, fidelity of one initial excitation injected at the middle site (site encoding) containing the localised eigenstate of a $N = 21$ sites chain with configuration (a) and $\delta/\Delta = 0.025$ with no disorder (yellow profile) and 10% of diagonal disorder (blue profile). The green profile represents the fidelity of the initial state when the excitations is injected at the localised eigenstate (eigenstate encoding). In the lower panel, unperturbed phase dynamics of the excitation injected at the middle site (solid lines) and averaged disordered ($E = 0.1$) phase dynamics over 100 realisations (dashed lines) for a chain configuration (a), site encoding and different coupling ratios (δ/Δ).

with confined eigenstates that proved the localisation as the fidelity of the initial state remained very close to unity over time. The picture is still the same when the initial state is an arbitrary qubit state $\alpha|0\rangle + \beta|1\rangle$ and disorder is added and the amplitude of the dynamics, hence the fidelity, remains the same as the state remains within the energy gap (as seen on the upper panel of Fig. 4.18 for the injection at site $i = 0$ and diagonal perturbation $E = 0.1$).

On the other hand, the fidelity figure is not enough to ensure that the quantum state is indeed stored. Even though the amplitude, $||^2$, remains constant, relative phases between the qubit components could quickly intervene and destroy the coherence of the initial state. One way to check this is by looking at the phase dynamics of the initial state $\langle\Psi(0)|\Psi(t)\rangle$ and how it changes with disorder. When looking at the averaged phase over 100 noise realisations (lower panel of Fig. 4.18) we observe

that with no disorder (solid lines) the phase factor remains at 1 (similar to what happens with the fidelity). The oscillations in the site encoding fidelity are due to small components of non-localised energy eigenstates, so the frequency is dominated by Δ. These contributions from non-localised energy eigenstates become more significant as the coupling ratio is reduced. However, the phase coherence starts dropping when the diagonal disorder added is of a strength E=0.1 and adds a phase error to the initial state. This behaviour has been contrasted with different coupling ratios and it has been shown to be similar for all of them. The phase error makes the system presented under the current encoding unsuitable for quantum memory applications, as it represents a relative phase on a qubit superposition involving an amplitude with no excitation and an amplitude with one site excitation.

Nevertheless, in the case at hand, because of the potentially very strong spatial localisation of the protected states, we can encode instead a single logical qubit for each of the topologically localised eigenstates ($|\varphi_L\rangle$), with presence or absence of the excitation being in the $|1_L\rangle$ or $|0_L\rangle$ qubit state, respectively, such that,

$$|\Psi_L(t)\rangle = \alpha|0_L\rangle + \beta e^{-iE_L t/\hbar}|1_L\rangle \tag{4.8}$$

This latter 'eigenstate encoding' allows the use of these protected states as qubits even when their spatial localisation is not so strong and the physical states extend over several spins, as long as the eigenstate remains isolated in an energy gap and thus accessible through energy-specific addressing. In this case the number of logical qubits that a system could host would depend on the number of topological protected 'solitons' or defects embedded in its couplings' structure.

The probability of finding the state initially injected at the localised state (eigenstate encoding) is constant at unity (dashed green profile of upper panel of Fig. 4.18). Thus the eigenstate encoding alternative for storing applications becomes very relevant. For configuration (a), even though the localised state will remain protected (within an energy gap) when diagonal disorder is added, it will shift an energy ΔE_L (see left panel of Fig. 4.19). In that case the qubit should be encoded into the perturbed localised eigenstate at energy ΔE_L. As the state remains well within the large gap, its energy should be relatively easily identified experimentally. Hence although both encodings will present a phase oscillation, the use of the eigenstate encoding and the fact that the initial state will be injected into a well known eigenstate at ΔE_L will allow us to know the periodicity of this phase and hence correct for it, if needed.

However, when off-diagonal disorder is affecting the system, the quantum state can still be encoded at the localised site. The encoded state will not suffer phase errors and will remain localised as long as the level of disorder is not large enough to close the gap. This behaviour is caused by the symmetric nature of the off-diagonal disorder. In Section 4.2 we explained how the energy spectrum is constructed as even and odd superpositions of the now perturbed (by ε) dimer states, and therefore will have energies of $\Delta + \varepsilon$ and $-\Delta + \varepsilon$. Because of this, the symmetry over the zero energy level of the spectrum is preserved (as shown in the right panel of Fig.

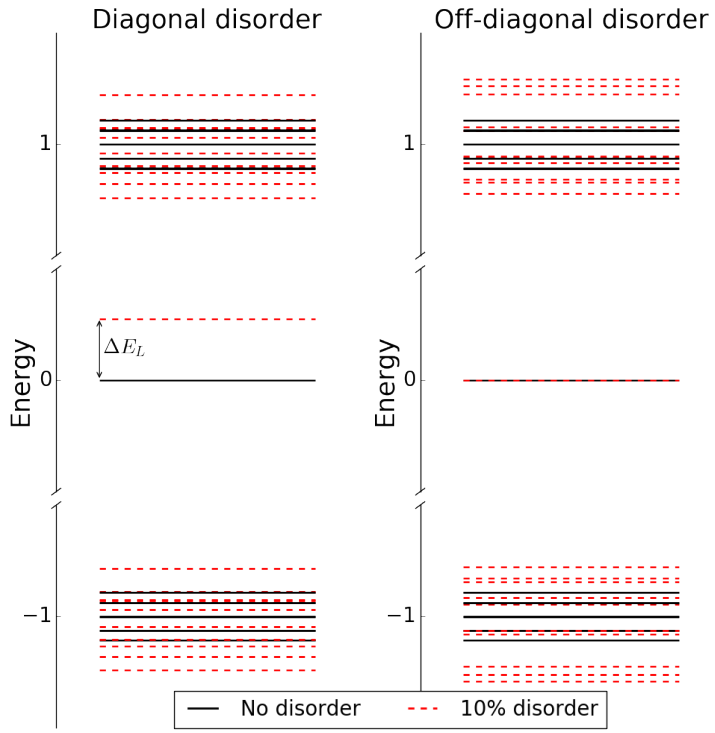

FIGURE 4.19: Energy levels for a $N = 21$ sites spin chain with configuration (a) with no noise (black solid lines) and 10% (red dashed lines) of diagonal (left panel) and off-diagonal (right panel) disorder.

4.19) and the localised state sitting in the middle of the gap remains unperturbed. The possibility of safely injecting the initial state directly on site may be indeed convenient to the user as there is no need to inject at a given energy, as for the eigenstate encoding.

Depending on the physical realisation implementing our chain configurations different types of disorder will be encountered. Quantum memory applications will be able to be attained given that the appropriate encoding is chosen. When diagonal disorder is affecting the system, the use of the eigenstate encoding will allow protection of the localised state from phase errors up to 300% of Δ, but with the added difficulty of having to inject the initial state at the precise ΔE_L energy. On the other hand, when off diagonal disorder is present, even though less robust (the localised states are protected up to 100% of Δ), we can still safely use the site encoding and inject the state at the defect site with the zero-energy confined state associated with no phase errors taking place.

4.6 Summary

Over this chapter we have investigated the presence and robustness of topologically localised states in engineered spin chains, inspired by the SSH model and relying on the dimerisation of their sites. The presence of these states can be selectively manipulated through control of the chain coupling distribution and length. Localised

states can be engineered to exist at the centre and/or the ends of the chain, as in configurations (a) and (b).

We have shown that these topologically localised states exhibit a high level of protection to increasing diagonal and off-diagonal disorder, with higher protection resulting from larger energy gaps. These gaps, along with the rest of the energy spectrum, depend directly on the coupling ratio δ/Δ and such dependence has been investigated. The protection and robustness is an essential requirement when thinking of quantum architecture components. In order to attain completely robust localised states against fabrication defects and avoiding phase errors for quantum memory applications we propose two different types of encoding: state injected at the localised site or at the energy of the localised eigenstate, each of which yields favorable results depending on the type of disorder perturbing the system. The presence of these localised states therefore provides an interesting system presenting two or more degenerate zero-energy states in which to encode protected quantum information. We can thus conclude that such systems are good potential candidates from which to design a quantum memory device.

Members of these dimerised families of spin chains with such symmetry breakers, when engineered and combined, could also represent promising elements for the construction of more complex quantum logic networks, thus providing a novel system with which to perform quantum information processing. In order to investigate such applications, in our next chapter we will examine the dynamics, state transport and computational abilities such as entanglement generation of appropriate spin chain systems inspired by the above types in a more extensive way, along with the robustness of these applications to disorder.

Chapter 5

Spin chains as quantum entangling gates

In this chapter we model a dimerised spin chain embedding three defects or weakly coupled sites. Three different entangling protocols are proposed as well as their latter storage, one producing a Cluster state and two generating a Bell state, depending on the initial state injection. The potential use of such protocols as quantum entangling gates and its robustness is considered. Part of this work has been published in: **M. P. Estarellas, I. D'Amico & T.P. Spiller**, "Robust Quantum Entanglement Generation and Generation-plus-Storage Protocols with Spin Chains", Phys. Rev. A **95**, 042335, (2017) and **K. N. Wilkinson, M. P. Estarellas, I. D'Amico & T.P. Spiller**, "Rapid and Robust Generation of Einstein-Podolsky-Rosen Pairs with Spin Chains", Quant. Inf. Comp. **18(3&4)**, 0249–0266, (2018).

At the lowest level of the physical layer of any classical computer architecture we encounter integrated circuits made up of many logic gates. Each of these gates is designed to perform a specific logical operation, a set of which will define any sort of computation and allow for universality (universal Turing machine). As an example, the arithmetic logic unit or ALU is one of the most essential components of any processor and is nothing more than an integrated combinational logic circuit designed to do some simple but essential arithmetic operations (add, subtract, increment, decrement, etc) to strings of binary code or bits.

With the quantum ingredient, technology needs to deal with other capabilities offered by the exotic nature of the quantum systems. One of the most important of these capabilities is entanglement. Many operations in quantum information rely on the sharing of entangled qubits between different parties, such as teleportation protocols [191], dense coding [27], and one-way quantum computing [192]. Therefore, such quantum phenomenon constitutes an essential resource for many applications in quantum technology. Accordingly, and analogously to classical computing, a universal set of gates able to operate under the rules of quantum logic is on demand (as already stated in Section 1.1.3 where DiVincenzo list [54] was analysed). Among

them, quantum entangling gates will be essential for the exploitation of the technology power of a true quantum Turing machine as well as other applications in quantum communications.

Over the years, several proposals for the generation of entangled states have been made and successfully realised experimentally. In solid-state implementations, previous works report the use of spin chains to allow for entanglement generation through different approaches. One of them studies the so called long distance entanglement generation [72, 77, 79, 82] which refers to the presence of a Bell state-like eigenstate between the edges of an antiferromagnetic chain. Another approach requires the moving of spin entities adiabatically [193, 194] in order to create entanglement. Other methods of generating entanglement include the use of correlated static disorder [195], due to fermionic exchange [73], using branched systems [129] or kondo chains [62].

In this context, this chapter will show how our set of proposed spin chain configurations, that we name ABC-type spin chains, allow for entanglement generation without being susceptible to some of the limitations of previous proposals. Our proposed device has the advantage of using physically static qubits (or 'stationary qubits') and is based upon their natural dynamics. This gives ABC-type chains the potential to fulfill the role of gates between closely spaced distanced quantum registers. In addition, this protocol is driven by the natural dynamics of the chain limiting the need of user interaction with the system. However, note that some interaction is required as initialisation and extraction of the desired input/output states will be needed. Depending on the initial state injected to the system, the protocol will lead to two different maximally entangled states: a cluster state or a Bell state. Based on the same principles seen in the previous chapter, this protocol also offers the possibility of localizing and therefore storing the entangled state. We have tested the resilience of the protocol against fabrication defects, by adding random fluctuations to both the sites and the couplings of the chain, as well as time delays, by variating the injection times when dealing with simultaneous initialisations involving more than one site. Highly favourable results have been obtained showing clear optimism in the prospective use of such devices for real application. In this line, we have gone a step forward by seeking a compromise between the fidelity of the desired entangled state, the overall robustness of the protocol and, quite importantly, the time needed for the entanglement operation to deliver. Such times are very relevant features of the device due to the necessity to have quickly operating gates able to perform as many operations as possible before the coherence of the qubits implementation decays.

5.1 ABC-type spin chains

The system considered in this chapter to serve as an entangling gate is a spin chain of $N = 7$ sites with alternating weak (δ) and strong (Δ) couplings, in a distribution

such that there are three sites (labeled A, B and C) weakly coupled to the rest of the chain as shown in Fig. 5.1.

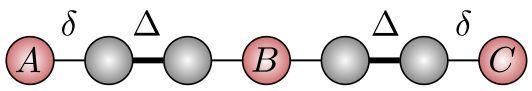

FIGURE 5.1: ABC-type spin chain configuration.

This spin chain can be described by the following time independent Hamiltonian (see Section 2.1.1 for more detail),

$$\mathcal{H} = \sum_{i=1}^{N} \epsilon_i |1\rangle\langle 1|_i + \sum_{i=1}^{N-1} J_{i,i+1}[|1\rangle\langle 0|_i \otimes |0\rangle\langle 1|_{i+1} + h.c.], \tag{5.1}$$

with $J_{i,i+1}$ equal to either Δ or δ depending on the site (see Fig. 5.1). In previous literature [1, 196, 197] it has been demonstrated that related dimerised chains have high fidelity quantum state transfer (QST) properties, something that we will exploit in our protocol in order to generate the desired entangled state.

5.2 Entanglement generation protocols

The entanglement generation protocol can be illustrated in the form of the schematic diagram shown in Fig. 5.2. The initial injection, which will define the overall initial state of the chain, is of particular relevance. First, it is one of the only two interactions the user has to make with the system, and second, because it will determine the final entangled state. Table 5.1 shows the three different initial states we are considering and the site of the chain into which they are locally injected (simultaneous double excitation states injections at A and C sites, or single excitation state injection at B site).

We then let the system naturally evolve to a given time. This entangling time, t_E, depends on the version of the protocol we use depending on the state to be generated (Cluster or Bell state). For the Cluster state generation, this is the mirroring time ($t_E \approx t_M$), the time needed for an arbitrary initial state to propagate to its mirror position in the system. However, for the Bell state generation, this time is approximately half the mirroring time ($t_E = t_M/2$). In all cases, at t_E the system state becomes maximally entangled between sites A and C. The two entangled qubits can be extracted – if desired – from sites A and C at the extraction time t_E. An alternative to this is to protectively store the state using a slightly modified system configuration and the protocol, as we will show later in this chapter (see Section 5.5).

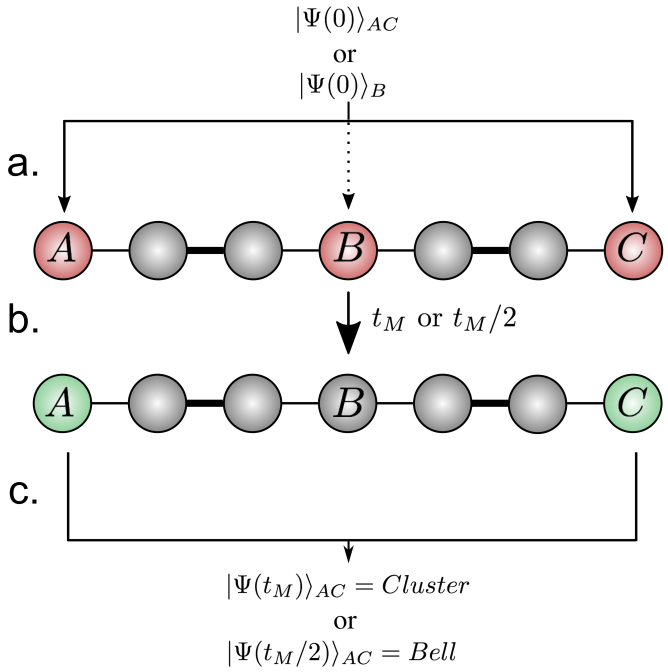

FIGURE 5.2: Entangling protocol. (a) Initial injection (red) at sites A and C (solid arrows) or at site B (dashed arrow). (b) Evolution of the system up to time $t_E \approx t_M$ or $t_E \approx t_M/2$. (c) Generation of a maximally entangled Cluster state or Bell, respectively, between sites A and C (green).

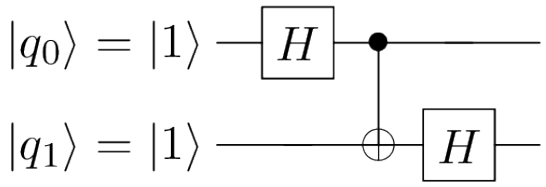

FIGURE 5.3: Cluster state creation written as a circuit.

5.2.1 Cluster state creation

Let us now investigate in more detail the protocol for the generation of the cluster state. The equivalent circuit to represent our cluster state generation gate is presented in Fig. 5.3. A cluster state is a maximally entangled state formed by an equal superposition of all the site basis vectors. In this case, the protocol is initiated at $t = 0$ with the injection of two initial $|+\rangle = \frac{1}{\sqrt{2}}(|0\rangle + |1\rangle)$ states at the chain ends (sites A and C). We can write the initial state in the standard basis as

$$|\Psi(0)\rangle_i = \frac{1}{2}\Big(|+\rangle_A \otimes |+\rangle_C\Big) \otimes |0\rangle_{rest-of-chain} = \frac{1}{2}\Big(|0\rangle_A|0\rangle_C + |1\rangle_A|0\rangle_C + |0\rangle_A|1\rangle_C + |1\rangle_A|1\rangle_C\Big) \otimes |0\rangle_{rest-of-chain}. \quad (5.2)$$

First, the fidelity of the initial state is calculated and presented as the red profile

Entangling Protocols			
	Initial state	**Entangled State**	$\mathbf{t_E}$
i	$\|\Psi(0)\rangle_{AC} = (\|+\rangle_A \otimes \|+\rangle_C)$	$\|\Psi(t_E)\rangle_{AC} = \frac{1}{2}(\|00\rangle_{AC} - \|01\rangle_{AC} - \|10\rangle_{AC} - \|11\rangle_{AC})$	t_M
ii	$\|\Psi(0)\rangle_{AC} = \|1\rangle_A \otimes \|1\rangle_C$	$\|\Psi(t_E)\rangle_{AC} = \frac{-i}{\sqrt{2}}(\|10\rangle_{AC} + \|01\rangle_{AC})$	$t_M/2$
iii	$\|\Psi(0)\rangle_B = \|1\rangle_B$	$\|\Psi(t_E)\rangle_{AC} = \frac{-i}{\sqrt{2}}(\|10\rangle_{AC} + \|01\rangle_{AC})$	$t_M/2$

TABLE 5.1: Initial injections and their corresponding product entangled states at $t_E \approx t_M$ or $t_E \approx t_M/2$. The $|+\rangle$ state corresponds to $\frac{1}{\sqrt{2}}(|0\rangle + |1\rangle)$. For simplicity, only the states of the relevant sites (A, C or B) are presented and a compact notation is used.

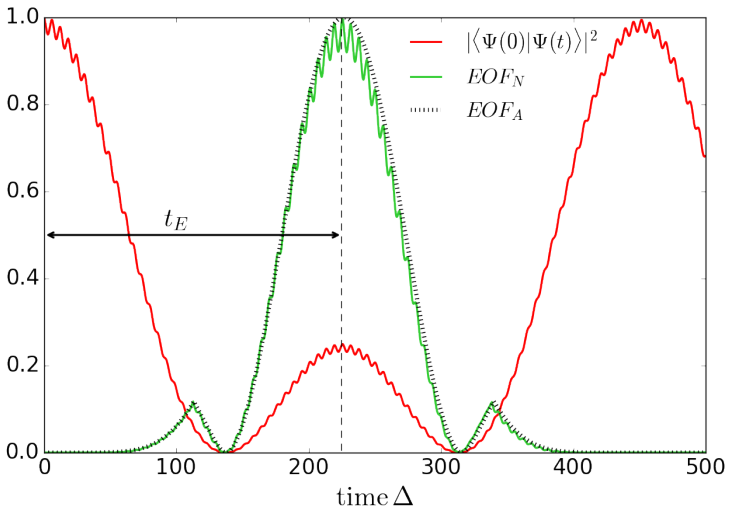

FIGURE 5.4: Fidelity of the initial state $|\Psi(0)\rangle_{AC}$ [i] (red profile) and numerically calculated EOF_N (green profile) for a $N = 7$ ABC spin chain and $\delta/\Delta = 0.1$. Blacked dashed profile is the analytically obtained EOF_A of the system derived from the trimer model.

in Fig. 5.4, which is the probability of recovering the initial overall state as a function of time, $\mathcal{F}(t) = |\langle\Psi(0)|\Psi(t)\rangle|^2$, i.e. the overlap between the initial state and the overall state at any time (see Chapter 2). From Fig. 5.4, we observe that the fidelity (red profile) peaks up to unity at twice (and even multiples of) the mirroring time, so at $2t_M$, $4t_M$, etc. This means that the dynamics of the system evolves in a periodic fashion and the initial state is recovered regularly. We now obtain the EOF between sites A and C, which is a bipartite measure of entanglement (see Section 2.2.3 for more details about this measure). At the mirroring time, the EOF (green profile) is maximum. Two qubits are maximally entangled when $EOF = 1$ and our results show that the two qubits states A and C approach this condition and their state can be approximated as it follows:

$$|\Psi(t_E)\rangle \approx \frac{1}{2}\Big(|0\rangle_A|0\rangle_C - |1\rangle_A|0\rangle_C - |0\rangle_A|1\rangle_C - |1\rangle_A|1\rangle_C\Big) \otimes |0\rangle_{rest-of-chain}. \tag{5.3}$$

The state is very similar to the initial one but with the crucial difference of three additional -1 signs which make the state impossible to separate in a product state of qubits A and C.

Trimer model approximation

This behavior can be understood analytically if we consider the Hamiltonian of an effective, one-excitation subspace, reduced 'toy model' with just three sites ABC equally coupled ($J_{AB} = J_{BC} = \eta$) so the presence of the dimers in between for the original model is encapsulated into this η interaction,

$$H = \begin{pmatrix} 0 & \eta & 0 \\ \eta & 0 & \eta \\ 0 & \eta & 0 \end{pmatrix} . \tag{5.4}$$

The trimer eigenstates resulting from the Eq. 5.4 diagonalization are given by

$$|\phi_-\rangle = \frac{1}{2}\begin{pmatrix} -1 \\ \sqrt{2} \\ -1 \end{pmatrix} \; |\phi_0\rangle = \frac{1}{\sqrt{2}}\begin{pmatrix} 1 \\ 0 \\ -1 \end{pmatrix} \; |\phi_+\rangle = \frac{1}{2}\begin{pmatrix} 1 \\ \sqrt{2} \\ 1 \end{pmatrix}, \tag{5.5}$$

with $|\phi_-\rangle$ having energy $E_- = -\sqrt{2}\eta$, $|\phi_0\rangle$ having energy $E_0 = 0$, and $|\phi_+\rangle$ having energy $E_+ = \sqrt{2}\eta$.

We can now write the initial state (Eq. 5.2) in terms of these eigenstates and each of them can be time evolved through its propagator (e^{-iEt}):

$$|\Psi(t)\rangle = a_- e^{-iE_-t}|\phi_-\rangle + a_0 e^{-iE_0t}|\phi_0\rangle + a_+ e^{-iE_+t}|\phi_+\rangle, \tag{5.6}$$

where a_-, a_0 and a_+ are the coefficients resulting from mapping the initial state from the site basis (Eq. 5.2) into the eigenstate basis (Eq. 5.5),

$$\begin{aligned} a_- &= \langle\phi_-|\Psi(0)\rangle \\ a_0 &= \langle\phi_0|\Psi(0)\rangle \\ a_+ &= \langle\phi_+|\Psi(0)\rangle. \end{aligned} \tag{5.7}$$

It is important to note that in this special case there is no need to consider the second excitation subspace in the Hamiltonian as it will be equivalent to the one excitation subspace. Therefore, the diagonalisation of the full one- and two-excitations subspace would lead to three pairs of degenerate eigenstates with their corresponding eigenvalues. This is because, as we are dealing with the special case of a trimer,

the eigenstates and eigenvalues (and therefore the evolution) of the two excitations states will be equivalent to the one excitation states due to the particle-hole symmetry of the site basis set ($|100\rangle \rightarrow |011\rangle$, $|010\rangle \rightarrow |101\rangle$, $|001\rangle \rightarrow |110\rangle$). Similarly, we do not include the $|000\rangle$ state in the trimer representation as it does not evolve at all but it has to be considered for the proper normalization of the overall state.

It can be then shown that all the terms of our initial state (except the inert $|0\rangle_A|0\rangle_C$ state) will acquire a -1 phase factor at the mirroring time, giving the overall state of Eq. 5.3. The mirroring time will be equal to half the time needed for all the propagators of the eigenstates to be equal to unity (at a time $2t_M$), this is the time needed to revive the system into its initial state. Given that one of the eigenstates does not evolve ($E_0 = 0$), such time is found solving the following system of equations,

$$\begin{cases} e^{-i\sqrt{2}\eta 2t_M} = 1 \\ e^{i\sqrt{2}\eta 2t_M} = 1, \end{cases} \tag{5.8}$$

and therefore the mirroring time (which approximates to the entangling time t_E) is resolved to be $t_M = \pi/\sqrt{2}\eta$.

Following a similar line, the EOF profile for the reduced model has been analytically characterized. The overall state for this trimer system, after initialisation, at any time can be written as

$$\begin{aligned} |\Psi(t)\rangle = \frac{1}{2}\Big(|0\rangle_A|0\rangle_C + \cos(\sqrt{2}\eta t)\big(|1\rangle_A|0\rangle_C + |0\rangle_A|1\rangle_C + |1\rangle_A|1\rangle_C\big)\Big)|0\rangle_B \\ -\frac{i}{\sqrt{2}}\sin(\sqrt{2}\eta t)\Big(|0\rangle_A|0\rangle_C + \frac{1}{2}|1\rangle_A|0\rangle_C + \frac{1}{2}|0\rangle_A|1\rangle_C\Big)|1\rangle_B\,. \end{aligned} \tag{5.9}$$

As introduced in Chapter 2, the first step to calculate the EOF is to find the reduced density matrix of the two qubits involved. For our state, this is done by tracing out site B, giving the form

$$\rho_{AC} = |\alpha_{AC}\rangle\langle\alpha_{AC}| + |\beta_{AC}\rangle\langle\beta_{AC}|, \tag{5.10}$$

where the unnormalised components are given by

$$\begin{aligned} |\alpha_{AC}\rangle = &\frac{1}{2}\Big(|0\rangle_A|0\rangle_C + \cos(\sqrt{2}\eta t)\big(|1\rangle_A|0\rangle_C + |0\rangle_A|1\rangle_C \\ &+ |1\rangle_A|1\rangle_C\big)\Big), \end{aligned} \tag{5.11}$$

and

$$\begin{aligned} |\beta_{AC}\rangle = &-\frac{i}{\sqrt{2}}\sin(\sqrt{2}\eta t)\Big(|0\rangle_A|0\rangle_C \\ &+ \frac{1}{2}|1\rangle_A|0\rangle_C + \frac{1}{2}|0\rangle_A|1\rangle_C\Big)\,. \end{aligned} \tag{5.12}$$

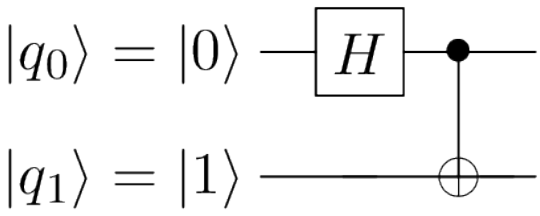

FIGURE 5.5: Bell state creation written as a circuit.

At $t = t_M$, $\sin(\sqrt{2}\eta t) = 0$ and $\cos(\sqrt{2}\eta t) = -1$ and Eq. 5.10 reduces to the pure state given by Eq. 5.11, which at this point is maximally entangled due to the additional -1 phase factors. We compute the EOF for such an approximated state at all times, by considering η as the effective coupling between $A - B$ and $B - C$ of the original $N = 7$ site chain. Its value can then be obtained by the eigenvalues immediately above (or below) zero of the overall spectrum and knowing that $E_+ = \sqrt{2}\eta$ ($E_- = -\sqrt{2}\eta$). In terms of the original chain parameters, this gives,

$$\eta = \frac{\Delta}{2}\sqrt{1 + 3(\frac{\delta}{\Delta})^2 - \sqrt{1 + 6(\frac{\delta}{\Delta})^2 + (\frac{\delta}{\Delta})^4}}, \tag{5.13}$$

(see Appendix A –'Derivation of η'– for further details on this derivation). After scaling the state dynamics against Δ, we obtain an approximate profile to the full numerical result, as shown by the black dashed line of Fig. 5.4. Clearly the trimer approximation accurately reproduces the overall entanglement evolution, without though the fine oscillations that are due to the full chain dynamics.

Once the effective coupling η is known, the entangling time can also be analytically approximated as $t_E = t_M = \pi/\sqrt{2}\eta$. We thus provide an analytic interpretation of the system behavior that demonstrates the importance of the presence of sites A, B and C for the operation of our protocol, mathematically validates the entangled state formation, and gives accurate recipes to obtain a value for η and, consequently, the required extraction time t_E.

5.2.2 Bell state creation

In this version of the protocol the dynamics of the spin chain generates a Bell state or EPR pair. The equivalent circuit to represent the Bell state generation gate is presented in Fig. 5.5. This same state can be achieved by using two different system initialisations, the (ii) simultaneous injection of two excitations at sites A and C or (iii) single-excitation injection at site B. These possibilities present different advantages. The single injection at the centre allows generation and distribution of a Bell state with the convenience and easiness of having to initially interact with one site only (site B). However, some applications such as modular quantum processor proposals may need to generate this same state with simultaneous compliance and contribution of two distant parties or quantum registers [198], i.e. the two parties A and C

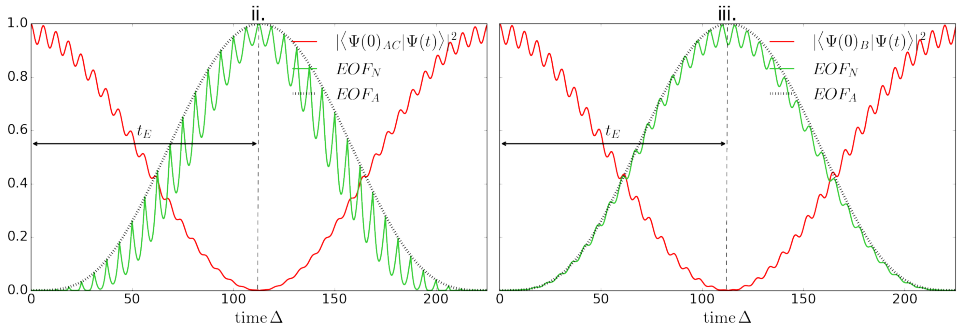

FIGURE 5.6: Fidelity of the initial state $|\Psi(0)\rangle_{AC}$ [ii - left panel] and $|\Psi(0)\rangle_B$ [iii - right panel] (red profile) and numerically calculated EOF_N (green profile) for a $N = 7$ ABC spin chain and $\delta/\Delta = 0.1$. Blacked dashed profile is the analytically obtained EOF_A of the system derived from the trimer model.

may need to agree priori initiating the protocol. We can then write the state of the chain at $t = 0$ as follows:

$$\text{ii) } |\Psi(0)\rangle_{ii} = \big(|1\rangle_A \otimes |1\rangle_C\big) \otimes |0\rangle_{rest-of-chain}. \tag{5.14}$$

$$\text{iii) } |\Psi(0)\rangle_{iii} = |1\rangle_B \otimes |0\rangle_{rest-of-chain}. \tag{5.15}$$

Similarly to the cluster state creation protocol, in Fig. 5.6 we consider the evolution of both initial states and observe a maximum peak of EOF at what is now half the mirroring time, $t_M/2$. At this time, the state between site A and C is a maximally entangled Bell state.

Again, this can be analytically explained by approximating the problem to the reduced trimer as in Eq. 5.4 and Eq. 5.5. As already covered in the previous section, due to particle-hole symmetry of this particular system, we can consider the one-excitation states equivalent to the two-excitation ones such that the initial state (ii) will be mathematically equivalent to (iii) ($|101\rangle \rightarrow |010\rangle$). This simplifies the analysis allowing us to only expand on the analytics of the (iii) type injection, where one excitation is injected at site B.

The initial state can thus be decomposed in terms of the trimer eigenstates,

$$|\Psi(0)\rangle_{iii} = \frac{1}{\sqrt{2}}\big(|\phi_+\rangle + |\phi_-\rangle\big). \tag{5.16}$$

As done before, the state of the system at any time can be found by evolving each of the eigenstates in Eq. 5.16 through its propagator (e^{-iEt}). At the mirroring time, $t_M = \frac{\pi}{\sqrt{2}\eta}$, the system will have returned to its initial position. This differs from the previous protocol and t_M coincides with the time where the fidelity of the initial state is equal to unity, as the mirrored state is by symmetry equal to the initial one. At half this time ($\frac{t_M}{2}$), though, we see from the numerical results presented in Fig. 5.6 that EOF becomes maximum and our state at that time can be written as,

$$|\Psi(\frac{t_M}{2})\rangle_{iii} = \frac{1}{\sqrt{2}}(e^{-iE_+\frac{\pi}{2\sqrt{2}\eta}}|\phi_+\rangle + e^{-iE_-\frac{\pi}{2\sqrt{2}\eta}}|\phi_-\rangle). \tag{5.17}$$

Using the explicit expression of the basis vectors, this yields to the expected maximally entangled Bell state between sites A and C:

$$|\Psi(\frac{t_M}{2})\rangle_{iii} = \frac{-i}{\sqrt{2}}\big(|1\rangle_A|0\rangle_C + |0\rangle_A|1\rangle_C\big) \otimes |0\rangle_B. \tag{5.18}$$

Similarly, due to particle-hole symmetry, a bit-flip operation on the state obtained in Eq. 5.18 leads the state generated through (ii) initial injection,

$$|\Psi(\frac{t_M}{2})\rangle_{ii} = \frac{-i}{\sqrt{2}}\big(|0\rangle_A|1\rangle_C + |1\rangle_A|0\rangle_C\big) \otimes |1\rangle_B. \tag{5.19}$$

As the analytic envelope shown in Fig. 5.6 shows, this treatment is a good approximation for the part of the system we are concerned with and explains the observed numerical behaviour. As per in the previous section, the effective coupling η and, therefore, the mirroring time t_M can be approximated from Eq. 5.13. Hence, we can have an approximate idea of when the sites A and C will become maximally entangled. In that sense, the trimer model is a useful way to predict the time scale of the dynamics. However, let us note that one thing is the time scale and the other is the dynamics per se. We can already see that even though the trimer approximates well the curve of the dynamics (as shown in Fig. 5.4), it does not account for the secondary oscillations seen in the real dynamics. Such oscillations are due to the interplay of a more complicated spectrum, consequence of the additional levels caused from the presence of the dimers and a larger excitation subspace that now also accounts for two excitations. Furthermore, for the entangled state obtained from (ii) injection, the real state from the $N = 7$ system dynamics is poorly approximated. This is due to the fact that the excitation that sits at site B in the entangled state obtained from the reduced model (Eq. 5.19) is in reality delocalised over several sites such that the state takes the form:

$$|\Psi(\frac{t_M}{2})\rangle_{ii} = \frac{1}{\sqrt{2}}\big(|1\rangle_A|0\rangle_C + |0\rangle_A|1\rangle_C\big) \otimes \big[\alpha|1\rangle_{\text{B}}|0\rangle_{\text{rest-of-chain}} + \beta|0\rangle_{\text{B}}|\chi\rangle_{\text{rest-of-chain}}\big] \tag{5.20}$$

Nevertheless, note that the picture for the Bell state involving qubit A and C, which is the part of the state we are concerned about, is not affected.

5.3 Robustness of the protocols

5.3.1 Random static disorder

Any practical application of such protocols will be subject to the presence of fabrication errors in the construction of the device. We have therefore investigated the effects on the generation of the two entangled states after introducing two different types of random static disorder into our system. By considering two different types of such perturbations we aim to simulate a wide range of realistic physical systems subject to different noises. Similarly, we investigate the time delays of asynchronous initial injections (specifically for cases (i) and (ii)) and how those affect the amount of entanglement generated in the final state.

The first approach to model local fabrication errors is to consider energy fluctuations affecting the sites themselves, and this is attained by adding random diagonal disorder to the Hamiltonian. This type of disorder can be understood as an on-site random potential. In our second approach we consider static errors in the couplings by introducing off-diagonal random noise to the Hamiltonian (see Chapter 2). Both types of perturbations have been scaled to the characteristic energies of the system by weighting them against the weak, δ, coupling. In order to have an understanding of the practical impact of these two types of fabrication errors, we also consider the case where both disorders are present. We simulate this by adding a randomized perturbation simultaneously to both diagonal and off-diagonal terms of the Hamiltonian.

In the following we compare two scenarios. In the first, given the stochastic nature of these calculations, we present an (ensemble) average over 1000 realisations (EOF_{1000}) of the EOF computed at exactly the entangling time, t_E, that is expected for the perfect system. Of course in the disordered systems there may well be an error in the actual time at which the EOF peaks; however, in this first scenario we assume that this timing error is unknown and we take the entanglement at the expected ideal time for it to peak and average this.

The second scenario corresponds to cases where the timing error could be known in advance. The maximum EOF over a time window is then calculated and, again, the (ensemble) average over 1000 realizations presented. Given that we are here considering fabrication disorder, this would be equivalent to the calibrations which are implemented routinely on current electronic components to get their exact specifications through a set of independent measurements on each device. Calibration would enable the state extraction to be performed at the time when the EOF is maximum, for each individual (disordered) device. For this reason there is also significant value in considering the average maximum EOF over a time window. This time window has been taken to be of a complete time period of the fidelity of the initial state, $\sim 2t_M$.

The robustness of the protocol is strongly linked to the nature of the initial injected state. For this reason let us first consider the effect of disorder separately for

each of the three cases shown in Table 5.2 and then comment on the features they have in common.

i) Protocol with initial state $|\Psi(0)\rangle_{AC} = (|+\rangle_A \otimes |+\rangle_C)$

To begin, we consider the results from the first scenario for the cluster state generation, this is considering the average EOF at the exact t_E (Fig. 5.7, blue symbols and shades). These show that the entanglement, at the extraction time t_E predicted for the perfect device, and with disorders smaller than 10% of the weak coupling δ, is very high ($EOF_{1000} > 0.9$) for both types of noise. However, when the disorder levels increase, for the case of diagonal disorder the EOF drops sharply, reaching $EOF_{1000} \sim 0.2$ with a disorder level at 50% of the weak coupling. Nevertheless, at this same level of off-diagonal disorder the averaged entanglement is still considerably high ($EOF_{1000} \sim 0.6$).

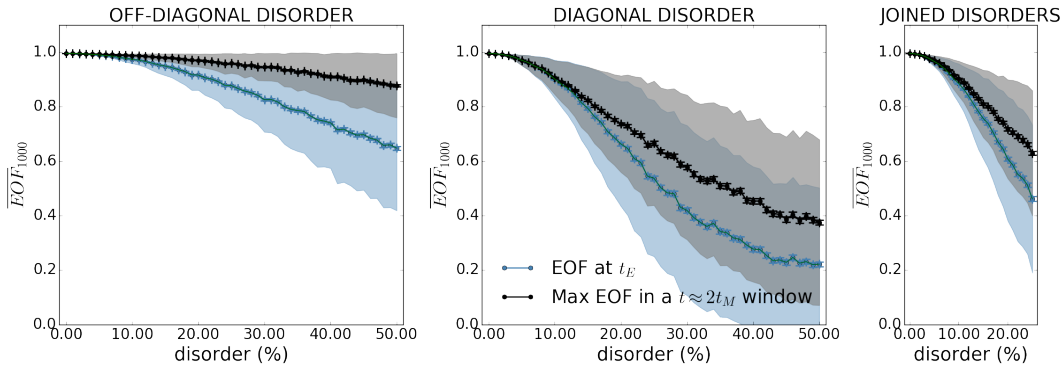

FIGURE 5.7: Averaged EOF at t_E (blue -lower- line) and maximum EOF over a 500 units of time window (black -upper- line) for different levels of off-diagonal, diagonal and both disorders weighted against the weak coupling (δ) for protocol (i) and $\delta/\Delta = 0.1$. Black and blue shadows represent the standard deviation, black and blue bars represent the standard error of the mean.

These values improve considerably in the second scenario we consider, that is if there is the possibility of making additional independent measurements on each device (calibration). As seen in Fig. 5.7 (second panel, black symbols and gray shades), when considering diagonal disorder, the maximum entanglement over a time window of 500 units of time does not go lower than $EOF_{1000} = 0.4$ even with noise perturbations at 50% of the weak coupling.

For disorder added to the couplings this second scenario is extremely robust, with maximum average entanglement value over the time window always above $EOF_{1000} = 0.9$ even for noise perturbations at 50% of the weak coupling (Fig. 5.7, first panel, black symbols and gray shades).

When both disorders are added (third panel of Fig. 5.7, where we plot up to 25% disorder), we get a similar trend to the one obtained with the effect of diagonal disorder only in both EOF measurements. We can conclude from this that disruption

from diagonal fabrication errors will be dominant for this system, and so reduction of these is the most important practical challenge with regard to fabrication errors.

ii) Protocol with initial state $|\Psi(0)\rangle_{AC} = (|1\rangle_A \otimes |1\rangle_C)$

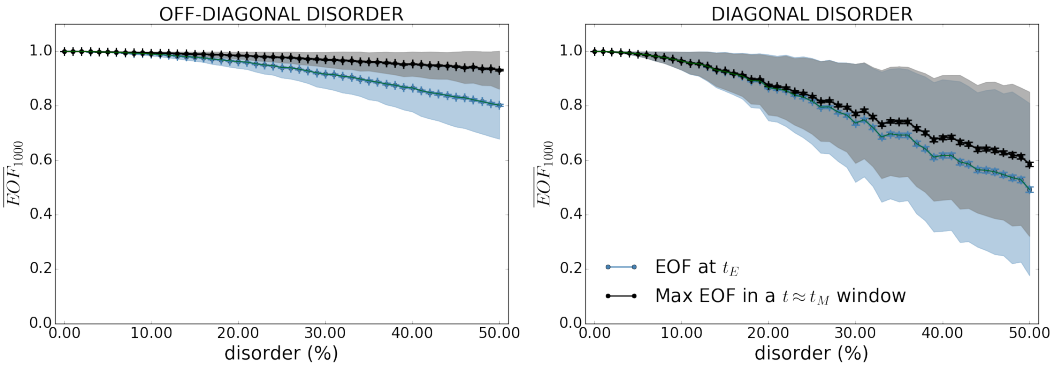

FIGURE 5.8: Averaged EOF at t_E (blue -lower- line) and maximum EOF over a 250 units of time window (black -upper- line) for different levels of off-diagonal and diagonal disorders weighted against the weak coupling (δ) for protocol (ii) and $\delta/\Delta = 0.1$. Black and blue shadows represent the standard deviation, black and blue bars represent the standard error of the mean.

We now focus on the first (ii) of Bell state creation protocols. The results of our robustness test show a remarkable improvement on the resilience of the system against both types of disorder compared with the previous figure. In Fig. 5.8 we again observe very high values of the averaged EOF when off-diagonal disorder is added. For both calculations scenarios, the average EOF values do not peak below 0.8 even with level of disorder of a 50% the weak coupling δ. Similar to the previous case, this protocol also shows more effect when subject to diagonal disorder. However, this is with a clear improvement with respect the previous results as it now decays much more slowly reaching a value of $EOF \approx 0.5$ with 50% of diagonal disorder.

In addition, the two calculated EOF measures $\overline{EOF}$ at t_E and $\overline{EOF}_{max}$ (blue and black lines) have closer values and their standard deviations (blue and black shades) spread less than the ones for the previous protocol for both types of added disorders.

iii) Protocol with initial state $|\Psi(0)\rangle_B = |1\rangle_B$

If we now move to the single-excitation protocol, we observe from Fig. 5.9 that the robustness of the system gets even better. The results for off-diagonal disorder show extremely high averaged EOF values, with both $\overline{EOF}$ at t_E and $\overline{EOF}_{max}$ remaining always around 0.9. The standard deviations of each ensemble are very small indicating that the random error fluctuates within a small range away from the ideal one. For diagonal disorder, we still observe a more pronounced effect but now close to

0.6 at the maximum disorder strength giving the best results of the three protocols under the same conditions.

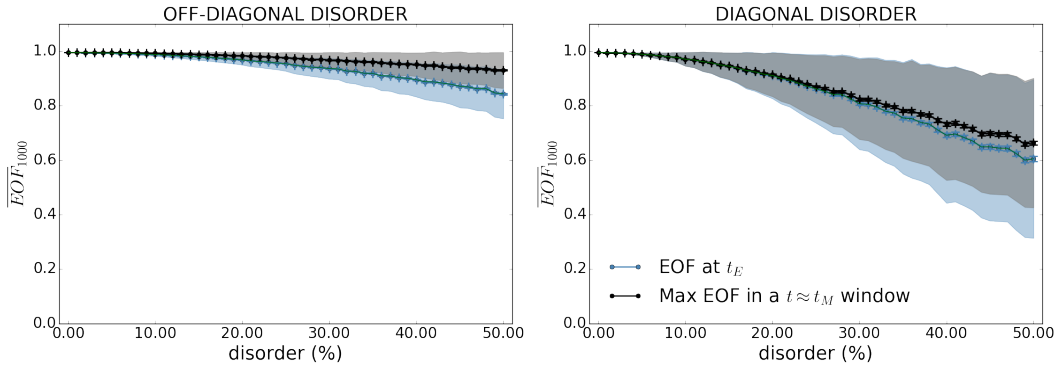

FIGURE 5.9: Averaged EOF at t_E (blue -lower- line) and maximum EOF over a 250 units of time window (black -upper- line) for different levels of off-diagonal and diagonal disorders weighted against the weak coupling (δ) for protocol (iii) and $\delta/\Delta = 0.1$. Black and blue shadows represent the standard deviation, black and blue bars represent the standard error of the mean.

From the analysis of the three versions of our protocol we can find some common trends. For the three injections, the robustness of the system against off-diagonal disorder is remarkably high. The reason for this is that this type of noise only affects the upper and lower band of the energy spectrum in a symmetrical way, leaving the genuinely zero-energy states at zero. Once again, this can be understood from considering our trimer 'toy model' with disorder added to the couplings, such that $\eta + d$ and $\eta + e$ are the off-diagonal terms in the Hamiltonian:

$$H = \begin{pmatrix} 0 & \eta + d & 0 \\ \eta + d & 0 & \eta + e \\ 0 & \eta + e & 0 \end{pmatrix} , \tag{5.21}$$

which yields the eigenvalues

$$\varepsilon = \pm\sqrt{2\eta^2 + 2\eta d + 2\eta e + d^2 + e^2} \ , \ 0 \ . \tag{5.22}$$

As seen in Eq. 5.22, the diagonalisation of such perturbed Hamiltonian leaves the zero-energy state undisturbed.

The same behavior is observed when considering the complete ABC chain system. To illustrate this, the effect of a single realisation of such perturbation in the energy levels is shown in the left panel of Fig. 5.10, and the standard deviation of the average energy values over 1000 noise realisations is presented in the right panel. We show the energy spectrum of our $N = 7$ site system, up to the two-excitation subspace (and ignoring the inert, zero-excitation, 'vacuum' state), and with a level of disorder $E = 5$, corresponding to 500% of the weak coupling δ (we use a huge amount of disorder to make this effect more visible). The spectrum comprises 7

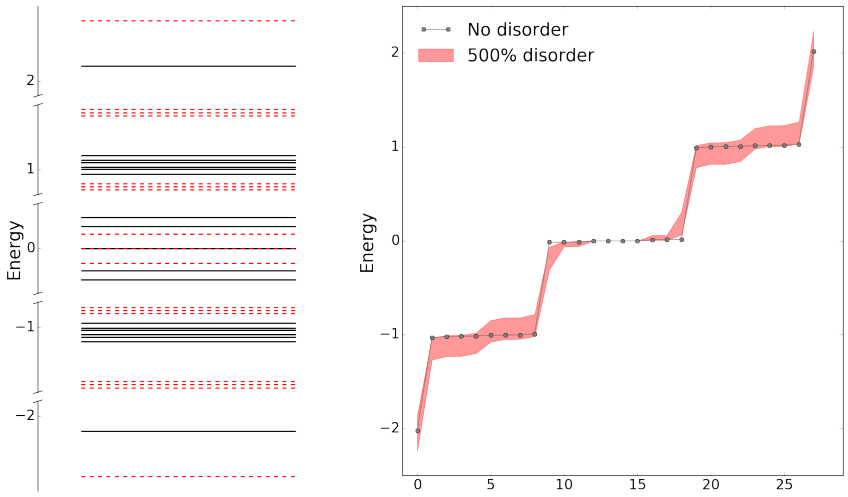

FIGURE 5.10: Effect of the off-diagonal disorder to the energy levels of an ABC chain with $N = 7$, $\delta/\Delta = 0.1$ and up to the two-excitation subspace. In the l.h.s panel we show the symmetric effect of such disorder by presenting the unperturbed energy levels (black solid lines) against the energy levels of a system perturbed by 500% of disorder (red dashed lines). Similarly, in the r.h.s panel the unperturbed spectrum is shown against the standard deviation (red shade) of an ensemble of 100 noise realisations of 500% disorder. From the last we note that the four central 0-energy state remain unperturbed.

single-excitation energy states plus $21 = N!/\big(2!(N-2)!\big)$ two-excitation states. In this case the latter can be expressed approximately as product state combinations of the former.

This enables understanding of the 10 states (close to zero energy) sitting in the gap between two 'bands'. In the single-excitation subspace the spectrum consists of three states belonging to the relevant ABC sites (see Eq. 5.5) with energies $\pm\sqrt{2}\eta, 0$, sitting in the gap, and two states in the upper 'band' and two states in the lower 'band'. In the two-excitation subspace the ABC system can be thought of as generating a trimer of three 'hole' states (a 'hole' being the lack of an excitation in the all excited ABC system and therefore effectively equivalent to the one-excitation states as previously explained), leading to three states in the gap with same energies $\pm\sqrt{2}\eta, 0$. Four additional two-excitation states in the gap can be understood analytically as products of a single-excitation state from the upper band with a single-excitation state from the lower band state. The sublattice (or chiral) symmetry of our system imposes mirror symmetry about zero energy on the spectrum; hence, when taking products of single-excitation upper and lower band states we obtain in the gap two exactly zero-energy states and two states with very small energy, equal to the energy difference between the two single-excitation states in a band, which is of the order of η. We therefore have four exactly zero-energy states in the gap (see the four points in the right panel of Fig. 5.10 with no red shade contribution), along with three states at very small positive energy and three states at very small negative energy, but still clearly within the gap.

As already mentioned, the off-diagonal disorder perturbs the system spectrum symmetrically; consequently the exactly zero-energy states contained at the 0-energy level in Fig. 5.10 are completely protected. At zero energy, the single-excitation and two-excitation (single 'hole') trimer states do not move in energy according to Eq. 5.22, while the two single excitation product band states suffer canceling shifts.

From this analysis we can now also understand why the EOF, even though very robust, does decrease somewhat as the off-diagonal disorder is increased. Despite the four exactly zero-energy states in the middle of the energy gap being protected against this type of noise, the dynamics of the entangling protocol also involves other states in the energy gap (which do suffer small effects due to off-diagonal noise). The states forming the bands also contribute small amplitudes to the protocol dynamics, as the initial states are prepared as site, rather than energy eigenstates.

5.3.2 Time delays

To consider another practical form of error with this model, we also investigate how the asynchronous injection at sites A and C affects the EOF value found at exactly t_E for the Cluster (i) and the Bell (ii) state creation. This type of error does not affect the protocol (iii) as it only needs a single site injection at site B. The effect of this error on the protocol is shown in Fig. 5.11. We observe that even with an injection time delay of 10% t_E, the EOF is still at the high value of 0.91 and 0.95, respectively. We can conclude that our protocol is therefore also robust against asynchronous state injections.

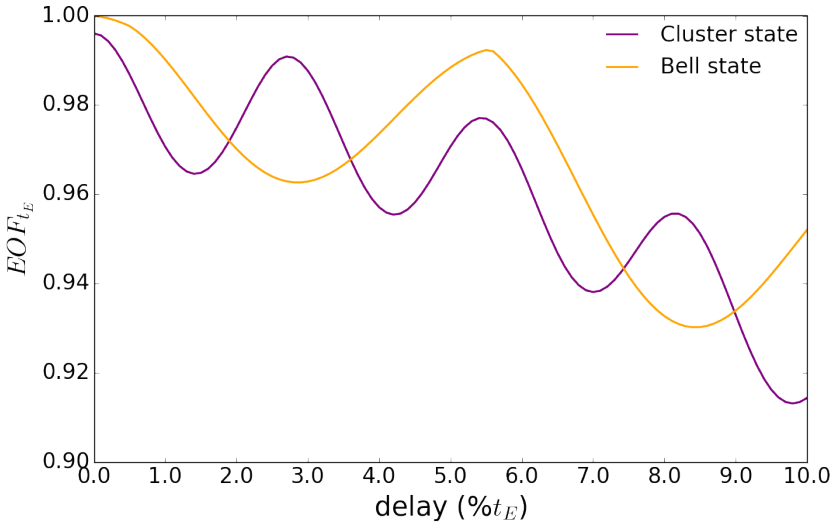

FIGURE 5.11: EOF at t_E against the input delay as a fraction of the mirroring time for protocols (i) –purple profile– and (ii) –yellow profile– with asynchronous injections of $|+\rangle$ and $|1\rangle$ respectively at sites A and C, and $\delta/\Delta = 0.1$.

5.4 Protocol optimization

In the previous sections we have been considering a small ratio, $\delta/\Delta = 0.1$ in order to obtain a well defined profile for the fidelity and EOF dynamics. It can be deduced from Eq. 5.13 that for larger ratios the effective coupling, η, will also be larger. This would effectively increase the overlap between the relevant eigenstates (approximated by Eq. 5.5) peaking at sites ABC and, consequently, the dynamics would be faster. The entangling times along with the robustness of these protocols can then be improved up to a certain level and such optimization will be inspected in this section.

In Fig. 5.12, we present the behavior of our protocols for different coupling ratios. First it is crucial to recalculate the entangling times, t_E, for each ratio in order to know when the EOF peaks to a maximum. This time will still be close to t_M for the Cluster state and $t_M/2$ for the Bell state protocols. However, because t_M is inversely proportional to η, with an increasing value of the coupling ratio, δ/Δ, η will also increase and therefore our entangling protocol will be faster, as observed in the inset of Fig. 5.12.

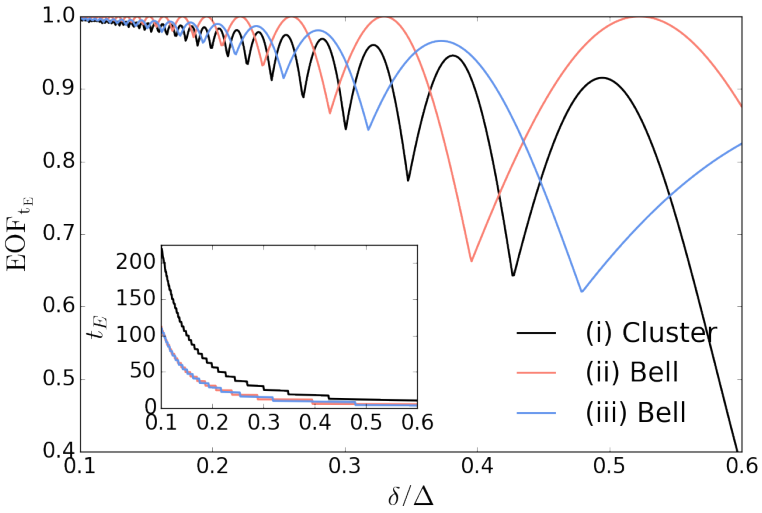

FIGURE 5.12: EOF at t_E for the three different protocols (i, ii and iii) against varying coupling ratio, δ/Δ, for an ABC chain with $N = 7$. In order to calculate such values it is essential to know the rescaled times. The inset shows how the entangling times, t_E, vary with the coupling ratio.

A faster entangling time, t_E, does not necessarily mean that the state retrieved at that time will have an optimal EOF (i.e. close to 1). In Fig. 5.12, we present how the nature of the entangled state involving sites A and C measured at the recalculated times t_E varies with the coupling ratio. We observe a non-linear non-monotonic decay of the EOF with coupling ratio but still obtaining decent values of entanglement for certain coupling ratios corresponding to the maxima of the oscillating profiles. Here it is of particular interest the protocol (ii), where the Bell state is created with

two initial injections, showing a decay that can be observed in the minima of the oscillations but not in their maxima, which remain very close to unity.

We want to find a compromise between the entangling times, t_E, the EOF of the state obtained at those times and the robustness of the protocol. We have already seen that we can shorten our times by increasing the coupling ratio, δ/Δ, and that we can still obtain reasonable amounts of entanglement at those times. We now want to study the behavior of the protocol with increasing coupling ratio against static perturbations and therefore test its robustness against off-diagonal and diagonal disorder. In order to do so we have considered the overall protocols for three different coupling ratios corresponding to different maxima of each profile of Fig. 5.12 as summarized in Table 5.2.

Coupling ratios		
i. Cluster state	**ii. Bell State**	**iii. Bell state**
0.205	0.260	0.204
0.382	0.330	0.280
0.490	0.523	0.373

TABLE 5.2: Chosen coupling ratios δ/Δ corresponding to some of the maxima of Fig. 5.12 profiles for protocols (i), (ii) and (iii).

The different panels of Fig. 5.13 show the averaged EOF obtained at t_E for each of the studied coupling ratios and several levels of diagonal and off-diagonal disorder (up to 50% of the weak coupling) for protocols (i), (ii) and (iii). We see that when using higher coupling ratios our protocols are still considerably resilient against static perturbations compared with the ones with a ratio $\delta/\Delta = 0.1$. Also, particularly in the case when diagonal disorder is present, which was previously shown to be the most damaging type of static deformation for our protocol, the protocol performance is dramatically improved with an increasing coupling ratio: for $\delta/\Delta > 0.37$ in all three cases, the averaged EOF at t_E does not go lower than 0.8 with a diagonal disorder of a 50% of the weak coupling. Additionally, as the coupling ratio gets bigger, each realisation for the EOF calculation deviates less from the averaged value as shown by the narrower standard deviation shades from Fig. 5.13. Such results offer clear evidence that our protocols can be optimized in terms of making the entangling operation times faster without necessarily sacrificing the quality of the entangled state, hence offering an optimal EOF and resilience against disorder.

Let us finish this section commenting on the scalability of the system. The chain length in this model can be increased by adding sets of four sites (two dimers, one either side of site B to preserve the symmetry) and the system will still support the protocol presented here. Yet this chain growth would increase the time taken for

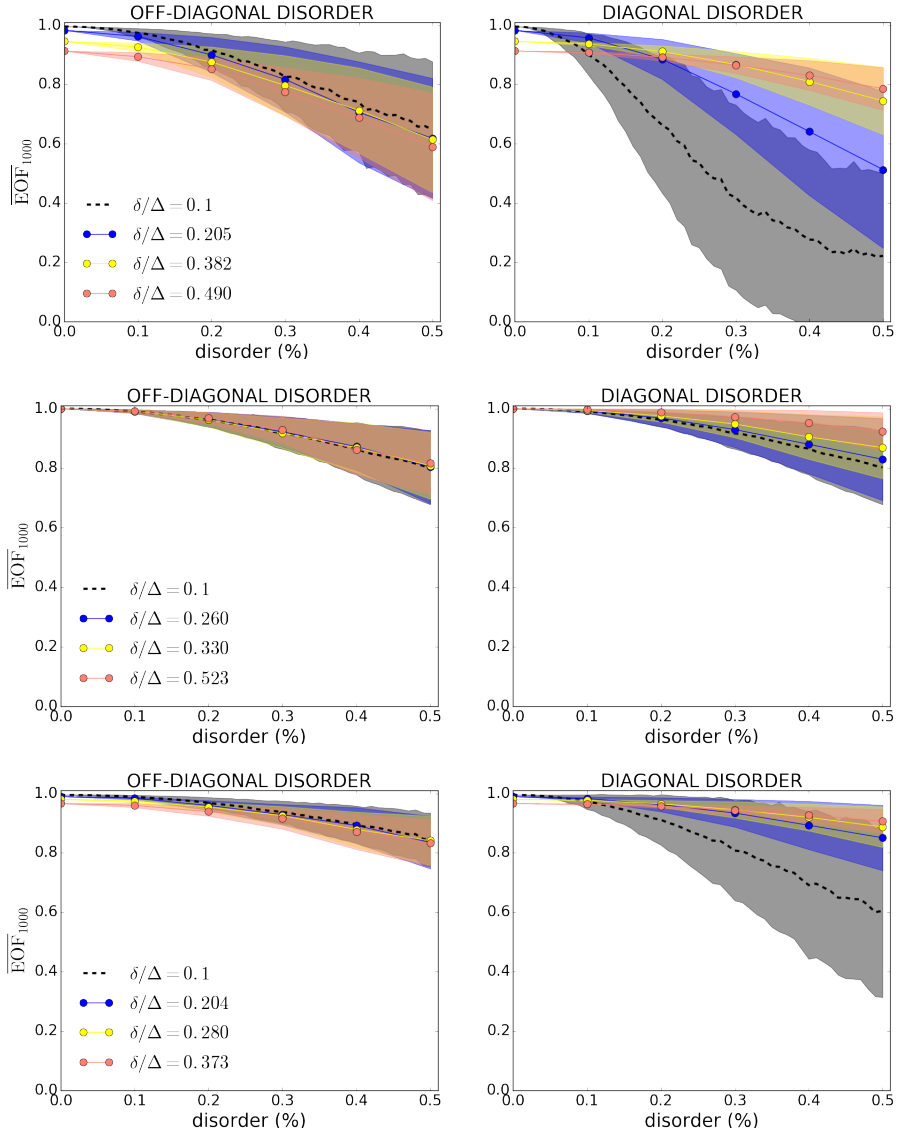

FIGURE 5.13: Averaged EOF at t_E for different levels of off-diagonal (l.h.s) and diagonal (r.h.s) disorders and coupling ratios from Table 5.2 for each of the three protocols (i), (ii) and (iii). The black dashed line shows the averaged EOF for a ratio $\delta/\Delta = 0.1$ and orange, yellow and blue solid lines show the other three compared ratios. The shadows represent the standard deviation of the average for each averaged profile.

entanglement creation, exponentially with chain length, due to the exponential decrease of η with length. The important feature of the application proposed in this work is the robust creation and storage of entanglement and we foresee its usefulness for modular quantum computer schemes. Therefore, the scalability with chain length is less of an issue for this than for applications with the chain acting as a quantum communication bus only.

5.5 Entanglement plus storage protocol

For quantum processing purposes a very useful capability to control is the production of entanglement and its storage until the rest of the system needs to utilize it for further operations. The ABC-type chains indeed offer this flexibility. To this purpose, we propose an extended version of our entangling protocol by considering a slightly different ABC chain, with two dimers at the edges of the chain, so that the three ABC defects are now completely embedded in the dimerised chain (see Fig. 5.14).

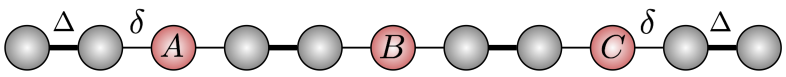

FIGURE 5.14: Extended version of the ABC-type spin chain configuration with two pairs of dimers coupled to site A and C.

The entangling protocol is the same as that demonstrated in Fig. 5.2, as the value of η is not affected. For the sake of brevity, in this section we will only consider the generation and then localisation of the Cluster state, hence the initial injection of two $|+\rangle$ states at sites A and C. We obtain essentially identical behavior in both the dynamics and the resilience against disorder, yet we incorporate an additional step corresponding to a 'switching off' (decoupling) of site B at t_E. This separates the system into two independent but equivalent chains, as seen in Fig. 5.15, when the full entangled state is approximately contained at the X sites of the two subsystems.

The single-excitation spectrum of each of the decoupled chains contains a topologically protected, strongly localised eigenstate at site X. The presence of this state can be explained by considering site X as a defect between two topologically distinct configurations, giving rise to a spatially localised state at zero energy within an energy gap [1], as discussed with detail in Section 4.2. The occupation probability distributions of the five single-excitation eigenstates for the new separated chain are presented in Fig. 5.16. Note that the middle site 3 contains almost the entire occupation probability of the localised eigenstate (highlighted in blue); this state is basically completely localised at site X with negligible contributions at other sites.

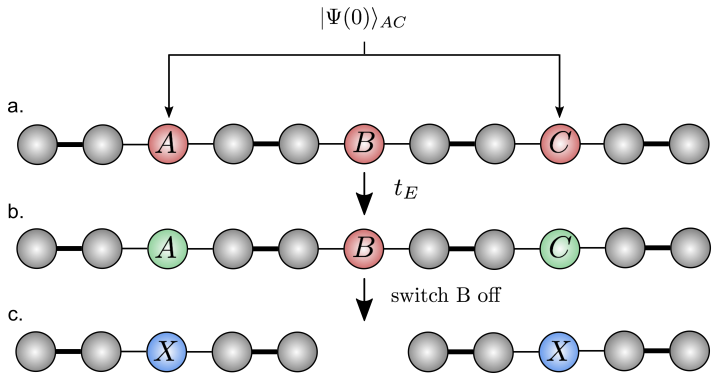

FIGURE 5.15: Entangling-plus-storage protocol. (a) Initial injection (red) at site A and C. (b) Evolution of the system up to time t_E which approximates to t_M as shown previously, and generation of a maximally entangled Cluster state, respectively, between site A and C (green). (c) Decoupling of site B and at t_E and localisation of the entangled state at sites X.

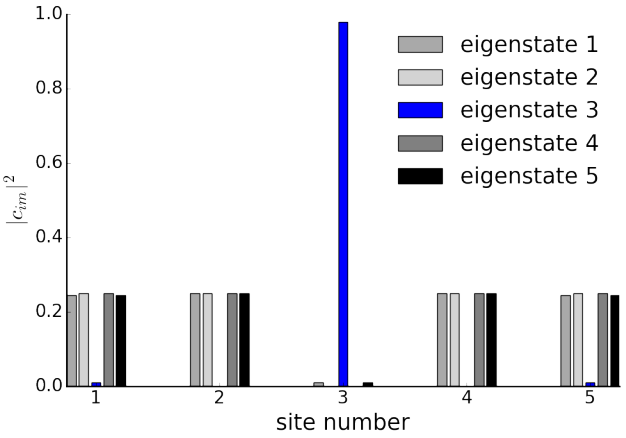

FIGURE 5.16: Occupation probability distributions for the five eigenstates of one of the newly separated chains containing central site X. The eigenstate peaking at site X is highlighted in blue and contains most of its probability at that site.

To model the decoupling we assume that this can be performed on a time scale much shorter than t_E and so employ the sudden approximation to decompose the state of the fully coupled system into the eigenstates of the new decoupled subsystems. From our previous asynchronous injection studies, presented in Fig. 5.11, we can deduce that the errors caused by time delays on the decoupling of site B will have a minor effect to the overall protocol. We also note that efficient experimental methods to perform similar types of decoupling have been proposed, e.g. applied to molecular spin-chain systems [199].

Let us now simulate such decoupling based in the sudden approximation and present it in Fig. 5.17. At $t = t_E^-$, immediately before decoupling site B, the full

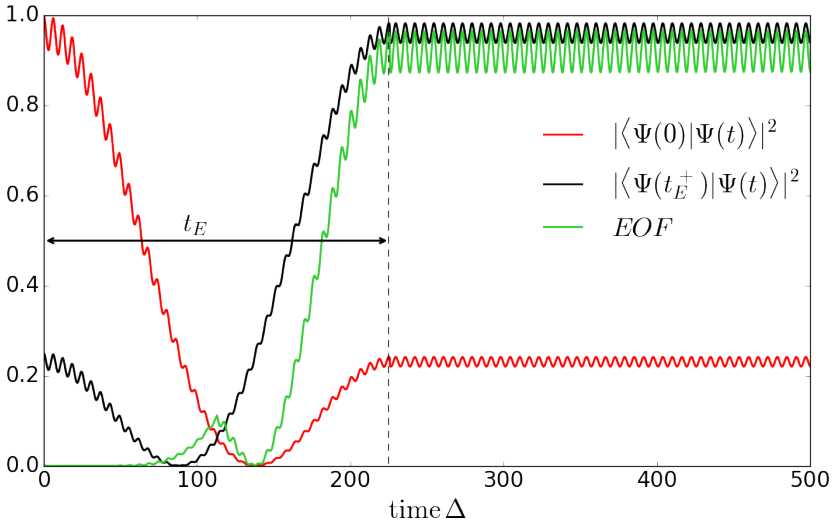

FIGURE 5.17: Fidelity of the initial state $|\Psi(0)\rangle_{AC}$ (i) (red profile) and numerically calculated EOF (green profile) for a $N = 7$ ABC spin chain and $\delta/\Delta = 0.1$. Black profile represents the fidelity of the Cluster state.

coupled dynamics generates two entangled qubits that are indeed localised at the sites A, C, that is the two X sites of the newly decoupled chains at time $t = t_E^+$, immediately after decoupling. It is therefore expected that the entangled state will inherit the topological localisation of the two shorter and equivalent chains after site B is decoupled. The dynamics of such a protocol show that the fidelity of the entangled state at t_E^+, ($F = |\langle\Psi(t_E^+)|\Psi(t)\rangle|^2$), once site B has been decoupled, does not reach values lower than 0.9, hence remains quite localised. For extraction purposes, the entanglement will be most useful if it is localised at just the sites X shown in Fig.5.16. Therefore we calculate the EOF just for those two sites, by tracing out the rest of the chain. We show that the resultant EOF does not drop below 0.9 either, meaning that the probability of finding the two entangled qubits localised at sites X is basically constant and very high with time after site B is decoupled. This type of localisation is also shown to be extremely protected against disorder, as already shown in previous work [1] and in Chapter 4.

5.6 Summary

In this chapter we have presented a robust entangling gate protocol using spin chains, as well as proposing a protocol to localise and store the two resulting entangled qubits. We have demonstrated the potential for ABC spin chains to generate Cluster states and EPR pairs through three different entangling protocols. We have shown numerically and analytically that, after a suitable initial state injection, the natural dynamics of a three-defect, ABC-type chain gives rise to the formation of two maximally entangled qubits. These two entangled qubits can be either extracted at a known time t_E, or localised and stored, so that the extraction and usage

of such a resource can be done at any desired time. The resulting entanglement of formation has been shown to be very robust against two potential fabrication errors of the chain, and also time delay errors on the state injection. It is important to note that the errors considered here are very large and we assume that there exists enough control on the fabrication of real systems such that errors are of just a few percent. Nevertheless, we conclude that diagonal errors are more damaging than off-diagonal disorder (against which there is excellent robustness), so in practical implementations diagonal disorder is the fabrication error to focus on reducing. We also find that timing injection errors at the few % (of t_E) level also have a very small effect on the performance of the protocol.

Importantly, our results prove the possibility of using a large range of characteristic coupling ratios for rapid generation of entangled states to a high fidelity. By increasing the value of δ, the entangled state is generated faster and with only a very small to fidelity loss. For the protocols (i) and (iii) and the highest ratio considered (δ/Δ), we incur a very small reduction in EOF of approximately 0.05; on the other hand, for the protocol (ii), we can retain an EOF of almost unity for all characteristic coupling ratios we considered. This result is particularly encouraging due to the exponential speedup of both entanglement protocols that we observe as the coupling ratio increases. Furthermore, not only is the robustness to off-diagonal disorder almost independent of coupling ratio, but that the robustness to diagonal disorder increases significantly as the coupling ratio is increased. This result exposes an interdependent relationship between the speed and robustness to disorder of the protocols. The ability to maximize both of these factors at little to no reduction in the maximum EOF allows us to propose ABC chains as rapid and reliable entanglement generation devices that present several advantages in front of previous implementations.

All this suggests that our proposals could be promising candidates for the realisation of reliable quantum communication/processing between modules in quantum processors and networks. Our protocols have potential for application in several quantum computer architectures and across of a variety of platforms, particularly where 'off-line' and robust entanglement creation and distribution between two parties is required as a resource.

Chapter 6

Conclusions

Throughout this thesis three main applications of spin chain models have been explored. We have considered in detail the use of such systems to allow for reliable quantum state transfer, to localise quantum states in a protective way and to be used as a quantum entangling gate. Detailed discussion on the outcome of our investigations has already been covered in previous chapters, and we can summarise the main conclusions as follows:

- Short-range quantum communication with high fidelities can be achieved using spin chain models.
- Spin chains are suitable systems in which to investigate localisation phenomena such as Anderson localisation.
- Based on the SSH model, dimerised spin chain systems can be designed to present topologically localised protected states, robust to high levels of static disorder and with potential use for quantum memory applications.
- Localised states in SSH-based spin chains arise from the presence of zero energy modes protected by an energy gap, the size of which can be modulated with the coupling ratio.
- Dimerised spin chain systems with embedded defects serve as a platform from which to build a robust quantum entangling gate able to generate maximally entangled states in three different ways, depending on the initial injection.
- A protocol to store the entangled qubits involving the decoupling of one of the defects is proposed, as well as methods for optimising the operation times and the robustness of the protocol.

6.1 Discussion and practical considerations

The results obtained encourage the possibility of engineering real physical devices to perform a set of quantum operations potentially interesting for computation through the application of our proposed protocols. Nevertheless, as already introduced in Section 1.1.3, there is a set of conditions our quantum devices should satisfy. We

therefore wish to conclude this work with a brief discussion on the fulfillment of the DiVincenzo criteria and other practical considerations of the physical platforms able to embody our proposed spin chain systems.

6.1.1 Qubit characterisation and scalability

As already summarized in Section 1.2.3, any two level quantum system can define the qubit of a spin chain. Various physical platforms are candidates for the realisation of the qubit, from real spins to artificial atoms such as quantum dots or superconducting systems. The possibility of scaling the number of qubits and controlling their interactions is of fundamental importance when designing a quantum computer. For our specific device, the number of qubits for short-range communication purposes will depend on the distance to be covered. On the other hand, for the simplest localisation or quantum gate devices, less demanding lengths of 5 and 7 qubits, respectively, are required. In addition, control of interactions between nearest-neighbour qubits is also essential, as all the protocols here presented are strongly dependent on the chosen coupling scheme. For short-range communication purposes, PST requires the tuning of all the spin-spin interactions, while the protocols based on dimerisation of the chain need the engineering of alternate sites with weak and strong couplings. The experimental realisation of the PST scheme presented here is not an easy task as control over all the couplings is required. In solid-state set-ups PST has only been achieved for moderate chain lengths, e.g. quantum state transfer over three sites using a LNMR platform [200]. Nevertheless, optical waveguides have become an optimal platform where to put into test QST protocols, e.g. the coherent transfer of the initial state over 19 sites using coupled optical waveguides using this coupling configuration has been successfully demonstrated [112] and, more recently, entanglement between a photon propagating through a PST waveguide array and another photon at a different location has been shown to be preserved [201]. Other QST protocols allowing the relaxation of the constraint of engineering of all the couplings have been proposed and realised [202]. Among them we find strategies based on the idea of weakening the end spin couplings to gapped systems [62, 203]. One example is the engineering of dimerised chains, scheme that has been widely used in this work (see Chapter 4 and 5). This dimer configuration might be more amenable to chemical engineering approaches due to its resemblance to some molecular structures. Similar coupling arrangements have also been implemented in a chain of identical coupled dielectric resonators placed in a microwave cavity [111] or optical waveguides in silicon [110], where topologically protected localised states as the ones we encounter in Chapter 4 have been experimentally found.

6.1.2 Initialisation, injection and measurement

The initialisation, injection and extraction of quantum information will depend on the specific hardware used for embedding the mathematical concept of spin chains. A precise and selective control on such methods is crucial for all the protocols here presented. In Chapter 3, an initial state needs to be injected at one site in order to be transfered to another location from which, for communication purposes, it will have to be extracted or measured at some point. Similarly, the main differences between the three entangling protocols here presented are the initial conditions, hence the initially injected states. However, the preparation of pure states in multi qubit systems is not an easy task. Initialisation in ion traps examples involve methods of laser cooling that can bring the ions to the ground state [104] with preparation errors below 10^{-3} [103]. Other methods include the passive relaxation of the qubit to its ground state. At very low temperatures, the qubit is in a thermal state that will approximate to the ground state assuming one waits long enough, the long waiting times being the main issue of these methods. Several ways of initialising superconducting qubits have been proposed, from performing successive projective measurements or cooling with a microwave pulse to coupling the qubit to a tunable harmonic oscillator [204]. When coming to injection, using quantum dots as an example and assuming that a site can be individually addressed, we can consider two injection scenarios [64]. The first consisting of the application of a π-pulse on a specific site of an excitonic QD [205]. The second method applies a SWAP operation that exchanges the quantum states contained in the injection site and an external register [206] the coupling of which can be set *on/off*. It is crucial that this operation is performed fast with respect the relative timescale of decoherence of the particular implementation (e.g. in QD the SWAP operation can be achieved with times of the order of $\sim ps$, well bellow the typical coherence times) [71].

When it comes to the state extraction, we have already seen that one method to store our generated entangled quantum state once the operation has finished implies the decoupling of site B from an ABC spin chain (see Section 5.5). One could quickly couple/decouple the site(s) containing any generated or transfered state to an external register through a SWAP operation similarly to what was described for the initialisation method. These give us the profitable possibility of isolating the state produced for later measurement or to serve as input of a further operation without the need of our device to stop running. For measuring the state, the methods will depend upon the implementation. To mention some examples, in electron quantum dots, these include all-electrical measurements based on current detection or charge sensing [207], or measurement of the polarisation of the photon produced by the decay of an exciton [208]. The state transfered over a chain of coupled waveguides as well as the entanglement fidelity can be measured using polarization state tomography techniques [201].

6.1.3 Universal set of quantum gates

The experimental realisations of qubit already mentioned present methods to perform single and multi-qubit gate operations. In this work we focus on entangling gates, which have already been realised in different platforms. In electron quantum dots, creation of entanglement between the solid-state qubit and a photon has been demonstrated [209]. Schemes for quantum gates between trapped atoms aided with optical qubits have also been proposed [210]. We here propose an alternative strategy for a quantum entangling gate that uses the natural dynamics of the interacting system. Hence, for the correct application of such gate, the platform used will require to be able to coherently transport the injected states as presented in Chapter 5.

6.1.4 Decoherence vs Operation times

Both static and dynamical decoherence can affect the integrity of our protocols and cause unreliable results. In our entangling protocols, excellent entanglement fidelities are obtained even when the presence of static random disorder is of the level of 50 times one of the characteristic energy of the system. This indicates that these systems perform very well against this point of DiVincenzo criteria with regard to static decoherence. The robustness investigations carried over this thesis also give the upper boundd of the allowed fabrication defects when it comes to engineering such devices, which happen to be very high.

With respect to dynamical decoherence, and as already introduced, the operation times of any quantum device must be much shorter than the relevant decoherence times of the qubit. In order to judge our system against it, we qualitatively assess the possibility of performing one of our quantum entangling protocols on few experimental platforms and discuss its viability. We consider some of the typical characteristic coupling energies for electron qubits in GaAs/AlGaAs quantum dots [65], exciton qubits in self-assembled quantum dots [71, 90, 92], trapped ions [101, 211] and superconducting qubits [37, 212]. We use this energies to estimate Δ and then t_E for the particular case of the Bell state creation (ii) protocol (see Section 5.3.1). Table 6.1 shows results for the mid coupling ratio of 0.330 (extracted from Table 5.2) which though providing excellent fidelity and robustness, does not correspond to the best case scenario. From our numerics for the two excitation protocol with a ratio of 0.330 we have t_E = entangling time $= 11.93/\Delta$. We compare our results for the t_E with typical coherence times for the various hardwares. Table 6.1 shows that for most platforms t_E is much smaller than the characteristic coherence times.

Such short times indicate that a number of consecutive entangling operations of the order of ~ 1000 would be possible before starting to lose the coherence of the qubit state for a set of common physical implementations. The possibility of performing multiple operations gives clear optimism on using our protocol in experiments. Our choice regarding the investigation of static decoherence is also validated

Entangling times vs. Decoherence			
Platform	**Characteristic energy, Δ**	**Entangling time, t_E**	**Coherence time**
QDs (electrons)	$0.05\,\mathrm{meV}$	$20\,\mathrm{ns}$	$1\,\mu\mathrm{s}$
QDs (excitons)	$1\,\mathrm{meV}$	$8\,\mathrm{ps}$	$1\,\mathrm{ns}$
Trapped $^{171}Yb^{+}$ ions	$100\,\mathrm{MHz}$	$0.1\,\mu\mathrm{s}$	$10\,\mathrm{min}$
Superconducting qubits	$1\,\mathrm{GHz}$	$0.1\,\mathrm{ns}$	$100\,\mu\mathrm{s}$

TABLE 6.1: Approximated entangling times of our protocol for different experimental realisations and their coherence times.

from these rapid entangling times, as for some cases such types of disorder might be as relevant as the dynamical ones.

Additionally, we can also think of using our schemes to localise and protect a quantum state as a tool to avoid decoherence damaging the computation. These systems could serve as external registers where to temporary allocate the state for its later use via SWAP operations activated by coupling/decoupling to the running circuit. For this purpose, more detailed investigations should be carried out on how other sources of decoherence affects the localisation of the states explored in Chapter 4.

6.1.5 From static to flying qubits

While photon based qubits are ideal platforms for long range communication, solid-state qubits serve as optimal quantum memories and processors. A direct consequence of this is that any spin chain device requires a way to pass the quantum information from the solid-state to the flying qubit. Platforms implementing spin chains are already capable to do this transformation. Examples include the coherent state transfer between an ion trap of cold rubidium atoms to a single photon [213] or the quantum state transfer from a single photon to a single electron spin confined in an InGaAs quantum dot [214]. Also, interfaces coupling superconducting and photonic qubits can be created using microwave cavities or quantum dots [215].

In conclusion, devices based on the spin chain models presented here look promising candidates for QIC technologies as their potential implementations fulfill mostly all the points of DiVincenzo criteria. The precision of the engineering as well as the capabilities of some of the practical realisations presented here evolve very fast. This gives hope that eventually issues related to scalability, control and decoherence will be minor and the future architecture of a functional and robust quantum computer will be defined.

6.2 Future directions

Spin chains have been shown to be versatile theoretical models, with implementations able to fulfill DiVincenzo criteria, and relatively simple to analyse and simulate. This makes them a valuable tool to study the quantum behaviour of different geometries and coupling configurations, which can be applied to a wide variety of physical systems. In this vein, future work may focus on the capabilites and performance of more complex spin networks going beyond one-dimensional schemes. Particularly, we are interested in extending the localisation of the topologically protected eigenstates studied in Chapter 4 to two-dimensional square lattices, geometries which are more resemblant to solid-state crystal lattices. The study of the dynamical behaviour enabling state transfer, generation of quantum states on demand, such as entangled states, or the routing of information through manipulation of the couplings configuration and chain topologies forms also interesting problems worthy of future detailed investigation. Bigger systems as well as higher excitation subspaces, will require a larger computational effort, then the redesign of code to be able to run under an OpenMP and MPI parallel paradigms is a must for this purpose.

To move our results closer to reality, further investigations could include more details on specific implementations and taking into account other relevant experimental parameters. Similarly, the quantum abilities of these and other protocols could be tested against other types of decoherence, both dependent and independent of time. In this direction, the use of mathematical tools such as master equations for the description of the continuous evolution of the open quantum system could be useful a addition to our analysis.

Appendix A

Derivations

A.1 Effective coupling ABC η

When calculating the single excitation spectrum of the 7 sites ABC chain in Chapter 5, seven different energy states are obtained. Two on an upper band E^{+2}, E^{+3}, two on a lower band E^{-2}, E^{-3} and three sitting in between (energy gap), E^{+1}, E^{0} and E^{-1}. From diagonalising the full Hamiltonian in terms of Δ and δ we obtain the following analytical forms of such eigenvalues:

$$E^{\pm 3} = \pm\frac{\sqrt{\Delta^2 + 3\delta^2 + \sqrt{\Delta^4 + 6\Delta^2\delta^2 + \delta^4}}}{\sqrt{2}}$$

$$E^{\pm 2} = \pm\sqrt{\Delta^2 + \delta^2}$$

$$E^{\pm 1} = \pm\frac{\sqrt{\Delta^2 + 3\delta^2 - \sqrt{\Delta^4 + 6\Delta^2\delta^2 + \delta^4}}}{\sqrt{2}}$$

$$E^{0} = 0$$

The three states sitting in the energy band ($E^{\pm 1}, E^0$) can be related to the trimer model of 5.5 to a good approximation, with the site basis states being those with an excitation at A, B and C. The presence of the dimers in between sites A, B and C is responsible for the upper/lower bands. Therefore, the 'effective' coupling between A-B and B-C, η, will be related to the energy difference between the states in the gap. In the trimer model, this difference is equal to $\sqrt{2}\eta$. If we relate this to the energies of the full spectrum, we can approximate η:

$$\Delta E = |E^{+1} - E^0| = |E^0 - E^{-1}| = \sqrt{2}\eta \tag{A.1}$$

$$\begin{aligned} E^{+1} &= \sqrt{2}\eta \rightarrow \frac{\sqrt{\Delta^2 + 3\delta^2 - \sqrt{\Delta^4 + 6\Delta^2\delta^2 + \delta^4}}}{\sqrt{2}} = \sqrt{2}\eta \\ \eta &= \frac{\sqrt{\Delta^2 + 3\delta^2 - \sqrt{\Delta^4 + 6\Delta^2\delta^2 + \delta^4}}}{2}. \end{aligned} \tag{A.2}$$

After rearranging in terms of δ/Δ we obtain the expression presented in Eq. (5.13).

List of Abbreviations

ALU	**A**rithmetic **L**ogic **U**nit
CPU	**C**entral **P**rocessing **U**unit
CU	**C**ontrol **U**unit
EOF	**E**ntanglement **O**f **F**ormation
EPR	**E**instein **P**odolsky **R**osen
GHZ	**G**reenberger-**H**orne-**Z**eilinger state
LNMR	**L**iquid **N**uclear **M**agnetic **R**esonance
NMR	**N**uclear **M**agnetic **R**esonance
PST	**P**erfect **S**tate **T**ransfer
QD	**Q**uantum **D**ot
QIC	**Q**uantum **I**nformation and **C**omputation
QKD	**Q**uantum **K**ey **D**istribution
QST	**Q**uantum **S**tate **T**ransfer
QX	**Q**uantum E**X**eperience
RAM	**R**andom **A**ccess **M**emory
ROM	**R**ead **O**nly **M**emory
SNMR	**S**olid **N**uclear **M**agnetic **R**esonance
SSH	**S**u **S**chrieffer **H**eeger

Bibliography

[1] M. P. Estarellas, I. D'Amico, and T. P. Spiller. "Topologically protected localised states in spin chains". In: *Scientific Reports* 7 (2017), p. 42904.

[2] M. P. Estarellas, I. D'Amico, and T. P. Spiller. "Robust quantum entanglement generation and generation-plus-storage protocols with spin chains". In: *Phys. Rev. A* 95.4 (2017), p. 042335.

[3] R. Ronke et al. "Anderson localisation in spin chains for perfect state transfer". In: *The European Physical Journal D* 70.9 (2016), p. 189.

[4] K. N. Wilkinson et al. "Rapid and robust generation of Einstein-Podolsky-Rosen pairs with Spin Chains". In: *Quantum Information and Computation* 18.4 (2018), pp. 249–266.

[5] A. M. Turing. "On Computable Numbers, with an Application to the Entscheidungsproblem". In: *Proceedings of the London Mathematical Society* s2-42.1 (1937), pp. 230–265.

[6] R. Solovay and V. Strassen. "A Fast Monte-Carlo Test for Primality". In: *SIAM Journal on Computing* 6.1 (1977), pp. 84–85.

[7] G. E. Moore. "Cramming more components onto integrated circuits, Reprinted from Electronics, volume 38, number 8, April 19, 1965, pp.114 ff." In: *IEEE Solid-State Circuits Society Newsletter* 11.3 (2006), pp. 33–35.

[8] G. E. Moore. "Progress in digital integrated electronics [Technical literature, Copyright 1975 IEEE. Reprinted, with permission. Technical Digest. International Electron Devices Meeting, IEEE, 1975, pp. 11-13.]" In: *IEEE Solid-State Circuits Society Newsletter* 11.3 (2006), pp. 36–37.

[9] "Quantum theory, the Church–Turing principle and the universal quantum computer". In: *Proceedings of the Royal Society of London A: Mathematical, Physical and Engineering Sciences* 400.1818 (1985), pp. 97–117.

[10] P. W. Shor. "Polynomial-Time Algorithms for Prime Factorization and Discrete Logarithms on a Quantum Computer". In: *SIAM Journal on Computing* 26.5 (1997), pp. 1484–1509.

[11] L. K. Grover and L. K. "A fast quantum mechanical algorithm for database search". In: *Proceedings of the twenty-eighth annual ACM symposium on Theory of computing - STOC '96*. New York, New York, USA: ACM Press, 1996, pp. 212–219.

[12] M. Fuechsle et al. “A single-atom transistor”. In: *Nature Nanotechnology* 7.4 (2012), pp. 242–246.

[13] N. Gisin et al. “Quantum cryptography”. In: *Reviews of Modern Physics* 74.1 (2002), pp. 145–195.

[14] N. Gisin and R. Thew. “Quantum communication”. In: *Nature Photonics* 1.3 (2007), pp. 165–171.

[15] V. Giovannetti, S. Lloyd, and L. Maccone. “Advances in quantum metrology”. In: *Nature Photonics* 5.4 (2011), pp. 222–229.

[16] M. A. Nielsen and I. Chuang. *Quantum Computation and Quantum Information*. Cambridge University Press, 2000.

[17] A. Einstein, B. Podolsky, and N. Rosen. “Can Quantum-Mechanical Description of Physical Reality Be Considered Complete?” In: *Phys. Rev.* 47 (10 1935), pp. 777–780.

[18] S. J. Freedman and J. F. Clauser. “Experimental Test of Local Hidden-Variable Theories”. In: *Physical Review Letters* 28.14 (1972), pp. 938–941.

[19] B. Hensen et al. “Loophole-free Bell inequality violation using electron spins separated by 1.3 kilometres”. In: *Nature* 526.7575 (2015), pp. 682–686.

[20] J.-A. Larsson. “Loopholes in Bell inequality tests of local realism”. In: *Journal of Physics A: Mathematical and Theoretical* 47.42 (2014), p. 424003.

[21] L. Amico et al. “Dynamics of entanglement in one-dimensional spin systems”. In: *Phys. Rev. A* 69.2 (2004), p. 022304.

[22] W. K. Wootters. “Entanglement of Formation and Concurrence”. In: *Quantum Info. Comput.* 1.1 (Jan. 2001), pp. 27–44.

[23] M. G. Ghahi and S. J. Akhtarshenas. “Entangled graphs: a classification of four-qubit entanglement”. In: *The European Physical Journal D* 70.3 (2016), p. 54.

[24] A. Min WANG. “Generalized GHZ-class and W-class concurrence and entanglement vectors of the multipartite systems consisting of qubits”. In: (2004).

[25] N. Linden and S. Popescu. “Good Dynamics versus Bad Kinematics: Is Entanglement Needed for Quantum Computation?” In: *Physical Review Letters* 87.4 (2001), p. 047901.

[26] C. H. Bennett et al. “Teleporting an unknown quantum state via dual classical and Einstein-Podolsky-Rosen channels”. In: *Physical Review Letters* 70.13 (1993), pp. 1895–1899.

[27] C. H. Bennett and S. J. Wiesner. “Communication via one- and two-particle operators on Einstein-Podolsky-Rosen states”. In: *Physical Review Letters* 69.20 (1992), pp. 2881–2884.

[28] C. H. Bennett and G. Brassard. “Quantum cryptography: Public key distribution and coin tossing”. In: *Theoretical Computer Science* 560 (2014), pp. 7–11.

[29] H. Weimer et al. "Long-Range Quantum Gates using Dipolar Crystals". In: *Phys. Rev. Lett.* 108 (10 2012), p. 100501.

[30] M. H. Freedman et al. "Topological quantum computation". In: *Bulletin of the American Mathematical Society* 40.01 (2002), pp. 31–39.

[31] S. J. Devitt, W. J. Munro, and K. Nemoto. "Quantum error correction for beginners". In: *Reports on Progress in Physics* 76.7 (2013), p. 076001.

[32] N. Nisan and S. Schocken. *The elements of computing systems : building a modern computer from first principles*. MIT Press, 2005, p. 325.

[33] S. Lloyd. "Almost any quantum logic gate is universal". In: *Physical Review Letters* (1995).

[34] R. P. Feynman. "Simulating Physics with Computers". In: *International Journal of Theoretical Physics* 217.6 (1982).

[35] P. Benioff. "The computer as a physical system: A microscopic quantum mechanical Hamiltonian model of computers as represented by Turing machines". In: *Journal of Statistical Physics* 22.5 (1980), pp. 563–591.

[36] G. Kurizki et al. "Quantum technologies with hybrid systems." In: *Proceedings of the National Academy of Sciences of the United States of America* 112.13 (2015), pp. 3866–73.

[37] J. M. Gambetta, J. M. Chow, and M. Steffen. "Building logical qubits in a superconducting quantum computing system". In: *npj Quantum Information* 3.1 (2017), p. 2.

[38] J. Kelly et al. "State preservation by repetitive error detection in a superconducting quantum circuit". In: *Nature* 519.7541 (2015), pp. 66–69.

[39] C. Nayak et al. "Non-Abelian anyons and topological quantum computation". In: *Reviews of Modern Physics* 80.3 (2008), pp. 1083–1159.

[40] A. Y. Kitaev. "Fault-tolerant quantum computation by anyons". In: *Annals. Phys.* 303.1 (2003), pp. 2–30.

[41] R. Blatt and C. F. Roos. "Quantum simulations with trapped ions". In: *Nature Physics* 8.4 (2012), pp. 277–284.

[42] C. Bennett et al. "Experimental quantum cryptography". In: *Journal of Cryptology* 5.1 (1992), pp. 3–28.

[43] D. Bouwmeester et al. "Experimental quantum teleportation". In: *Nature* 390.6660 (Dec. 1997), pp. 575–579.

[44] B. P. Williams, R. J. Sadlier, and T. S. Humble. "Superdense Coding over Optical Fiber Links with Complete Bell-State Measurements". In: *Physical Review Letters* 118.5 (2017), p. 050501.

[45] *ID Quantique, the home of Quantum-Safe Crypto*.

[46] H. J. Kimble. "The quantum internet". In: *Nature 2008 453:7198* (2008).

[47] J. Yin et al. “Satellite-based entanglement distribution over 1200 kilometers.” In: *Science (New York, N.Y.)* 356.6343 (2017), pp. 1140–1144.

[48] A. Montanaro. “Quantum algorithms: an overview”. In: *npj Quantum Information* 2.1 (2016), p. 15023.

[49] S. Debnath et al. “Demonstration of a small programmable quantum computer with atomic qubits”. In: *Nature* 536.7614 (2016), pp. 63–66.

[50] A. Kandala et al. “Hardware-efficient variational quantum eigensolver for small molecules and quantum magnets”. In: *Nature* 549.7671 (2017), pp. 242–246.

[51] P. J. O’Malley et al. “Scalable quantum simulation of molecular energies”. In: *Physical Review X* 6.3 (2016), p. 031007.

[52] J. R. McClean et al. “OpenFermion: The Electronic Structure Package for Quantum Computers”. In: (2017).

[53] *QISKit - Open Source - Quantum Information Software Kit*.

[54] D. P. DiVincenzo. “The Physical Implementation of Quantum Computation”. In: *Fortschritte der Physik* 48.9-11 (2000), pp. 771–783.

[55] E. Pednault et al. “Breaking the 49-Qubit Barrier in the Simulation of Quantum Circuits”. In: *arXiv:1710.05867* (2017).

[56] C. Neill et al. “A blueprint for demonstrating quantum supremacy with superconducting qubits”. In: *Science* 360.6385 (2018), pp. 195–199.

[57] I. Usmani et al. “Mapping multiple photonic qubits into and out of one solid-state atomic ensemble”. In: *Nature Communications* 1.1 (2010), pp. 1–7.

[58] M. Gündoğan et al. “Quantum Storage of a Photonic Polarization Qubit in a Solid”. In: *Physical Review Letters* 108.19 (2012), p. 190504.

[59] A. Delteil et al. “Realization of a Cascaded Quantum System: Heralded Absorption of a Single Photon Qubit by a Single-Electron Charged Quantum Dot”. In: *Phys. Rev. Lett.* 118 (17 2017), p. 177401.

[60] W. Gerlach and O. Stern. “Der experimentelle Nachweis der Richtungsquantelung im Magnetfeld”. In: *Zeitschrift for Physik* 9.1 (1922), pp. 349–352.

[61] S. Bose. “Quantum communication through spin chain dynamics: an introductory overview”. In: *Contemp. Phys.* 48.1 (2007), p. 13.

[62] G. M. Nikolopoulos, I. Jex, et al. *Quantum State Transfer and Network Engineering*. Springer, 2014.

[63] A. Kay. “Perfect, efficient, state transfer and its application as a constructive tool”. In: *Int. J. Quantum Inf.* 8 (2010), p. 641.

[64] R. Ronke, T. P. Spiller, and I. D’Amico. “Effect of perturbations on information transfer in spin chains”. In: *Phys. Rev. A* 83.1 (2011), p. 012325.

[65] G. M. Nikolopoulos, D. Petrosyan, and P. Lambropoulos. "Electron wavepacket propagation in a chain of coupled quantum dots". In: *J. Phys. Condens. Matter* 16.28 (2004), p. 4991.

[66] M. Christandl et al. "Perfect state transfer in quantum spin networks". In: *Phys. Rev. Lett.* 92.18 (2004), p. 187902.

[67] M.-H. Yung and S. Bose. "Perfect state transfer, effective gates, and entanglement generation in engineered bosonic and fermionic networks". In: *Phys. Rev. A* 71.3 (2005), p. 032310.

[68] P. Karbach and J. Stolze. "Spin chains as perfect quantum state mirrors". In: *Phys. Rev. A* 72.3 (2005), p. 030301.

[69] J. Gong and P. Brumer. "Controlled Quantum State Transfer in a Spin Chain". In: *arXiv:quant-ph/0702265* (2007).

[70] D. Burgarth and S. Bose. "Conclusive and arbitrarily perfect quantum-state transfer using parallel spin-chain channels". In: *Phys. Rev. A* 71.5 (2005), p. 052315.

[71] T. P. Spiller, I. D'Amico, and B. W. Lovett. "Entanglement distribution for a practical quantum-dot-based quantum processor architecture". In: *New J. Phys.* 9.1 (2007), p. 20.

[72] G. M. A. Almeida et al. "Disorder-assisted distribution of entanglement in X Y spin chains". In: *Physical Review A* 96.3 (2017), p. 032315.

[73] R. Ronke, I. D'Amico, and T. P. Spiller. "Knitting distributed cluster-state ladders with spin chains". In: *Phys. Rev. A* 84.3 (2011), p. 032308.

[74] B. Ç. Akmak et al. "Robust multipartite entanglement generation via cascaded interactions". In: *arXiv:1803.05243* (2018).

[75] A. Kay. "Generating Quantum States through Spin Chain Dynamics". In: *New Journal of Physics* 19.4 (2016), p. 043019.

[76] J. Chen et al. "Preparing Greenberger-Horne-Zeilinger and W states on a long-range Ising spin model by global controls". In: *Physical Review A* 95.3 (2017), p. 032340.

[77] L. Campos Venuti, C. Degli Esposti Boschi, and M. Roncaglia. "Qubit Teleportation and Transfer across Antiferromagnetic Spin Chains". In: *Physical Review Letters* 99.6 (2007), p. 060401.

[78] I. D'Amico, B. W. Lovett, and T. P. Spiller. "Creating, distributing and freezing entanglement with spin chains". In: *arXiv:quant-ph/0702269v2* (2007).

[79] L. CamposVenuti, C. DegliEspostiBoschi, and M. Roncaglia. "Long-Distance Entanglement in Spin Systems". In: *Physical Review Letters* 96.24 (2006), p. 247206.

[80] L. Campos Venuti et al. "Long-distance entanglement and quantum teleportation in XX spin chains". In: *Phys. Rev. A* 76 (5 2007), p. 052328.

[81] S. M. Giampaolo and F. Illuminati. "Long-distance entanglement and quantum teleportation in coupled-cavity arrays". In: *Phys. Rev. A* 80 (5 2009), p. 050301.

[82] A. Ferreira and J. M.B. L. dos Santos. "Analytic results on long-distance entanglement mediated by gapped spin chains". In: *Physical Review A* 77.3 (2008), p. 034301.

[83] P. Sodano, A. Bayat, and S. Bose. "Kondo cloud mediated long-range entanglement after local quench in a spin chain". In: *Physical Review B* 81.10 (2010), p. 100412.

[84] A. Bayat, S. Pasquale, and S. Bose. "Negativity as the entanglement measure to probe the Kondo regime in the spin-chain Kondo model". In: *Phys. Rev. B* 81.6 (2010), p. 064429.

[85] A. Kay and M. Ericsson. "Geometric effects and computation in spin networks". In: *New J. Phys.* 7.1 (2005), p. 143.

[86] P. J. Pemberton-Ross and A. Kay. "Perfect Quantum Routing in Regular Spin Networks". In: *Physical Review Letters* 106.2 (2011), p. 020503.

[87] M.-H. Yung. "Spin star as a switch for quantum networks". In: *Journal of Physics B: Atomic, Molecular and Optical Physics* 44.13 (2011), p. 135504.

[88] G. Burkard, D. Loss, and D. P. DiVincenzo. "Coupled quantum dots as quantum gates". In: *Physical Review B* 59.3 (1999), pp. 2070–2078.

[89] D. Loss and D. P. DiVincenzo. "Quantum computation with quantum dots". In: *Physical Review A* 57.1 (1998), pp. 120–126.

[90] I. D'Amico. "Quantum dot-based quantum buses for quantum computer hardware architecture". In: *Microelectron. J.* 37.12 (2006), p. 1440.

[91] H Kamada and H Gotoh. "Quantum computation with quantum dot excitons". In: *Semiconductor Science and Technology* 19.4 (2004), S392–S396.

[92] E. Biolatti et al. "Electro-optical properties of semiconductor quantum dots: Application to quantum information processing". In: *Phys. Rev. B* 65 (7 2002), p. 075306.

[93] I. D'Amico. "Quantum buses and quantum computer architecture based on quantum dots". In: *arXiv:cond-mat/0511470v1* (2005).

[94] E. Biolatti et al. "Quantum Information Processing with Semiconductor Macroatoms". In: *Physical Review Letters* 85.26 (2000), pp. 5647–5650.

[95] J. M. Elzerman et al. "Single-shot read-out of an individual electron spin in a quantum dot". In: *Nature* 430.6998 (2004), pp. 431–435.

[96] D. Press et al. "Complete quantum control of a single quantum dot spin using ultrafast optical pulses". In: *Nature* 456.7219 (2008), pp. 218–221.

[97] M. H. Devoret and R. J. Schoelkopf. "Superconducting Circuits for Quantum Information: An Outlook". In: *Science* 339.6124 (2013), pp. 1169–1174.

[98] N. Materise. "An Introduction to Superconducting Qubits and Circuit Quantum Electrodynamics". In: *arXiv:1708.07000v1* (2017).

[99] G Wendin. "Quantum information processing with superconducting circuits: a review". In: *Reports on Progress in Physics* 80.10 (2017), p. 106001.

[100] A. Acín et al. "The European Quantum Technologies Roadmap". In: (2017).

[101] K. R. Brown, J. Kim, and C. Monroe. "Co-designing a scalable quantum computer with trapped atomic ions". In: *npj Quantum Information* 2.1 (2016), p. 16034.

[102] T. D. Ladd et al. "Quantum computers". In: *Nature* 464.7285 (2010), pp. 45–53.

[103] T. Harty et al. "High-Fidelity Preparation, Gates, Memory, and Readout of a Trapped-Ion Quantum Bit". In: *Physical Review Letters* 113.22 (2014), p. 220501.

[104] C Monroe and J Kim. "Scaling the ion trap quantum processor." In: *Science (New York, N.Y.)* 339.6124 (2013), pp. 1164–9.

[105] J. I. Cirac and P. Zoller. "Quantum Computations with Cold Trapped Ions". In: *Physical Review Letters* 74.20 (1995), pp. 4091–4094.

[106] C. Monroe et al. "Demonstration of a Fundamental Quantum Logic Gate". In: *Physical Review Letters* 75.25 (1995), pp. 4714–4717.

[107] J. Jones. "NMR Quantum Computation: A Critical Evaluation". In: *Fortschritte der Physik* 48.9-11 (2000), pp. 909–924.

[108] S. L. Braunstein et al. "Separability of Very Noisy Mixed States and Implications for NMR Quantum Computing". In: *Phys. Rev. Lett.* 83 (5 1999), pp. 1054–1057.

[109] C. Negrevergne et al. "Benchmarking Quantum Control Methods on a 12-Qubit System". In: *Physical Review Letters* 96.17 (2006), p. 170501.

[110] A. Blanco-Redondo et al. "Topological Optical Waveguiding in Silicon and the Transition between Topological and Trivial Defect States". In: *Phys. Rev. Lett.* 116 (2016), p. 163901.

[111] C. Poli et al. "Selective enhancement of topologically induced interface states". In: *Nat. Commun.* 6 (2015).

[112] A. Perez-Leija et al. "Coherent quantum transport in photonic lattices". In: *Physical Review A* 8782 (2013).

[113] S. C. Benjamin et al. "Towards a fullerene-based quantum computer". In: *Journal of Physics: Condensed Matter* 18.21 (2006), S867–S883.

[114] B. E. Kane. "A silicon-based nuclear spin quantum computer". In: *Nature* 393.6681 (1998), pp. 133–137.

[115] M. V. G. Dutt et al. "Quantum register based on individual electronic and nuclear spin qubits in diamond." In: *Science (New York, N.Y.)* 316.5829 (2007), pp. 1312–6.

[116] L. Childress and R. Hanson. "Diamond NV centers for quantum computing and quantum networks". In: *MRS Bulletin* 38.02 (2013), pp. 134–138.

[117] E. Schrödinger. "An Undulatory Theory of the Mechanics of Atoms and Molecules". In: *Physical Review* 28.6 (1926), pp. 1049–1070.

[118] C. Cohen-Tannoudji, B. Diu, and F. Laloë. *Quantum mechanics*. Wiley, 1977, p. 1524.

[119] P. Jordan and E. P. Wigner. "Über das paulische äquivalenzverbot". In: *Z. Phys.* 47 (1928), p. 631.

[120] S. Bose. "Quantum communication through an unmodulated spin chain". In: *Phys. Rev. Lett.* 91.20 (2003), p. 207901.

[121] W. K. Wootters. "Entanglement of formation of an arbitrary state of two qubits". In: *Phys. Rev. Lett.* 80.10 (1998), p. 2245.

[122] *Intel® Core™ i7-4770 Processor (8M Cache, up to 3.90 GHz) Product Specifications*.

[123] M. Christandl et al. "Perfect transfer of arbitrary states in quantum spin networks". In: *Phys. Rev. A* 71.3, Part A (2005), p. 032312.

[124] C. Godsil et al. "Number-Theoretic Nature of Communication in Quantum Spin Systems". In: *Phys. Rev. Lett.* 109 (5 2012), p. 050502.

[125] S. Paganelli et al. "Routing quantum information in spin chains". In: *Physical Review A* 87.6 (2013), p. 062309.

[126] I. D'Amico, B. W. Lovett, and T. P. Spiller. "Creating and preserving multipartite entanglement with spin chains". In: *Physica Status Solidi C*. Vol. 5. 7. 2007, p. 2481.

[127] B. Bellomo, R. Lo Franco, and G. Compagno. "N identical particles and one particle to entangle them all". In: *Phys. Rev. A* 96 (2 2017), p. 022319.

[128] G. M. Nikolopoulos, A Hoskovec, and I Jex. "Analysis and minimization of bending losses in discrete quantum networks". In: *Physical Review A* 85 (2012).

[129] I. D'Amico, B. W. Lovett, and T. P. Spiller. "Freezing distributed entanglement in spin chains". In: *Phys. Rev. A* 76.3 (2007), p. 030302.

[130] S. Lorenzo et al. "Quantum-state transfer via resonant tunneling through local-field-induced barriers". In: *Physical Review A* 87.4 (2013), p. 042313.

[131] T. J. Osborne and N. Linden. "Propagation of quantum information through a spin system". In: *Phys. Rev. A* 69.5 (2004), p. 052315.

[132] T. Ohshima et al. "Robust state transfer and rotation through a spin chain via dark passage". In: *arXiv:0702019* (2007).

[133] V. Kostak, G. M. Nikolopoulos, and I. Jex. "Perfect state transfer in networks of arbitrary topology and coupling configuration". In: *Phys. Rev. A* 75.4 (2007), p. 042319.

[134] A. Wójcik et al. "Unmodulated spin chains as universal quantum wires". In: *Phys. Rev. A* 72 (), p. 034303.

[135] S. Oh et al. "Effect of randomness on quantum data buses of Heisenberg spin chains". In: *Physical Review B* 85.22 (2012), p. 224418.

[136] L. Banchi et al. "Optimal dynamics for quantum-state and entanglement transfer through homogeneous quantum wires". In: *arXiv/1006.1217* (2010).

[137] L. Banchi et al. "Nonperturbative Entangling Gates between Distant Qubits Using Uniform Cold Atom Chains". In: *Phys. Rev. Lett.* 106 (14 2011), p. 140501.

[138] Y. Wang, F. Shuang, and H. Rabitz. "All possible coupling schemes in XY spin chains for perfect state transfer". In: *Phys. Rev. A* 84 (1 2011), p. 012307.

[139] C. Albanese et al. "Mirror inversion of quantum states in linear registers". In: *Phys. Rev. Lett.* 93.23 (2004), p. 230502.

[140] S. Yang, A. Bayat, and S. Bose. "Spin state transfer in laterally coupled quantum dot chains with disorders". In: *Phys. Rev. A* 82.2 (2010), p. 022336.

[141] D. Liu and J.-F. Zhang. "Effect of disturbance in perfect state transfer". In: *Chin. Phys.* 15.2 (2006), p. 0272.

[142] A. Zwick et al. "Robustness of spin-coupling distributions for perfect quantum state transfer". In: *Phys. Rev. A* 84.2 (2011), p. 022311.

[143] G. De Chiara et al. "From perfect to fractal transmission in spin chains". In: *Phys. Rev. A* 72.1 (2005), p. 012323.

[144] D. Petrosyan, G. M. Nikolopoulos, and P. Lambropoulos. "State transfer in static and dynamic spin chains with disorder". In: *Phys. Rev. A* 81.4 (2010), p. 042307.

[145] J. M. Cai, Z. W. Zhou, and G. C. Guo. "Decoherence effects on the quantum spin channels". In: *Phys. Rev. A* 74.2 (2006), p. 022328.

[146] A. Zwick et al. "Optimized dynamical control of state transfer through noisy spin chains". In: *New Journal of Physics* 16.6 (2014), p. 065021.

[147] S. Ashhab. "Quantum state transfer in a disordered one-dimensional lattice". In: *Phys. Rev. A* 92 (6 2015), p. 062305.

[148] N. Bloembergen. "On the interaction of nuclear spins in a crystalline lattice". In: *Physica* 15 (May 1949), pp. 386–426.

[149] A. M. Portis. "Spectral Diffusion in Magnetic Resonance". In: *Phys. Rev.* 104 (3 1956), pp. 584–588.

[150] G. Feher and E. A. Gere. "Electron Spin Resonance Experiments on Donors in Silicon. II. Electron Spin Relaxation Effects". In: *Phys. Rev.* 114 (5 1959), pp. 1245–1256.

[151] P. A. Lee and T. V. Ramakrishnan. "Disordered electronic systems". In: *Rev. Mod. Phys.* 57 (2 1985), pp. 287–337.

[152] P. W. Anderson. "Absence of Diffusion in Certain Random Lattices". In: *Phys. Rev.* 109 (5 1958), pp. 1492–1505.

[153] S. Chakravarty and A. Schmid. "Weak localization: The quasiclassical theory of electrons in a random potential". In: *Physics Reports* 140.4 (1986), pp. 193 –236.

[154] N. Mott. "Electrons in disordered structures". In: *Advances in Physics* 16.61 (1967), pp. 49–144.

[155] D. J. Thouless. "Anderson's theory of localized states". In: *Journal of Physics C: Solid State Physics* 3.7 (1970), p. 1559.

[156] A. M. M. Pruisken. "Universal Singularities in the Integral Quantum Hall Effect". In: *Phys. Rev. Lett.* 61 (11 1988), pp. 1297–1300.

[157] E. N. Economou and C. M. Soukoulis. "Calculation of optical transport and localization quantities". In: *Phys. Rev. B* 40 (11 1989), pp. 7977–7980.

[158] P. Sheng and Z.-Q. Zhang. "Scalar-Wave Localization in a Two-Component Composite". In: *Phys. Rev. Lett.* 57 (15 1986), pp. 1879–1882.

[159] M. Segev, Y. Silberberg, and D. N. Christodoulides. "Anderson localization of light". In: *Nat. Photonics* 7 (2013), p. 197.

[160] A. Crespi et al. "Anderson localization of entangled photons in an integrated quantum walk". In: *Nat. Photonics* 7 (2013), p. 322.

[161] S. S. Kondov et al. "Three-Dimensional Anderson Localization of Ultracold Matter". In: *Science* 334 (2011), p. 66.

[162] F. Jendrzejewski et al. "Three-dimensional localization of ultracold atoms in an optical disordered potential". In: *Nature Phys.* 8 (2012), p. 398.

[163] N. Mott and W. Twose. "The theory of impurity conduction". In: *Advances in Physics* 10.38 (1961), pp. 107–163.

[164] J. Pendry. "Symmetry and transport of waves in one-dimensional disordered systems". In: *Advances in Physics* 43.4 (1994), pp. 461–542.

[165] A Kitaev and C Laumann. "Topological phases and quantum computation". In: *Kitaev Lecture Notes* (2009), pp. 1–31.

[166] J. Preskill. "Fault-tolerant quantum computation". In: *arXiv:9712048* (1997).

[167] K. v. Klitzing, G. Dorda, and M. Pepper. "New Method for High-Accuracy Determination of the Fine-Structure Constant Based on Quantized Hall Resistance". In: *Phys. Rev. Lett.* 45 (6 1980), pp. 494–497.

[168] J. E. Moore. "The birth of topological insulators". In: *Nature 2010 464:7286* (2010).

[169] E. Dennis et al. "Topological quantum memory". In: *Journal of Mathematical Physics* 43.9 (2002), pp. 4452–4505.

[170] W. P. Su, J. R. Schrieffer, and A. J. Heeger. "Solitons in Polyacetylente". In: *Phys. Rev. Lett.* 42.25 (1979), p. 1698.

[171] R. E. Peierls. *Quantum Theory of Solids*. eng. Oxford: Oxford University Press, 2001, p. 238.

[172] A. J. Heeger et al. "Solitons in conducting polymers". In: *Reviews of Modern Physics* 60.3 (1988), pp. 781–850.

[173] A. J. Heeger. "Semiconducting and Metallic Polymers: The Fourth Generation of Polymeric Materials (Nobel Lecture)". In: *Angewandte Chemie International Edition* 40.14 (2001), pp. 2591–2611.

[174] A. G. MacDiarmid. ""Synthetic Metals": A Novel Role for Organic Polymers (Nobel Lecture)". In: *Angewandte Chemie International Edition* 40.14 (2001), pp. 2581–2590.

[175] H. Shirakawa. "The Discovery of Polyacetylene Film: The Dawning of an Era of Conducting Polymers (Nobel Lecture)". In: *Angewandte Chemie International Edition* 40.14 (2001), pp. 2574–2580.

[176] R. Jackiw and C. Rebbi. "Solitons with fermion number 1/2". In: *Phys. Rev.* D13 (1976), pp. 3398–3409.

[177] R. Jackiw and J. R Schrieffer. "Solitons with fermion number 1/2 in condensed matter and relativistic field theories". In: *Nuc. Phys. B* 190 (1981), pp. 253–265.

[178] H. Schomerus. "Topologically protected midgap states in complex photonic lattices". In: *Opt. Lett.* 38.11 (2013), pp. 1912–1914.

[179] E. J. Meier, F. A. An, and B. Gadway. "Observation of the topological soliton state in the Su-Schrieffer-Heeger model". In: *arXiv:1607.02811* (2016).

[180] J. Cho and K. W. Kim. "Quantum Phase Transition and Entanglement in Topological Quantum Wires". In: *Scientific Reports* 7.1 (2017), p. 2745.

[181] L. Li, Z. Xu, and S. Chen. "Topological phases of generalized Su-Schrieffer-Heeger models". In: *Physical Review B* 89.8 (2014), p. 085111.

[182] S. Sen. "Overview of Topological Ideas in Condensed Matter Physics". In: *A Short Course on Topological Insulators*. Springer, 2017, pp. 1–21.

[183] J. W. Alexander. "Topological invariants of knots and links". In: *Transactions of the American Mathematical Society* 30.2 (1928), pp. 275–275.

[184] E. H. Kim et al. "Phase transitions between topologically distinct gapped phases in isotropic spin ladders". In: *Physical Review B* 62.22 (2000), pp. 14965–14974.

[185] S. Ryu and Y. Hatsugai. "Topological Origin of Zero-Energy Edge States in Particle-Hole Symmetric Systems". In: *Physical Review Letters* 89.7 (2002), p. 077002.

[186] J. Zak. "Berry's phase for energy bands in solids". In: *Phys. Rev. Lett.* 62 (23 1989), pp. 2747–2750.

[187] M. Atala et al. "Direct measurement of the Zak phase in topological Bloch bands". In: *Nat Phys* 9.12 (2013), p. 795.

[188] J. K. Asbóth, L. Oroszlány, and A. Pályi. "The Su-Schrieffer-Heeger (SSH) Model". In: *A Short Course on Topological Insulators*. Springer, 2016, pp. 1–22.

[189] P. Delplace, D. Ullmo, and G. Montambaux. "Zak phase and the existence of edge states in graphene". In: *Phys. Rev. B* 84 (2011), p. 195452.

[190] T. Jacqmin et al. "Direct observation of Dirac cones and a flatblanc in a honeycomb lattice for polaritons". In: *Phys. Rev. Lett.* 112 (2014), p. 116402.

[191] S. Pirandola et al. "Advances in quantum teleportation". In: *Nature Photonics* 9.10 (2015), pp. 641–652.

[192] R. Raussendorf and H. J. Briegel. "A One-Way Quantum Computer". In: *Phys. Rev. Lett.* 86 (22 2001), pp. 5188–5191.

[193] V. Srinivasa, J. Levy, and C. S. Hellberg. "Flying spin qubits: A method for encoding and transporting qubits within a dimerized Heisenberg spin-$\frac{1}{2}$ chain". In: *Phys. Rev. B* 76 (9 2007), p. 094411.

[194] S. Bose and V. Korepin. "Quantum Gates Between Flying Qubits via Spin-Independent Scattering". In: *arXiv:1106.2329* (2011).

[195] G. M. A. Almeida et al. "Disorder-assisted distribution of entanglement in XY spin chains". In: *Phys. Rev. A* 96 (3 2017), p. 032315.

[196] M. X. Huo et al. "The Peierls distorted chain as a quantum data bus for quantum state transfer". In: *EPL (Europhysics Letters)* 84.3 (2008), p. 30004.

[197] G. M. A. Almeida et al. "Quantum-state transfer in staggered coupled-cavity arrays". In: *Phys. Rev. A* 93 (3 2016), p. 032310.

[198] G. Gualdi, S. M. Giampaolo, and F. Illuminati. "Modular Entanglement". In: *Phys. Rev. Lett.* 106 (5 2011), p. 050501.

[199] G. A. Timco et al. "Engineering the coupling between molecular spin qubits by coordination chemistry". In: *Nat Nano* 4.3 (Mar. 2009), pp. 173–178.

[200] J. Zhang et al. "Simulation of Heisenberg X Y interactions and realization of a perfect state transfer in spin chains using liquid nuclear magnetic resonance". In: *Physical Review A* 72.1 (2005), p. 012331.

[201] R. J. Chapman et al. "Experimental perfect state transfer of an entangled photonic qubit". In: *Nature Communications* 7 (2016), p. 11339.

[202] C Dlaska, B Vermersch, and P Zoller. "Robust quantum state transfer via topologically protected edge channels in dipolar arrays". In: *Quantum Science and Technology* 2.1 (2017), p. 015001.

[203] Y. Ping et al. "Practicality of Spin Chain Wiring in Diamond Quantum Technologies". In: *Phys. Rev. Lett.* 110 (10 2013), p. 100503.

[204] J. Tuorila et al. "Efficient protocol for qubit initialization with a tunable environment". In: *npj Quantum Information* 3 (2017).

[205] A. Zrenner et al. "Coherent properties of a two-level system based on a quantum-dot photodiode". In: *Nature* 418.6898 (2002), pp. 612–614.

[206] R. Brunner et al. "Two-Qubit Gate of Combined Single-Spin Rotation and Interdot Spin Exchange in a Double Quantum Dot". In: *Physical Review Letters* 107.14 (2011), p. 146801.

[207] R. Hanson et al. "Spins in few-electron quantum dots". In: *Reviews of Modern Physics* 79.4 (2007), pp. 1217–1265.

[208] T. Heindel et al. "Accessing the dark exciton spin in deterministic quantum-dot microlenses". In: *APL Photonics* 2.12 (2017), p. 121303.

[209] W. B. Gao et al. "Coherent manipulation, measurement and entanglement of individual solid-state spins using optical fields". In: *Nature Photonics* 9.6 (2015), pp. 363–373.

[210] L.-M. Duan et al. "Probabilistic quantum gates between remote atoms through interference of optical frequency qubits". In: *Physical Review A* 73.6 (2006), p. 062324.

[211] Y. Wang et al. "Single-qubit quantum memory exceeding ten-minute coherence time". In: *Nature Photonics* 11.10 (2017), pp. 646–650.

[212] A. A. Houck, H. E. Tureci, and J. Koch. "On-chip quantum simulation with superconducting circuits". In: *Nat Phys* 8.4 (2012), pp. 292–299.

[213] D. N. Matsukevich and A Kuzmich. "Quantum state transfer between matter and light." In: *Science (New York, N.Y.)* 306.5696 (2004), pp. 663–6.

[214] Y. He et al. "Quantum State Transfer from a Single Photon to a Distant Quantum-Dot Electron Spin". In: *Physical Review Letters* 119.6 (2017), p. 060501.

[215] Y. Tsuchimoto et al. "Proposal for a quantum interface between photonic and superconducting qubits". In: *Physical Review B* 96 (2017).